AN ABSTRACT OF THE DESSERTATION OF

Khalid A. I. Eleissa Al-Hussan for the degree of Doctor of Philosophy in Nuclear Engineering presented on December 9, 1997. Title: Radiation Dosimetry of Radioimmunotherapy Antibodies Conjugated with ^{90}Y

Abstract approved:

Andrew Klein

The ultimate objective of radiation dosimetry in the treatment of cancer is to predict the biological effects of energy deposited in cells. Radioimmunotherapy (RIT) is rapidly attracting interest as a potential new technique for cancer therapy. ^{90}Y is a potential conjugate isotope for tumor-seeking antibodies (Monoclonal antibodies). In this work, the beta dose kernel of ^{90}Y was calculated using MCNP-4B. The established correlation of beta point kernel could be then used to calculate the conventional dose distribution from the ^{90}Y activity distribution within a tumor mass. In general, the calculated point kernel is in good agreement with the published data. The activity distribution is not uniform and there are regions where there is low or no activity. These regions are known as cold-regions. The effect of the cold-regions on the therapeutic dose was studied for ^{90}Y. Calculations of microdosimetric quantities are important in an attempt to infer the mechanisms of the biological effect of ionizing radiation. In this work, the single event distributions , $f_1(z)$, are evaluated for ^{90}Y for two different radiotherapy cases. The first is for an isolated cancer cell with ^{90}Y bonded to the antigen at the cell surface, in this case no cross-fire effect is

considered from the possible ^{90}Y attached to the surrounding cells (e.g., simulating Leukemia). The second case where the cross-fire effect is considered (e.g., simulating solid-tumors) by assuming a uniform distribution of ^{90}Y within the radiation equilibrium region of the tumor mass. The calculations were performed using the electron transport Monte Carlo code (EMCS) which is specially developed for this purpose. In each of the two cases, the single event spectrum was evaluated for both the whole cell and the cell-nucleus. EMCS simulates the electron tracks in water-vapor down to the lowest vibrational excitation energy (0.198 eV). Extension of the tracking to low energies is another significant aspect of the work. Appropriate electron interaction cross sections were developed to enable these calculations.

Radiation Dosimetry of Radioimmunotherapy Antibodies Conjugated with ^{90}Y

by

Khalid A. I. Eleissa Al-Hussan

A DISSERTATION

submitted to

Oregon State University

in partial fulfillment of
the requirement for the
degree of

Doctor of Philosophy

Presented December 9, 1997
Commencement June 1998

Doctor of Philosophy dissertation of Khalid A. I. Eleissa Al-Hussan presented on December 9, 1997

APPROVED:

Redacted for Privacy

Major Professor, representing Nuclear Engineering

Redacted for Privacy

Head of Department of Nuclear Engineering

Redacted for Privacy

Dean of Graduate School

I understand that my dissertation will become part of the permanent collection of Oregon State University libraries. My signature below authorizes release of my thesis to any reader upon request.

Redacted for Privacy

Khalid A. I. Eleissa Al-Hussan, Author

ACKNOWLEDGEMENTS

I wish to express my sincere appreciation for the encouragement, great patience, invaluable assistance, and friendship offered so willingly by Dr. Andrew Klein, committee chairman. I would like to thank everyone on my graduate committee for their advice, care and support during my graduate study and for their patience during the final stage of this project.

I had the privilege to meet and communicate with several eminent scientists in the area of radiation physics: Dr. Walter R. Nelson, Stanford Linear Accelerator Center (SLAC); Dr. Alex F. Bielajew, National Research Council of Canada (NRC); and Dr. Young-Ki Kim, National Institute for Science and Technology (NIST). I appreciate their advice and valuable comments.

Special thanks to Dr. Todd Palmer for his technical support and valuable scientific comments. I thank all whom I have not mentioned here but certainly not forgotten.

Finally, I am greatly indebted to my family for their support, and encouragement throughout these years.

TABLE OF CONTENTS

Page

1. INTRODUCTION 1

2. BACKGROUND 9

2.1 Biological Effect of Radiation 9

2.2 Radioimmunotherapy 10

2.2.1 Monoclonal Antibodies 10
2.2.2 Radionuclide Selection 12

2.3 Radiation Dosimetry 14

2.3.1 Macrodosimetry 15
2.3.2 Microdosimetry 16

2.4 Electron Track Structure 18

2.4.1 Condensed Walk Monte Carlo 19
2.4.2 Analog Monte Carlo 22

3. CROSS SECTION EVALUATION 24

3.1 Introduction 24

3.2 Electron Elastic Scattering Cross Section 26

3.3 Electron-Impact Ionization Cross Section 33

3.4 Electronic Excitation Cross Section 50

3.5 Dissociative Attachment Cross Section 59

3.6 Vibrational Excitation Cross Section 63

TABLE OF CONTENTS (Continued)

Page

3.7 Cross Section Accuracy 65

3.7.1 Mean Excitation Energy 65
3.7.2 Mass Collision Stopping Power 70

4. ELECTRON TRACK STRUCTURE SIMULATION 74

4.1 Monte Carlo Simulation Method 74

4.2 Direct Sampling Method 75

4.3 Rejection Sampling Method 76

4.4 Algorithm of Electron Analog Monte Carlo Simulation 77

4.4.1 Dissociative Attachment Events 81
4.4.2 Elastic Scattering Events 82
4.4.3 Ionization Collision Events 83
4.4.4 Electronic Excitation Events 87
4.4.5 Vibrational Excitation Events 97

4.5 Energy Spectrum of Beta-Particles 98

5. RESULTS 105

5.1 ^{90}Y Beta Dose Point Kernel 105

5.2 Cold-region Effect 109

5.3 ^{90}Y Microdosimetry 117

5.3.1 General Remarks 117
5.3.2 Sampling Procedures 124

TABLE OF CONTENTS (Continued)

Page

6. CONCLUSION AND DISCUSSION 130

6.1 Summary 130

6.2 Discussion and Recommendations 137

BIBLIOGRAPHY 146

LIST OF FIGURES

Figure		Page
3.1	Total elastic cross section	31
3.2	Differential elastic cross section	32
3.3	Fractional partial ionization cross section	46
3.4	Total ionization cross section	47
3.5	Differential ionization cross section for water vapor for primary electron energies of 50, 100 and 200 eV	48
3.5	Differential ionization cross section for water vapor for primary electron energies of 500, 1000 and 2000 eV	49
3.7	Excitation cross section for triplet-1, triplet-2 and diffusion bands	53
3.8	Excitation cross sections for Rydberg states (A+B); n=3 and n≥4, and (C+D); n=3 and n≥4	54
3.9	Excitation cross sections for dissociative continua 1 and 2	55
3.10	Excitation cross sections for Lyman-α, Balmer-α, Balmer-β, Balmer-γ, and Balmer-δ dissociative excitation states	56
3.11	Excitation cross sections for OH-3064, OH-2800, O-8447, and O-7774 dissociative excitation states	57
3.12	Total excitation cross section	58
3.13	Dissiociative attachment (H-Ion formation) state cross section	61

LIST OF FIGURES (Continued)

Figure		Page
3.14	Dissiociative attachment (O-Ion formation) state cross section	62
3.15	Vibrational excitation cross section for the first group (i.e., v_2)	66
3.16	Vibrational excitation cross section for the second group (i.e., v_{13})	67
3.17	Vibrational excitation cross section for the last group (i.e., v_r.)	68
3.18	Mean excitation energy, $\langle W_{exc}(T) \rangle$ of electrons in water vapor	72
3.19	Collision mass stopping power of water vapor as a function of electron energy	73
4.1	Flowchart for the Analog Monte Carlo Simulation	79
4.2	Probability distribution function $F(T,\theta)$ of the elastic scattering polar angle for different electron energies	85
4.3	Probability distribution function $F_j(T,W)$ of the secondary electron energy for 1b1-Orbital, different curves for different primary electron energies	89
4.4	Probability distribution function $F_j(T,W)$ of the secondary electron energy for 3a1 Orbital, different curves for different primary electron energy	90
4.5	Probability distribution function $F_j(T,W)$ of the secondary electron energy for 1b2-Orbital, different curves for different primary electron energy	91

LIST OF FIGURES (Continued)

Figure — Page

4.6 Probability distribution function $F_j(T,W)$ of the secondary electron energy for 2a1-Orbital, different curves for different primary electron energy 92

4.7 Probability distribution function $F_j(T,W)$ of the secondary electron energy for 1a1-Orbital, different curves for different primary electron energies 93

4.8 Relative beta spectrum of ^{90}Y 102

4.9 Histogram of the beta spectrum of ^{90}Y 103

5.1 Comparison between the beta dose distributions for ^{90}Y 108

5.2 Electron energy-spectra at r = 0.0135 and r = 0.0675 centimeters 110

5.3 Electron energy-spectra at r = 0.135 and r = 0.270 centimeters 111

5.4 Electron energy-spectra at r = 0.405 and r = 0.540 centimeters..... 112

5.5 Electron energy-spectra at r = 0.675 and r = 0.810 centimeters 113

5.6 Electron average, probable, and maximum energy at different radial distances from ^{90}Y point source 114

5.7 Diagram of the simple model used for the calculations of radiation dose profile across tumor cold-region. 115

5.8 Profile of ^{90}Y beta-particle absorbed dose fraction across cold-region of radius R_{CR} (R_{CR}/R_{max} = 0.263, 0.2, 0.175, and 0.15) within tumor, surrounded by uniform distribution of ^{90}Y labeled monoclonal antibodies (hot-region) 116

LIST OF FIGURES (Continued)

Figure		Page
5.9	^{90}Y beta spectrum compared with the collided electron spectrum within tumor mass, which has a uniformly distributed ^{90}Y, calculated using MCNP-4B	125
5.10	Single event distribution due to ^{90}Y for both cell and nucleus from the ^{90}Y beta spectrum	127
5.11	Single event distribution due to ^{90}Y for both cell and nucleus from the collided electron spectrum	128
6.1	^{90}Y beta point dose kernel calculated using MCNP-4B	132
6.2	Relative radial dose profile due to a uniformly distributed ^{90}Y source within a spherical tumor of radius equal to twice the maximum beta particle range	133
6.3	Single event distribution functions for both cell and nucleus from ^{90}Y beta-particles energy spectrum	135
6.4	Single event distribution functions for both cell and nucleus from the collided electron spectrum within the tumor of uniformly distributed ^{90}Y	136
6.5	Inelastic fraction cross section	143
6.6	Fraction cross section as a function of electron kinetic energy in water vapor	144

LIST OF TABLES

Table		Page
3.1	Binding (B) and kinetic (U) energies in (eV) and (N) occupation number of water molecule	39
3.2	Atomic electron radii in Bohr units	42
3.3	Water molecule orbital electron radii in Bohr units	42
3.4	Evaluated a_j and b_j constants for water molecule orbital electron	44
3.5	Analytic cross section parameters for electronic excitation	52
3.6	Analytic cross section parameters for dissociative attachment (Negative Ion) processes	60
3.7	Parameters for vibrational cross sections evaluation	65
3.8	Summary of the formulas used to evaluate cross sections	69
4.1	Energy bins used for beta histogram evaluation	104

Radiation Dosimetry of Radioimmunotherapy Antibodies Conjugated with ^{90}Y

1. INTRODUCTION

The discovery of tumor-associated or tumor-specific antigens has initiated a new strategy in cancer treatment called radioimmunotherapy (RIT). The attractiveness of radioimmunotherapy lies in its specificity to tumor cells: therapeutic agents have a high tendency to locate, approach, and attach preferentially to tumor cells, thereby sparing normal cells. Development of techniques for mass production of monoclonal antibodies (MoAbs) has enhanced the potential of using them for both imaging and therapy. When radioimmunotherapy is performed for localized treatment of tumor cells, weakly penetrating radiation (alpha, beta or Auger particles) is the popular choice. Therefore, the variation of radiation dose among cells should be examined. The approach of microdosimetry is the ultimate technique to assess this variation.

Monoclonal antibodies labeled with radionuclides emitting beta particles may overcome the heterogeneous targeting of tumor cells due to their non-uniform distribution within the tumor mass. This is because of the relatively long range of beta particles compared with alpha particle's range. Therefore, energy can be delivered not only to the bound cell, but also to the neighboring cells.

The strategy and planning of radioimmunotherapy includes finding the distribution of radiolabeled monoclonal antibodies in the body after administration, estimating radiation dose to cellular targets due to a distributed radiation source, and

predicting both tumor-cell killing and normal cell damage based on the knowledge about radiobiological effectiveness.

On the other hand, radioimmunodetection, which is used for diagnostic purposes, follows the same technique but the radionuclides used to label antibodies have a long radiation range so that it can penetrates the patient's body and reach the detection system.

The progress in the field of radioimmunotherapy has been slower than in radioimmunodetection (RID), mainly because radioimmunotherapy has more strict requirements for its practice. Penetrating radiation, such as gamma or X rays, is used in radioimmunodetection; therefore, the amount of activity, and hence the amount of dose, are much lower than that required for radioimmunotherapy. Radioimmunotherapy requires absolute quantification of dose delivered to both tumor and normal cells, while radioimmunodetection requires only differential counts in tumor cells from those in adjacent normal cells. However, because of the present limitation of detection resolution of radioimmunodetection technology, radioimmunotherapy technique requires more reliable approach for dose estimation. Although it is an expensive computational tool, the Monte Carlo approach is considered the most reliable technique for dose estimation at present.

The Dexyribonuleic Acid (DNA) is considered the primary sensitive target for cellular inactivation or killing. However, since the DNA is assumed to be randomly distributed through the cell nucleus, the magnitude of the energy deposition within the cell nucleus appears to be an appropriate choice of the target dimensions with which to relate the toxicity. If some physical parameter of dose to cell nucleus can be related to the probability of cell death, and this parameter can be obtained for all cells within the tissue

of interest, then a method should exist to calculate the fraction of cell survivors within a tumor following treatment by radiolabeled monoclonal antibodies.

Ionizing radiation has direct and indirect effects on the DNA. The direct effect is due to radiation interactions with the DNA molecules. And the indirect effect comes from the DNA chemical reactions with the induced free radicals, generated by radiation reactions with other compounds of the cell. Water-radicals have higher yield and mobility than other free radicals of other cellular compounds. Therefore, water-radicals are considered the main source of the indirect effect. However, the yield of water-radicals decreases significantly during their thermalization and diffusion processes. Once the DNA damage has been chemically stabilized, the cell responds by trying to effect repair by complex enzymatic processes. Therefore, a cellular volume of water constituent containing a nucleus size target is considered a proper model of a biological cell.

When traversing a medium, an electron will face a very large number of interactions which result in small energy losses and deflections, and a relatively small number of 'catastrophic' collisions where it may lose a major fraction of its energy or may be turned through a large angle. This is in great contrast to the behavior of gamma rays or neutrons. Therefore, it is unrealistic, because of the tedious calculations, to simulate all the physical interaction through single-event or analog Monte Carlo simulation of electrons in most practical situations. However, it is feasible to perform the analog simulation in small or microscopic volumes or for low energy electrons. For relatively large or macroscopic volumes, the simulation can be performed using the condensed history Monte Carlo technique. This is based on breaking the electron path into major steps and the energy and direction of an electron at the end of each step are

sampled from a pre-determined multiscatter energy and deflection-angle distributions. There are, however, important constraints with such a method. For instance when geometrical regions or distance to boundaries are very small, or when energy loss or transfer is a smaller or close to the binding energies of electrons or when the transport of low-energy electrons (e.g., $\leq$ 100 keV) has to be simulated. In these situations, either the number of collisions is not enough to consider a process as multiple, or the physics behind the theory itself is violated. Although the condensed history Monte Carlo method makes electron transport simulation feasible in most practical situations, it does not provide the detailed spatial description of the energy deposition events along the electron track which is essential for studying radiation effect on the transport medium. Several computer codes, based on the condensed history method exist and are used in wide applications, particularly, in medical physics applications such as radiotherapy planning. The ETRAN series is one of the earliest codes developed by Berger and Seltzer for electron/photon transport simulation in any medium through plane-parallel slabs [1,2]. The physics of ETRAN is the basis for ITS or the Integrated TIGER Series (TIGER, CYLTRAN, ACCEPT) developed by Halbleib et al. [3,4,5,6,7] for electron/photon transport simulation in any material with more flexible input of data for varying geometry (slabs, cylindrical, or combinatorial). EGS4 is a popular code in radiotherapy which simulates the transport of high energy electrons and photons in any material through user-supplied geometry routines [8,9]. MCNP, which was used in this work, is a general-purpose Monte Carlo N-Particle code [10] that can be used for neutron, gamma, electron, or coupled neutron/photon/electron transport. The code treats an arbitrary three dimensional configuration of material in geometric cells bounded by first and second

degree surfaces and fourth degree elliptic tori. The electron physics in MCNP is essentially that of the Integrated TIGER Series. All of the current condensed history Monte Carlo codes have an electron cut-off energy of 1 keV or higher.

On the other hand, microscopic or analog Monte Carlo simulation of electron transport is identical to the approach used for photon and neutron transport simulations. In principle, the technique is simpler than the condensed history simulation as it does not depend on additional parameters governing the grouping and distance between collisions. However, depending on the electron energy, the physics involved might become considerably more complicated. There are still a number of poorly known cross sections at very low electron kinetic energies and, in certain instances, the simulation of electron transport in liquid water, which is assumed to simulate the biological medium composition, must rely on experimental data extrapolated from gas-phase data or based on theoretical models. This is because of the difficulties of measuring directly the interactions between an electron and water molecules in a condensed phase. There are a number of analog Monte Carlo simulation computer codes, based on electron cross section in water vapor, such as MOCA [11,12,13], DELTA [14], ETRACK [15], TRION [16] and KURBUC [17]. These codes are based on electron cross sections in water vapor normalized to liquid density, but they are different in input data, procedures for tracking the electrons, the value of cut-off energy, which ranges from 10 eV to 1 keV, and the maximum electron energy range from 10 keV to 10 MeV. Also there are codes developed specifically for condensed water, such as OREC [18] and CPA100 [19], and codes developed for both water vapor and condensed phases, such as KAPLAN [20] and ETS [21].

The point kernel approach is a deterministic technique used in radiation dosimetry which relates a point source to the dose to a target which is defined with a combination of parametric values. Dose point-kernels for beta emitting sources have been generated by experimental measurements [22,23] or by solving the electron transport equation analytically [24,25] or by performing Monte Carlo simulation of electron transport [26].

Spencer developed a multiple scattering theory for electrons [24]. Then he produced a numerical solution to the transport equation for monoenergetic electrons assuming an infinite homogeneous medium [25]. In Spencer's treatment, electron interactions with the medium are classified into elastic Coulomb scattering, where the electron changes its direction only, and inelastic Coulomb scattering, where the electron slows down and changes its direction. Bethe's stopping power theory based on the continuous slowing down approximation (CSDA) was used for the calculation of energy losses [27]. Point kernels for beta spectra were calculated by Cross [28], Berger [29], and Cross et al. [30], based on Spencer's monoenergetic point kernels. Later, Berger used the ETRAN Monte Carlo computer code [1,2], which is based on his condensed history Monte Carlo method [31], to generate monoenergetic point kernels in liquid water [26]. EGS4, an independently developed Monte Carlo code [32,33], was used by Simpkin and Mackie [34] to generate point-source dose kernels for monoenergetic electrons and for eight beta-particles emitters. The radial dose distribution around an isotropic point source of monoenergetic electrons in water has been calculated by Cross et al. [35] using the ACCEPT Monte Carlo code [3,4,5,6,7]. Their results were averaged over beta spectra to derive distributions for 147 beta emitters. Bardiès and Chatal [36] calculated absorbed dose fractions and mean values per unit accumulated activity in source spheres 10 μm to

2 cm for 22 beta-emitting radionuclides. Their calculations were performed using point kernels based on the recent point kernels of Berger calculated by ETRAN.

The Medical Internal Radiation Dose (MIRD) Committee of the Society of Nuclear Medicine has published guidelines for calculating the absorbed dose from internally distributed radionuclides [37,38]. Their technique is widely accepted through the world. The scheme developed by the MIRD committee allows one to calculate the average dose within a target volume easily utilizing tabulated dose fraction factors.

Refining dose estimates for radioimmunotherapy becomes essential because of the lack of conventional techniques of internal dose estimation which assume a uniform distribution of activity in the source region. Several studies have been performed to treat the non-uniformity of the activity distribution [39,40,41,42,43,44]. Distribution of absorbed dose is obtained by differential contribution of dose from each point source of beta particles within the tumor mass. The calculations are based on a beta dose kernel which represents the radial distribution of absorbed dose about an individual point beta source. Beta dose kernels were tabulated in the literature [25,34,35,39]. These beta dose kernels were originally calculated for monoenergetic electrons and then averaged over the beta spectrum.

The first objective of this dissertation is to calculate a beta dose kernel by sampling electron energy directly from the ^{90}Y beta spectrum eliminating the approximation of the beta averaging followed in the published beta dose kernel data. Moreover, an analytical formula for ^{90}Y beta dose kernel was obtained which then can be used to calculate the differential contribution of dose from each beta point source within the non-uniform ^{90}Y-activity tumor mass. The second objective is to study the effect of

cold-region (region within the tumor mass which has zero ^{90}Y-activity) on the dose profile across the cold-region . The investigation was performed for different spherical cold-region sizes (relative to the maximum range of ^{90}Y beta particles). Then, the minimum dose for smaller cold-region sizes can be estimated by extrapolation. Yet, most of the present dosimetry studies provide absorbed dose profile throughout the tumor. Thus, estimates of dose addressed specifically to individual cell nuclei is necessary. This is because it is widely held that cell killing is indeed a result of radiation damage to nuclear DNA. It is this probability distribution of doses to individual cell nuclei which is a more accurate indicator of the level of cell killing for treatment. Therefore, the third objective of this dissertation is to evaluate the basic microdosimetric quantity: the single event distribution for ^{90}Y-beta particles which consequently can be used to estimate ^{90}Y-beta hit probability.

This dissertation contains the following: general principles of biological effect of ionizing radiation, radioimmunotherapy, ionizing radiation macro-and-micro dosimetry, electron track structure (Chapter 2); compilation of theoretical and experimental electron interaction cross-section data for different types of collisions and representing each cross-section type by a proper analytical formula customized for water and suitable for track structure simulation (Chapter 3); description of the electron track structure simulation using analog Monte Carlo technique (Chapter 4); calculation of ^{90}Y-beta dose kernel and derivation of a formula which correlates the radial distance and the absorbed dose; estimation of cold-region effect; and calculation of ^{90}Y-beta single event density. This study is concluded by discussing the results obtained and suggesting the future work for completing the strategy of radioimmunotherapy.

2. BACKGROUND

2.1 Biological Effect of Radiation

Interactions of ionizing radiation with biological material induce a variety of initial processes which may or may not lead to a particular biological damage. These involved processes form a long chain which can have physical, chemical, biochemical and cellular as well as temporal aspects. The time domain of radiation response is divided into five stages; physical, physiochemical, chemical, biochemical and cellular stages. The time domain division makes it convenient for classification and identification of the particular mechanisms involved in each one of the five stages.

The first stage is the physical stage occurring in approximately 10^{-15} sec. In this stage, ionization and electronic excitation of constituent molecules occur and are followed by vibrational and rotational excitations. The second stage in the sequence is the physiochemical stage occurring over about 10^{-13} sec, which initiates ion recombination and ion-neutral atomic and molecular reactions within a limited spatial region along the path of the penetrating radiation. In this stage, the incident radiation and its induced secondary electrons lose most of their kinetic energies and the electrons become thermalized. The next stage is the chemical stage occurring at about 10^{-11} sec. In the chemical stage, a series of chemical reactions start to spread, involving molecules of different species which may cause significant structural changes in the molecular constituent of the biological system. Bimolecular alterations occur in the cellular stage, with a time scale from fractions of seconds to years encompassing the sequential response

of the organism. Molecular alteration to biomolecules could result in cell structure alterations which can lead to metabolic changes in the cell. These changes could result in different kinds of endpoints including mutation, transformation and cellular death. The route and mechanisms leading to early biological effects, i.e., cellular effects, and late biological effects, i.e., tissue effects, are very complicated but to a significant extent they are mediated via chromosomal aberrations.

2.2 Radioimmunotherapy

Historically, cancer therapy has consisted primarily of surgery, chemotherapy, and external irradiation. Because of the risk of surgery, and the adverse effects of chemotherapy and external radiation, there is a tremendous opportunity for new non-invasive therapies that offer reduced associated side-effects and improve efficacy.

2.2.1 Monoclonal Antibodies

Recent advances in genetic engineering have introduced an approach to kill cancer cells with "magic bullets" or cytotoxic agents. One kind of these cytotoxic agents is monoclonal antibodies labeled with radioisotopes. Cancer cells are targeted by the labeled monoclonal antibodies, which preferentially bind to cancer cells. Site-directed radiolabeled monoclonal antibodies are aimed primarily at antigens on the cell surface or at receptors expressed in high numbers on cancer cells.

Usually, radioimmunotherapy (RIT) is preceded by radioimmunodetection (RID) in a complicated protocol involving serial imaging and pharmacokinetic analysis after

multiple, escalating doses of radiolabeled monoclonal antibodies [45,46]. Small, tracer amounts of radiolabeled monoclonal antibody are adminstered in order to determine the optimal dose of monoclonal antibody to achieve maximal binding to tumor cells with minimal binding to non-targeted or normal cells.

Hematopoietic cancers are successful targets for radioimmuonotherapy (RIT) by radiolabeled monoclonal antibodies (mAb's). This is because of their radiosensitivity and accessibility to mAb.

On the other hand, radioimmunotherapy of solid tumors is complicated by relative radioresistance of many types of cancers as well as the more difficult pharmacology as compared with hematopoietic cancers. Therefore, it is more difficult to saturate solid tumor cells with targeted radiation. In general, the use of radioimmunotherapy in solid tumors has seen far fewer successes than similar approaches in hematopoietic cancers. This is largely because of the heterogeneity of the intra-tumor distribution of injected monoclonal antibodies. There are a number of causes for this heterogeneity, such as the heterogeneous distribution of tumor cells within tumor mass [47,48]. Single cells or small groups of cells may be separated by relatively large volumes of host-reaction or tumor secretion with the tumor cells constituting only a few percent of the tumor mass. Furthermore, tumor cells can have an irregular expression of the antigen to which the monoclonal antibody is directed [49,50]. Areas with poor monoclonal antibody localization are refereed to as cold regions.

Accordingly, radioimmunotherapy of solid tumors needs extensive investigation before its practical implementation. Nevertheless, based on the current knowledge status, radioimmunotherapy in the near future, will probably be most useful for eliminating

residual or occult sites of malignancy after surgery reduces the tumor burden, prolonging life, and improving the quality of life for patients with advanced disease.

The potential success of any radioimmunotherapy protocol is based on the following parameters :

1. The specificity and affinity of monoclonal antibodies should be high for tumor cells and zero or low for normal cells.
2. The time factor: The tumor uptake of monoclonal antibodies should be rapid and the biological half-life in tumor cells relative to normal cells should be long. Also, the clearance speed from the normal tissues should be high, in particular from areas affecting dose limiting organs such as bone marrow [51,52].
3. Choice of radionuclide

2.2.2 Radionuclide Selection

Wessels and Rogus [53], O'Brien Jr [54], Jungermann et al. [55] and Leonard and Srivastava [56] have listed suitable radionuclides for labeling monoclonal antibodies. Selection of suitable radionuclides is based on several characteristics :

1. Physical half-life ($t_{1/2}$)
2. Emission type
3. Daughter type
4. Dose rate
5. Metabolism and excretion

6. Stability of linkage to antibody molecule (Ig)
7. Damage to antibody molecule (Ig)
8. Radionuclide production

The time required for the radiolabeled antibody to find its tumor antigen and to deliver its dose in the tumor is estimated to be of the order of 1-3 days [57]. Therefore, the radionuclide which is conjugated to the antibody should have a half-life of this order. Radionuclides with longer half lives would lead to increase non-target patient dose if the antibodies are shed before the radioactive decay.

Alpha-emitting radionuclides sometimes are favored because of their high radiotoxicity. It is estimated that only 200-300 decays at the cell surface are enough to reduce the cells survival to 1% level [58]. While for β-emitters between 500 to 10^6 decays are necessary to produce the same effect. Nevertheless, β-particles have longer ranges which could be used to compensate for the lack of homogeneity of monoclonal antibody distribution. That is, regions of poor antibody concentration (cold regions) could receive better radiation sterilization due to the contribution of surrounding regions which have a better antibody concentration. This cross fire effect depends on the kinetic energy distribution of the beta particles and the end point energy of the beta decaying radioisotope.

Some radionuclides emit charged particles (α or β particles) accompanied by X or γ-rays. The ranges of these X or γ-rays are much longer than the charged particles ranges. Thus, they will provide unnecessary dose to healthy tissue. Therefore, these radionuclides should be avoided unless they are needed for diagnostic imaging purposes.

The daughter nucleus of the selected radionuclide should be stable to avoid any additional dose to other tissues in the patient. Moreover, it has to be chemically compatible with the antibody and does not form any risk of toxicity. In case of α-emitting radionuclides, the α-recoil could have sufficient kinetic energy to rupture the radionuclide antibody ligand leaving the daughter product to diffuse away from the tumor.

Because of the desired short half-life (few days) of the radioisotope, it would be more practical to produce it locally with a sufficient specific activity. Particular isotopes can be readily produced by a medium-energy cyclotron or similar accelerator or following a high purity striping chemical approach from longer half life parents.

A systematic plan for radioimmuonotherapy is essential for predicting the therapeutic effects under varying conditions. The plan includes finding the radiolabeled monoclonal antibodies distribution in the body after administration. Estimation of radiation dose to cellular targets due to distributed radiation source is considered an essential element in this plan. The last part of the plan covers the biological effect (i.e., sterilization) prediction based on the estimated radiation dose for both tumor and normal cells.

2.3 Radiation Dosimetry

Studies of radiation interaction with matter can be performed following two different approaches. The first approach (Approach-I) concerns the fate of radiation after interaction with matter. Typical examples of studies following this approach are radiation

transport problems occurring for example in shielding calculations. Radiation transport calculations can be performed following deterministic techniques, such as point kernels, or statistical Monte Carlo method. The second approach (Approach-II) concerns the fate of matter after interaction of radiation with material. It is more complicated and provides more analytical details of radiation interactions. It involves several scientific disciplines. Typical examples of studies following the second approach are found in radiation chemistry and biology. Solutions of problems in these fields are obtained from the detailed analysis of radiation track structure. Reasons for the difficulties of this approach are manifold. First, any piece of irradiated matter is a new material that needs to be fully characterized. Second, irradiated matter is, in general, in a non-equilibrium state that changes physically and chemically with the time. Finally, existing tools and techniques, both experimental and theoretical, for material characterization are limited.

2.3.1 Macrodosimetry

In macrodosimetry (or conventional dosimetry), the average energy deposited at a target site per unit mass is referred to as the absorbed dose, D. It is a deterministic quantity and its amount is equal to the total energy deposited by the incident radiation per gram of absorber. From a regulatory point of view in radiation protection of the public and radiation workers this average quantity of dose is a sufficient measure in determining the safety level of the environment. The amount of the average absorbed dose is determined either by direct measurements or by calculation following the first approach (Approach-I) when direct measurements are not possible.

2.3.2 Microdosimetry

In some of the radiation applications such as those in medical field (e.g., radioimmunotherapy), the cellular dose is the target information in dosimetry. The average dose quantity, D, may not be valid when applied to cellular dose estimation [59]. This is mainly because of the heterogeneous radiolabeled antibody distribution which results in a variation of dose among targeted cells. This variation in dose becomes more obvious if these radiation sources are composed of weakly penetrating particles such as beta or alpha particles. Furthermore, the energy deposition within small targets is a stochastic process and its randomness has been recognized [60].

The microdosimetry concept is used to describe the process involved in determining the statistical distribution of energy deposition in very small volumes such as cells or cell nuclei. Initially, the microdosimetric approach was applied only for external radiation sources. Rossi initially developed the conceptual and mathematical framework of microdosimetry [60]. On his work, he established the specific energy quantity, z, which quantifies every radiation interaction event, and the single event density $f_1(z)$. Roesch extended Rossi's theories to describe the microdosimetry of internal alpha emitters [61]. He determined single event spectra using both theoretical calculations using the Monte Carlo technique and proportional counter measurements.

For high dose radiation fields of concern for external radiation therapy multiple event spectra become interesting. This can be obtained by convoluting the stochastic single event density of individual target hits with the hit probability distribution. The microdosimetric quantity, specific energy, z, used to denote the stochastic energy

deposition per unit mass from multiple track transferals, is the microdosimetric analog to absorbed dose D. The frequency mean $\bar{z}$ of a multiple event specific energy spectrum $f(z)$ is under most circumstances equal to the absorbed dose, D. Identical specific energy means ($\bar{z}$'s) resulting from differing specific energy spectra do not imply equal toxicity. This notion is of immense importance for radioimmuonotherapy because microdosimetry can predict widely differing tissue toxicities resulting from identical average tissue dose deliveries.

The first microdosimetry study relating to radioimmunotherapy was performed by Fischer for monoclonal antibodies labeled with alpha emitters [62]. He covered a broad class of irradiation geometries and his work showed a strong need for microdosimetry in cellular-dose estimation.

Kellerer and Rossi proposed the 'theory of dual radiation action' (TDRA) to investigate the link between radiation physics and cellular radiology [63]. The TRDA provides a precise link between the microdosimetric quantities and the biological effect of radiation. They have surpassed their theory in its original form, i.e., a site model, by the distance model which has been formalized as the so-called ' theory of generalized dual radiation action' [64]. In the site model, each radiation sub-lesion was assumed to have a constant probability of leading to a given biological effect within the sensitive site. That is, the shape of the dose-effect relationship for a given biological effect is not modified by any subsequent biological processes such as dose-dependent repair process. In contrast, in the distance model the probability of sublesions interacting depends on the distance apart rather than being constant within the site volume. Probability functions proposed to fit mammalian cell data have very large values at distances of nanometer

scale and decreasing to a very low probability values at distances of micrometers scale [63, 65-68]

DNA is the relevant target for cell sterilization [69-71]. It is assumed to be randomly distributed throughout the cell nucleus. Therefore, the magnitude of energy deposition within cell nucleus appears to be an appropriate choice for target dimensions with which to relate cell toxicity. The cell dimensions encounter in practice vary between 6 and 20 micrometers in diameter with the corresponding diameter of the cell nucleus ranging from 4 and 12 micrometers.

2.4 Electron Track Structure

Track structures of beta particles (i.e., electrons) are composed of the spatial distribution of the energy loss events (ionizations and excitations) along the particle track. It forms the basic quantity in characterizing the physical aspects of radiation effects. At present, there is no satisfactory method for obtaining images of the track structure experimentally. The existing experimental techniques, such as nuclear emulsion, do not have sufficient resolution to represent individual ionizations. Thus, the only practical way to obtain geometric representations of charged particle tracks is by Monte Carlo simulation. The accuracy of a Monte Carlo simulation depends on the accuracy of the material constants such as the interaction cross section data. It also depends on the randomness of the random numbers generated and the total number of random numbers used.

Monte Carlo simulation provides a full description of particle tracks, i.e., consists of the full interaction-by-interaction histories of a large number of beta particles interacting with the biological medium. Then, a statistical relationship is established from these histories to derive microdosimetric quantities such as single event and multiple events distributions and the corresponding mean values. Basic information on the electron interaction cross sections, spectrum of beta-particle initial energies and an electron transport model are needed to simulate the tracks of beta particles.

The transport of electrons is dominated by the long range of the Coulomb force. This results in large number of interactions. Therefore, in contrast to photons or neutrons, it is very time-consuming to simulate electron motion on an interaction-by-interaction basis for many situations of practical interest. For example, Berger and Wang [72] showed that on the order of 10^4 collisions are required to slow down an electron from 0.5 MeV to 1 keV in aluminum. In comparison about 30 collisions, under the same conditions, are enough to slow a neutron down from 0.5 MeV to 0.0625 MeV, and about 10 photon collisions are sufficient to have the same energy loss.

2.4.1 Condensed Walk Monte Carlo

Even with the aid of the current generation of powerful computers, it is not possible to simulate all of the physical electron interactions on an event-by-event basis. This aspect has motivated the development of the so called 'condensed history' electron transport [31]. The condensed history method is useful to evaluate the fate of electrons while disregarding the fate of the transport medium, i.e., following Approach-I (sec. 2.3).

Condensed history Monte Carlo is based on breaking an electron's path into many steps. These steps are chosen to be large enough to encompass many collisions but short enough that the mean energy loss in any one step is small compared to the electron's energy. Then, the energy loss and the angular deflection of the electron during each step can be sampled from probability distributions based on appropriate multiple scattering theories. Multiple-scattering theories attempt to use the fundamental cross sections and the statistical nature of the transport process to predict probability distributions for energy loss and angular deflection.

The MCNP-4B code (A general Monte Carlo N-Particle transport code, version-4B) [10] was used to perform part of the calculations required in this work. This code follows the condensed walk algorithm for electron transport simulation. It utilizes the Goudsmit-Sanderson theory [73] for angular deflections, the Landau theory [74] of energy-loss fluctuations, and the Blunck-Leisegang enhancement [75] of Landau theory.

In MCNP, The electron's path is divided into major steps called energy steps and smaller substeps. The major steps have a constant logarithmic spacing, i.e.

$$\frac{E_n}{E_{n-1}} = k \tag{2-1}$$

Where $k = 2^{-1/m}$, and $m = 8$ which is the most commonly used value, so that the energy loss per major step is 8.3%. Logarithmic spacing has the advantage that the average angular multiple-scattering deflection per step changes little from step to step [31]. The

average energy loss per major step is evaluated by the total stopping power quantity *dE/ds*

$$E_{n-1} - E_n = -\int_{s_{n-1}}^{s_n} \frac{dE}{ds} ds \tag{2-2}$$

Before the beginning of electron transport calculations, all necessary data are calculated. These data include energy grid, stopping powers, electron ranges, energy steps lengths, substeps lengths, and probability distributions of angular deflections and for production of secondary electrons. Then, at the beginning of each major step, the energy loss rate is sampled from the Landau distribution [74]. The direction of the electron can change at the end of each substep and the deflection angle can be sampled using Gudsmit-Sanderson distribution [73]. The projected energy for the electron at the end of each substep is calculated based on the current sampled energy loss rate and the substep length. The production of the secondary particles are examined at substeps level and the energy of the secondary electron is sampled from an appropriate probability distribution which is based on Møller cross section [76]. The angle between the primary direction and the direction of the secondary electron is determined by momentum conservation.

The number of substeps n is determined empirically, based on material atomic number, and range from $n = 2$ for $Z < 6$ and $n = 15$ for $Z > 91$. However, in some circumstances, it may be desirable to increase the value of n for a given material, such as when the material-region is very small so that more substeps are necessary to improve the accuracy of the simulation.

In this work, the condensed walk Monte Carlo was used to evaluate electron energy spectrum from a uniformly distributed ^{90}Y source which was then used in the analog Monte Carlo code to evaluate the microscopic quantities. Also, the condensed walk Monte Carlo was used to evaluate macroscopic dose quantities such as the point kernels or the radial dose distribution from a ^{90}Y point source and the radial dose distribution across a typical cold region (regions within tumor with none or low monoclonal antibodies). Also, electron energy spectra at different distances from a ^{90}Y point source were calculated.

2.4.2 Analog Monte Carlo

Condensed walk Monte Carlo is used widely in different applications such as radiotherapy. It has, however, important limitations in its application. For instance condensed walk Monte Carlo has trouble when the distance to boundaries or geometrical regions is very small, or when dealing with very low-energy transfers close or smaller than the binding energy, or when it has to simulate the transport of low-energy electrons. In many of these cases the condensed walk Monte Carlo technique can not be used. Instead, the analog or event-by-event Monte Carlo simulation is used.

The analog Monte Carlo is utilized to simulate track-length structure, i.e., the spatial distribution of elastic and inelastic events along a radiation track. Track structure is the basic quantity in microdosimetry or in the characterization of the physical aspects of radiation effects.

Electron track structure simulation on a computer requires basic information on the electron cross section in water, an electron transport model, and initial electron energy and position. The evaluation of the electron collision cross section in water (gas phase) has been performed in the next chapter (Chapter 3) starting from 0.198 eV (the lowest threshold of vibrational excitation). The cross section data are presented in simplified analytical forms suitable for use in a Monte Carlo simulation. The electron transport model could be very precise if all the known atomic collision types are included. The initial electron energy is that of the beta spectrum of ^{90}Y which is evaluated numerically (Chapter 4). ^{90}Y radionuclides are assumed to be distributed uniformly within the tumor, thus, they are assumed to be distributed uniformly on the surface of cancer cells.

3. CROSS SECTION EVALUATION

3.1 Introduction

An electron with kinetic energy which exceeds the first electronic excitation threshold, during its passage through a medium, loses its kinetic energy or is deflected from its path. The energy loss events mark the locations of inelastic collisions with the orbital electrons of the medium. Each energy transfer event may then result in ionization or excitation of the molecule. In the ionization case, a secondary electron is generated, which may cause additional ionization and excitation events in the vicinity of the primary energy loss. The molecular ions and excited states formed, rapidly begin to undergo a series of chain reactions either through decomposition or collision with surrounding molecules, then gradually stabilize energetically and spatially until they eventually reach equilibrium. This equilibrium state is often different in its energy, in the spatial distribution of its molecules, and in the kind of newly formed species from the initial state prior to the electron's passage.

The electronic excitation cross section increases rapidly, right above its threshold, until it reaches a maximum. The ionization channels open, slightly above the excitation threshold, hence, ionization cross section dominates in magnitude in the energy domain above the threshold.

The electron kinetic energies degrade rapidly as long as they are exceeding the first electronic excitation threshold. They eventually fall into the sub-excitation domain. In the sub-excitation domain, their energies start to degrade at much slower rate because

they lose small quanta of energy per collision through momentum transfer in elastic scattering and through rotational and vibrational excitations of constituent molecules. Vibrational excitations are the dominant process in the sub-excitation domain, followed by rotational excitation and elastic scattering.

As the nuclear electron approaches the nucleus without being captured, the nuclear Coulomb force deflects it. In most of these deflections, the electron is elastically scattered without a potential loss in its energy.

An incident electron could lose a potentially large amount of energy by the production of Bremsstrahlung photons in the field of the target electrons. Nevertheless, evaluation of Bremsstrahlung cross sections will not be considered here because their importance starts at high energies or high atomic number media. For example, the Bremsstrahlung yield at 1 MeV electrons in water is about 0.36% and it is about 1.09% at 3 MeV [72]. Moreover, Bremsstrahlung photons travel relatively large distances compared with electrons, so that they do not tend to deposit their energies locally.

All cross sections evaluated here, are based on up-to-date experimentally determined cross section data for electron interactions with water vapor medium. Unfortunately, some of the experimental cross section data, for all or part of the energy domain, and particularly at low energy, do not exist. Liquid water is more appropriate for tissue simulation than water vapor, however, water vapor data are used after normalizing to liquid water density. This is because of the shortcoming of experimentally determined cross sections for liquid water. Despite the predicted differences between the cross sections of the two phases, specially at low energy range. There are two experimentally based facts for the differences in the cross sections of the water two phases. First, there is

a decrease in the ionization potential in the liquid water (8.76 eV) compared with the water vapor (12.61 eV) [78]. Second, there are discrete peaks in the distribution of oscillator strength in the low-energy region for water vapor change into a continuous distribution with a wide peak of absorption in the range of 21 eV [79]. Usually, this peak is attributed to collective excitation of the plasmon type [78,80].

Furthermore, the cross sections formulation should be in its simplest shape in order to speed up calculations of Monte Carlo simulation. Thus, simple analytical expressions based on sound physical and mathematical reasoning were used for most types of the electron cross section evaluations.

3.2 Electron Elastic Scattering Cross Section

In elastic scattering, an incident electron interacts with an atom, resulting in the deflection of the electron through an angle. Hence, the electron loses some energy owing to momentum transfer. However, since the center of mass is small because of the large mass difference between the electron and the collided nucleus, the resultant energy transfer is very small and will be ignored. Furthermore, the electron emits photons (i.e., Bremsstrahlung photons) during its acceleration towards the nucleus, due to the Coulomb field, before the collision. Most of these emitted photons have energies in the infrared region [81]. Therefore, this kind of electron energy loss will not be considered and its effect on the cross section is not significant. The elastic differential cross section (DCS) is proportional to the square of atomic number, Z. In its simplest classical treatment, the

atom is represented as an unscreened point nucleus of charge *Ze*. The elastic differential cross section is obtained as follows:

$$\frac{d\sigma_{el}}{d\Omega} = Z^2 \; r_e^2 \left[\frac{1-\beta^2}{\beta^4}\right]\left[\frac{1}{(1-\cos\theta)^2}\right] \tag{3-1}$$

The above equation is the Rutherford's cross section formula [82]. Often, it is modified to include the effect of orbital electron screening

$$\frac{d\sigma_{el}}{d\Omega} = Z^2 \; r_e^2 \left[\frac{1-\beta^2}{\beta^4}\right]\left[\frac{1}{(1-\cos\theta+2\eta)^2}\right] \tag{3-2}$$

η, is the screening parameter given by Molière [83] and modified by Seltzer [2]

$$\eta(Z,T) = \left(\frac{\alpha}{0.885}\right)^2 \left[\frac{Z^{2/3}}{4\tau(\tau+2)}\right]\left[1.13+3.76\left(\frac{\alpha Z}{\beta}\right)^2\left(\frac{\tau}{\tau+1}\right)^{1/2}\right] \tag{3-3}$$

Where

$\alpha \cong 1/137$, is the fine structure constant

$Z = 10$, is the total number of orbital electrons per molecule

$r_e = 2.81794 \times 10^{-13}$ cm, is the classical electron radius

$m_o c^2 = 511003.4$ eV, is the electron rest mass

$\tau = \frac{T}{m_o c^2}$, is the electron kinetic energy (T) in unit of the rest mass

$\beta^2 = 1 - \frac{1}{(1+\tau)^2}$, is the electron relative velocity ($\beta = \frac{v}{c}$)

The Coulomb force of atomic electrons also causes deflections of electrons. The atomic elastic scattering increases with the atomic number. However, nuclear elastic scattering dominates over atomic elastic scattering. The effect of electron scattering with the orbital electrons can be approximated and included in equation (3-2) [84]

$$\frac{d\sigma_{el}}{d\Omega} = Z(Z+1)\, r_e^2 \left[\frac{1-\beta^2}{\beta^4}\right]\left[\frac{1}{(1-\cos\theta+2\eta)^2}\right] \tag{3-4}$$

The total elastic cross section obtained by integrating the differential cross section over all possible scattering angles Ω is

$$\sigma_{el}(T) = \pi Z(Z+1)\, r_e^2 \left[\frac{1-\beta^2}{\beta^4}\right]\left[\frac{1}{\eta(\eta+1)}\right] \tag{3-5}$$

In practice, electron collision cross sections are measured for an ensemble of target molecules with instruments of finite angular and energy resolutions and represent averages over the ensemble and the instrumental ranges of the parameters. Moreover, rotational excitation of water molecules cannot be resolved from elastic scattering with present experimental techniques. Therefore, the experimental data for elastic scattering

cross sections in the low energy domain (where the rotational excitation interactions are the dominant processes) represent a combination of elastic scattering and rotational excitation and de-excitation. The rotational excitation events occur when an incident electron approaches the target from a distance and exerts a torque on molecular motion. The incident electron could also gain energy from molecules through a reveres process, i.e., rotational de-excitation.

The energy loss due to rotational excitation reactions is slightly higher than the energy loss due to momentum conservation in elastic scattering. Rotational excitation cross section measurements for water are rare and their theoretical prediction models are complicated. Consequently, and for the other reasons mentioned previously, the energy loss due to rotational excitation reactions will be ignored but their reaction rate will be combined with the elastic collision rate. Thus, the following analytical form [85] is used instead of equation (3-5) to evaluate the total elastic cross sections for electrons of energies less than or equal to 200 eV

$$\sigma_{el}(T) = 10^{-16}\left[\left(\frac{T^2}{\delta(\delta+T)}\right)\left(\frac{T^{x_1}}{70+T^{x_2}}\right)+\sum_{i=1}^{2}\frac{\gamma_i}{\left(T-\lambda_i\right)^2+\kappa_i}\right] \qquad (3\text{-}6)$$

Where x_1, x_2, δ, γ, κ_1, and κ_2 are parameters obtained by least squares fitting of several experimental data and cover energy range from 0.35 to 1000. eV. The compiled data are from Seng [86], Shyn and Cho [87], Hayashi [88], Johnstone and Newell [89], Katase et al. [90] and Shyn and Grafe [91]. These parameters were evaluated and found to be:

$x_1 = -0.65$

$x_2 = 1.23$

$\delta = 0.0039$

$\gamma_1 = 20.575$

$\gamma_2 = 2794.27$

$\lambda_1 = 0.125$

$\lambda_2 = 13.93$

$\kappa_1 = 0.225$

$\kappa_2 = 396.9$

Figure 3.1 shows the total elastic cross section in water vapor using modified Rutherford's formula and the analytical formula, equations (3-6) and (3-7) respectively.

In a similar way, the differential elastic scattering cross section (DCS) for electron energies beyond 200 eV can be evaluated using equation (3-4). But for energies below or equal to 200 eV, the available experimental data were fitted using the polynomial function

$$\ln\left[\frac{d\sigma_{el}(T,\theta)}{d\Omega}\right] = a_0(T) + a_1(T)\ \theta + a_2(T)\ \theta^2 + a_3(T)\ \theta^3 + a_4(T)\ \theta^4 \qquad (3\text{-}7)$$

where a_0, a_1, a_2, a_3 *and* a_4 are electron energy dependent parameters. The elastic differential scattering cross sections for several incident electron energies are shown in Figure 3.2.

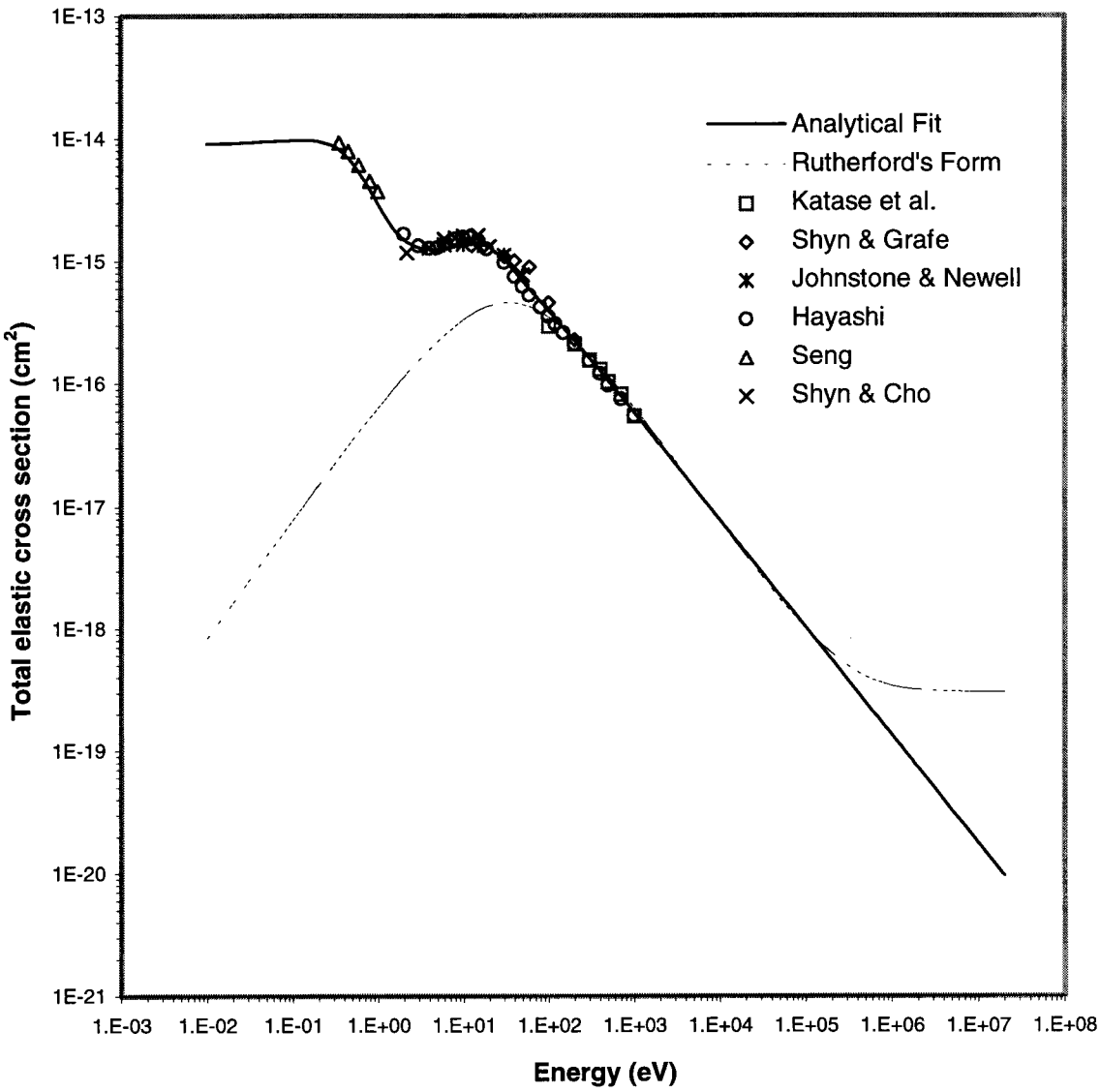

Figure 3.1 Total elastic cross-section , symbols are experimental data of Seng[86], Shyn and Cho [87], Hayashi [88], Johnstone and Newell [89], Katase et al. [90], and Shyn and Grafe [91]; the dot-line is Rutherfored's formula [eq. (3-5)], and the solid-line is the analytical fit [eq. (3-6)].

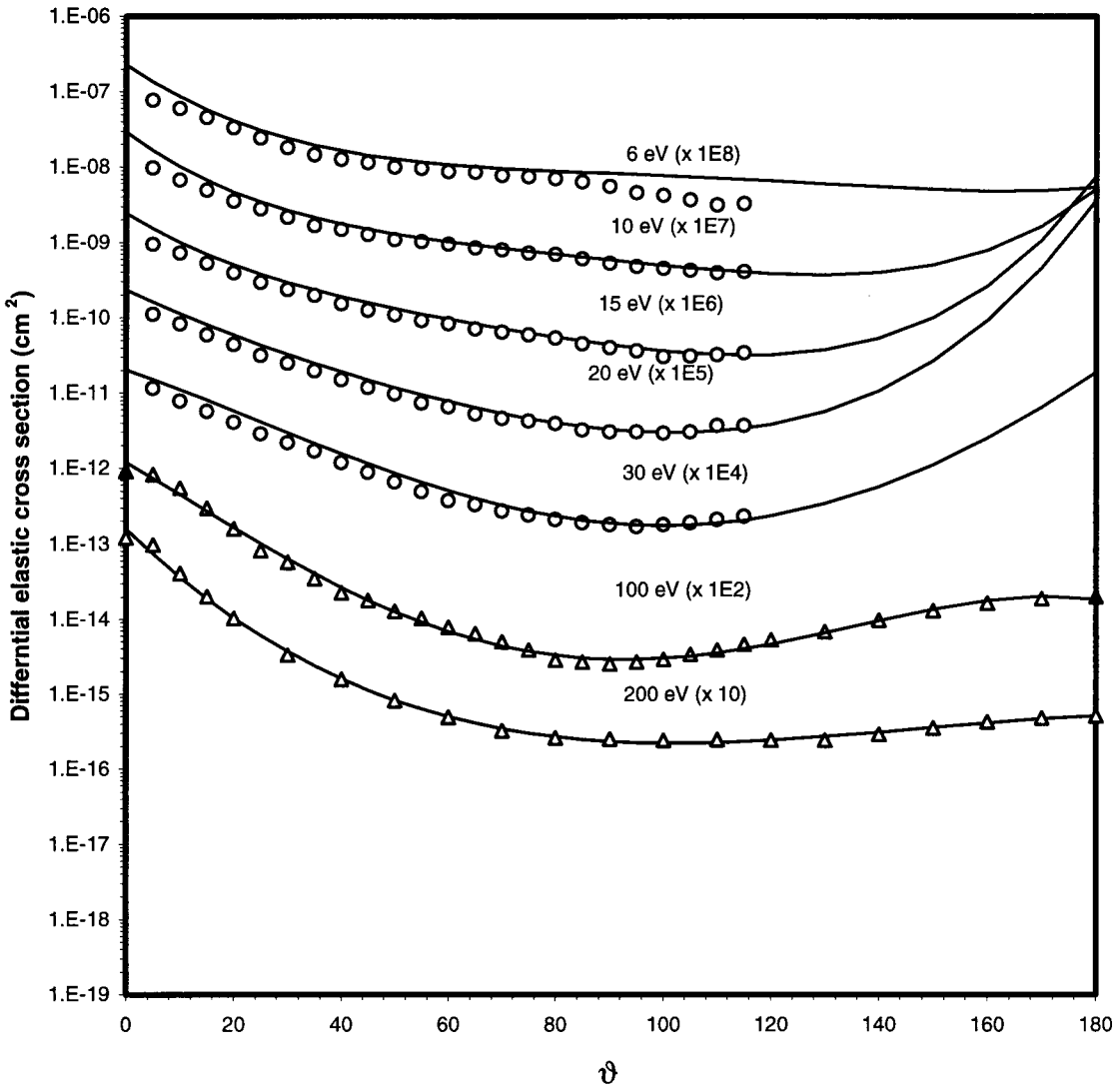

Figure 3.2 Differential elastic cross section , symbols are experimental data; triangles: Johnstone and Newell [89]; circles: Katase et al. [90], and the solid-line is the least square fit [eq. (3-7)].

3.3 Electron-Impact Ionization Cross Section

Electron-impact ionization of orbital electrons constitutes the major mechanism of the inelastic collision processes. When an electron passes an atom at a considerable distance, i.e., large impact parameter, the Coulomb force field of the incident electron affects the atom as a whole. This kind of collision is called a soft or distant collision. In a soft collision, the incident electron could affect the atom by distorting it and producing Čerenkov radiation, by exciting it into a higher energy level and by ionizing it. The impact parameter is defined as the distance between the incident electron track and an interacting atom. When the impact parameter is comparable with atomic dimensions, the incident electron interacts with a single orbital electron. This kind of collision is known as a hard or close collision.

Electron-impact ionization cross sections were evaluated using the binary-encounter Beth model (BEB) [92], for low incident electron energies, i.e., from threshold to 200 eV. For higher incident electron energies, the Weizsäcker-William method is used [93].

The binary-encounter Beth (BEB) model is a simplified form of the binary-encounter dipole model (BED) [94]. The BED model combines the Mott theory modified by the binary-encounter theory [95] and the Beth theory [96]. It provides a formula to calculate the single differential ionization cross section (SDICS), or the energy distribution of the ejected electrons ($d\sigma/dW$) with the ejected electron energy W, for each atomic or molecular orbital. In order to apply BED model, The following data for each orbital electron are required; the electron binding energy B_j, the average kinetic

energy $U_j = \left\langle \mathbf{P}^2 / 2m \right\rangle$ with the bound electron momentum **p** at its mass m, the orbital occupation number N and the continuum dipole oscillator strength $df(w)/dw$. It is more convenient to express the differential cross section in terms of energy variables in units of binding energy B of the electron in a sub-shell

$$\frac{d\sigma^j(T,W)}{dW} = \frac{S}{B_j(t+u+1)}\left\{\frac{(N_i/N)-2}{t+1}\left(\frac{1}{w+1}+\frac{1}{t-w}\right)+\right.$$

$$\left.+\left[2-(N_i/N)^2\right]\left[\frac{1}{(w+1)^2}+\frac{1}{(t-w)^2}\right]+\frac{\ln t}{N(w+1)}\frac{df(w)}{dw}\right\} \qquad (3\text{-}8)$$

where

$t = \dfrac{T}{B_j}$, is the reduced incident electron kinetic energy

$w = \dfrac{W}{B_j}$, is the reduced ejected electron kinetic energy

$u = \dfrac{U_j}{B_j}$, is the reduced average electron kinetic energy in sub-shell j

$S = 4\pi a_o^2 N\left(\dfrac{R}{B_j}\right)$

$a_o = 5.29\,x\,10^{-9}$ cm, is the Bohr radius

R = 13.6 eV, is the Rydberg energy

N, is the number of bound electrons in the sub-shell

and

$$N_i = \int_0^{\infty} \frac{df(w)}{dw} dw \tag{3-9}$$

$\frac{df(w)}{dw}$, is the orbital differential oscillator strength

In the BEB model, the differential oscillator strength is simplified into a form that can be integrated to obtain N_i [92]

$$\frac{df(w)}{dw} = \frac{b}{(w+1)^2} + \ldots. \tag{3-10}$$

where b, is a constant.

Considering only the first term, then

$$N_i = b \int_0^{\infty} \frac{dw}{(w+1)^2}$$

$$= b \tag{3-11}$$

Rewriting equation (3-8)

$$\frac{d\sigma^j(T,w)}{dw} = S \sum_{n=1}^{3} F_n(t)\left[f_n(w) + f_n(t-w)\right] \tag{3-12}$$

where

$$F_1 = \frac{-F_2}{t+1} \tag{3-13a}$$

$$F_2 = \frac{2-Q}{t+u+1} \tag{3-13b}$$

$$F_3 = \frac{Q \ln t}{t+u+1} \tag{3-13c}$$

and

$$f_n(w) = (w+1)^{-n} \tag{3-14a}$$

$$f_n(t-w) = (t-w)^{-n} \tag{3-14b}$$

$$Q = \frac{2B_j M_i^2}{NR} \tag{3-15}$$

Where M_i^2, is a constant related to the differential oscillator strength by

$$M_i^2 = \frac{R}{B_j} \int_0^\infty \frac{1}{w+1} \frac{df(w)}{dw} dw \tag{3-16}$$

Substituting equation (3-10) into equation (3-16)

$$M_i^2 = \frac{Rb}{B_j} \int_0^\infty \frac{dw}{(w+1)^3}$$

$$= \frac{Rb}{2B_j} \tag{3-17}$$

Combining equations (3-11) and (3-15)

$$M_i^2 = \frac{RN_i}{2B_j} \tag{3-18}$$

and

$$Q = \frac{N_i}{N} \tag{3-19}$$

If E is the energy lost in the collision, the primary electron energy, T', after collision and the ejected electron energy, W, are

$$T' = T - E \tag{3-20}$$

$$W = E - B_j \tag{3-21}$$

However, because the scattered and ejected electrons are indistinguishable, it is customary to call the faster one of the two after the collision the primary electron, and the slower one the secondary electron.

The total ionization cross section per shell σ_{Ion}^{j} is obtained by integrating equation (3-12) over w, actually from w_0 to w_{max} where

$$w_0 = 0.0 \tag{3-22.a}$$

$$w_{\max} = \frac{t-1}{2} \tag{3-22.b}$$

so that,

$$\sigma_{Ion}^{j}(T) = \int_0^{w_{\max}} \frac{d\sigma^{j}}{dw} dw$$

$$\sigma_{Ion}^{j}(T) = \frac{S}{(t+u+1)} \left\{ \frac{Q \ln t}{2} \left(1 - \frac{1}{t^2} \right) + (2-Q) \left[\left(1 - \frac{1}{t} \right) - \frac{\ln t}{t+1} \right] \right\} \tag{3-23}$$

In the current application, instead of evaluating the value of M_i^2, which is needed to obtain Q, equations (3-12) and (3-23) were further approximated by setting Q equal to one, then check the compliance of the total ionization cross sections evaluated by this model with the experimental data. Consequently, these two equations will be

$$\frac{d\sigma(w,T)}{dw} = \frac{S}{t+u+1} \left\{ \begin{array}{l} \dfrac{-1}{(t+1)} \left[\dfrac{1}{(w+1)} + \dfrac{1}{(t-w)} \right] + \left[\dfrac{1}{(w+1)^2} + \dfrac{1}{(t-w)^2} \right] \\ + \ln t \left[\dfrac{1}{(w+1)^3} + \dfrac{1}{(t-w)^3} \right] \end{array} \right\} \tag{3-24}$$

and

$$\sigma_{Ion}^{j}(T) = \frac{S}{(t+u+1)} \left\{ \ln t \left[\frac{1}{2} \left(1 - \frac{1}{t^2} \right) - \frac{1}{(1+t)} \right] + 1 - \frac{1}{t} \right\} \tag{3-25}$$

The cross sections must be summed over the sub-shells that contribute to ionization, i.e., j = 1 to 5. As for the values of B_j and U_j , the experimental data are used [97], Table 3.1.

j	Orbital	B_j (eV)	U_j (eV)	N
1	1b1	12.61	122.9	2
2	3a1	14.73	118.4	2
3	1b2	18.55	97.39	2
4	2a1	32.2	142.0	2
5	1a1	589.7	1589.5	2

Table 3.1 Binding (B) and kinetic (U) energies in (eV) and (N) occupation number of water molecule.

The particular design of BED/BEB models were designed to deal with cross sections at low incident electron energies [98]. For higher energies (here, > 200 eV), the Seltzer formula [99] based on Weizsäcker -William method [93] is used instead. In this formula the differential ionization cross sections $d\sigma^{j}(T,W) / dW$ for the jth orbital is written as the sum of the hard or close collision $d\sigma_c^j/dW$ and the soft or distant collision $d\sigma_d^j/dW$

$$\frac{d\sigma^{j}(T,W)}{dW} = \frac{d\sigma_c^j(T,W)}{dW} + \frac{d\sigma_d^j(T,W)}{dW}) \qquad (3\text{-}26)$$

The hard collision part can be obtained according to

$$\frac{d\sigma_c^j(T,W)}{dW} = \frac{2\pi\, r_e^2 m_o c^2}{\beta^2} n_j P_j \left\{ \begin{array}{l} \dfrac{1}{(W+B_j)^2} + \dfrac{1}{(T-W)^2} + \dfrac{1}{T^2}\left(\dfrac{\tau}{\tau+1}\right)^2 \\ -\dfrac{2\tau+1}{(\tau+1)^2}\dfrac{1}{(W+B_j)(T-W)} + G_j \end{array} \right\} \quad (3\text{-}27)$$

where

$$P_j = \frac{T}{(T+B_j+U_j)} \quad (3\text{-}28)$$

and

$$G_j = \frac{8U_j}{3\pi}\left[\frac{1}{(W+B_j)^3} + \frac{1}{(T-W)^3}\right]\left[\tan^{-1}\sqrt{y} + \frac{(y-1)\sqrt{y}}{(y+1)^2}\right]$$

$$y = \frac{W}{U_j} \quad (3\text{-}29)$$

The distant collision is described in terms of the interaction of equivalent field with orbital electrons

$$\frac{d\sigma_d^j(T,W)}{dW} = n_j\, I(E)\, \sigma_{PE}^j(E) \quad (3\text{-}30)$$

Where σ_{PE}^{j}, is the photoionization cross section for the jth orbital (per orbital electron), for an incident photon energy $E = W + B_j$. The virtual electron spectrum integrated over impact parameters $b_{min} < b < b_{max}$ is given by

$$I(E) = \frac{2\alpha}{\pi\beta^2 E}\left(\begin{array}{l}\left\{\left[x_{\min}K_0(x_{\min})\,K_1(x_{\min})\right] - \frac{x_{\min}^2}{2}\left[K_1{}^2(x_{\min}) - K_0^2(x_{\min})\right]\right\} \\ -\left\{x_{\min}K_0(x_{\max})\,K_1(x_{\max}) - \left(\frac{x_{\max}^2}{2}\right)\left[K_1^2(x_{\max}) - K_0^2(x_{\max})\right]\right\}\end{array}\right) \tag{3-31}$$

where

$$x_{\min} = \frac{E\,b_{\min}}{\hbar c}\frac{\sqrt{1-\beta^2}}{\beta} \tag{3-32}$$

$$x_{\max} = \frac{E\,b_{\max}}{\hbar c}\frac{\sqrt{1-\beta^2}}{\beta} \tag{3-33}$$

K_0 and K_1 are the Bessel functions of zeroth and first orders, $\hbar$ is the reduced Plank's constant, and c is the speed of light. The maximum impact parameter is given by

$$b_{\max} = \frac{1.123\,\hbar c}{B_j}\frac{\beta}{\sqrt{1-\beta^2}} \tag{3-34}$$

and the minimum impact parameter $b_{min} = \langle r \rangle_j$ is the expectation value of the electron radius for the orbital *j*. The atomic electron radii $\langle r \rangle_j$ in Bohr units (i.e., $\langle r \rangle_j / a_0$) are listed in Table 3.2 [100].

Atomic orbital	$\langle r \rangle / a_0$
H_{1s}	1.000
O_{2p}	0.833
O_{2s}	0.875
O_{1s}	0.129

Table 3.2 Atomic electron radii in Bohr units.

The molecular orbital radii $\langle r \rangle_j$, similarly, the photoionization cross sections, were assembled from a linear combinations using weighted coefficients N_s given by Siegbahn et al. [101] divided by the number of electrons per molecular orbital N_j, Table (3.3) .

j	Orbital	N_j	Orbital Shell	N_s	$\langle r \rangle_j / a_0$
1	1b1	2	O_{2p}	2.000	0.833
2	3a1	2	H_{1s} O_{2p} O_{2s}	0.340 0.200 1.460	0.867
3	1b2	2	H_{1s} O_{2p}	0.820 1.180	0.901
4	2a1	2	H_{1s} O_{2s}	0.500 1.500	0.906
5	1a1	2	O_{1s}	2.000	0.129

Table 3.3 Water molecule orbital electron radii in Bohr units.

The partial ionization cross section for a molecular orbital is given by

$$\sigma_{Ion}^{j}(T) = \int_{0}^{\frac{T-B_j}{2}} \frac{d\sigma^{j}(T,W)}{dW} dW \tag{3-35}$$

The cross section must be summed over the sub-shells that contribute to ionization

$$\sigma_{Ion}(T) = \sum_{j=1}^{5} \sigma_{Ion}^{j}(T) \tag{3-36}$$

Evaluating partial, hence, total ionization cross sections using Seltzer's approach, i.e., equations (3-35) and (3-36), requires relatively intensive computations. In order to simplify the ionization cross section calculations, the formula obtained based on Bethe approximation (the so called Fano plot) [72,102], was used to evaluate partial ionization cross section

$$\sigma_{Ion}^{j}(T) = \frac{4\pi a_0^2 \alpha^2}{\beta^2}\left\{b_j + a_j\left[\ln\left(\frac{\beta^2}{1-\beta^2}\right) - \beta^2\right]\right\} \tag{3-37}$$

and total ionization cross section

$$\sigma_{Ion}(T) = \frac{4\pi a_0^2 \alpha^2}{\beta^2}\left\{b + a\left[\ln\left(\frac{\beta^2}{1-\beta^2}\right) - \beta^2\right]\right\} \tag{3-38}$$

Where a_j and b_j are constants for each orbital j and independent of the electron energy. The cross sections evaluated for water using Seltzer's formula [72] were used to obtain the a_j and b_j values, Table 3.4.

j	1	2	3	4	5
a_j	1.093	0.894	0.670	0.215	0.045
b_j	10.663	8.684	6.445	2.056	0.263

Table 3.4 Evaluated a_j and b_j constants for water molecule orbital electrons.

Hence, the constants a and b for the total ionization cross section

$a = 2.92$

$b = 28.11$

For further computational simplification, the partial ionization cross sections, i.e., the ionization cross section for each orbital of the water molecule were evaluated by multiplying the total ionization cross section by the relative probability P_j for ionization from different orbitals

$$\sigma_{Ion}^{j}(T)=\frac{4\pi a_0^2\alpha^2}{\beta^2}\left\{b+a\left[\ln\left(\frac{\beta^2}{1-\beta^2}\right)-\beta^2\right]\right\}P_j \qquad (3\text{-}39)$$

The fractional partial ionization cross sections for different orbitals were calculated for both low and high primary electron energy domains and shown in Figure 3.3. As it can be seen from the figure, the contribution to the ionization process from the 1a1 orbital (the one with the highest electron binding energy, i.e., B = 589.7 eV) is very low especially at the electron energy domain under consideration (~ 2 MeV). Therefore, Auger electrons, produced by the orbital-electrons re-arrangement following the ionization of this orbital, is not accounted for in this work.

A number of experimental determinations of the total ionization cross section for electrons in water vapor have been compiled and presented together with the theoretically evaluated cross section in Figure 3.4. The experimental data were obtained from the measurements of Schutten et al. (0.1 to 20 keV) [103], Djurić et al. (15 to 150 eV) [104] , Bolorizadeh et al. (50 to 2000 eV) [105] and the data recommended by Hayashi et al. (15 to 1000 eV) based on analysis of the different experimental collision cross sections [88]. Figures 3.5 and 3.6 show the single differential ionization cross section evaluated theoretically for different primary electron energy along with the experimental measurements.

In general, only single ionization is considered and the possibility of multiple ionization in a single electron collision is neglected.

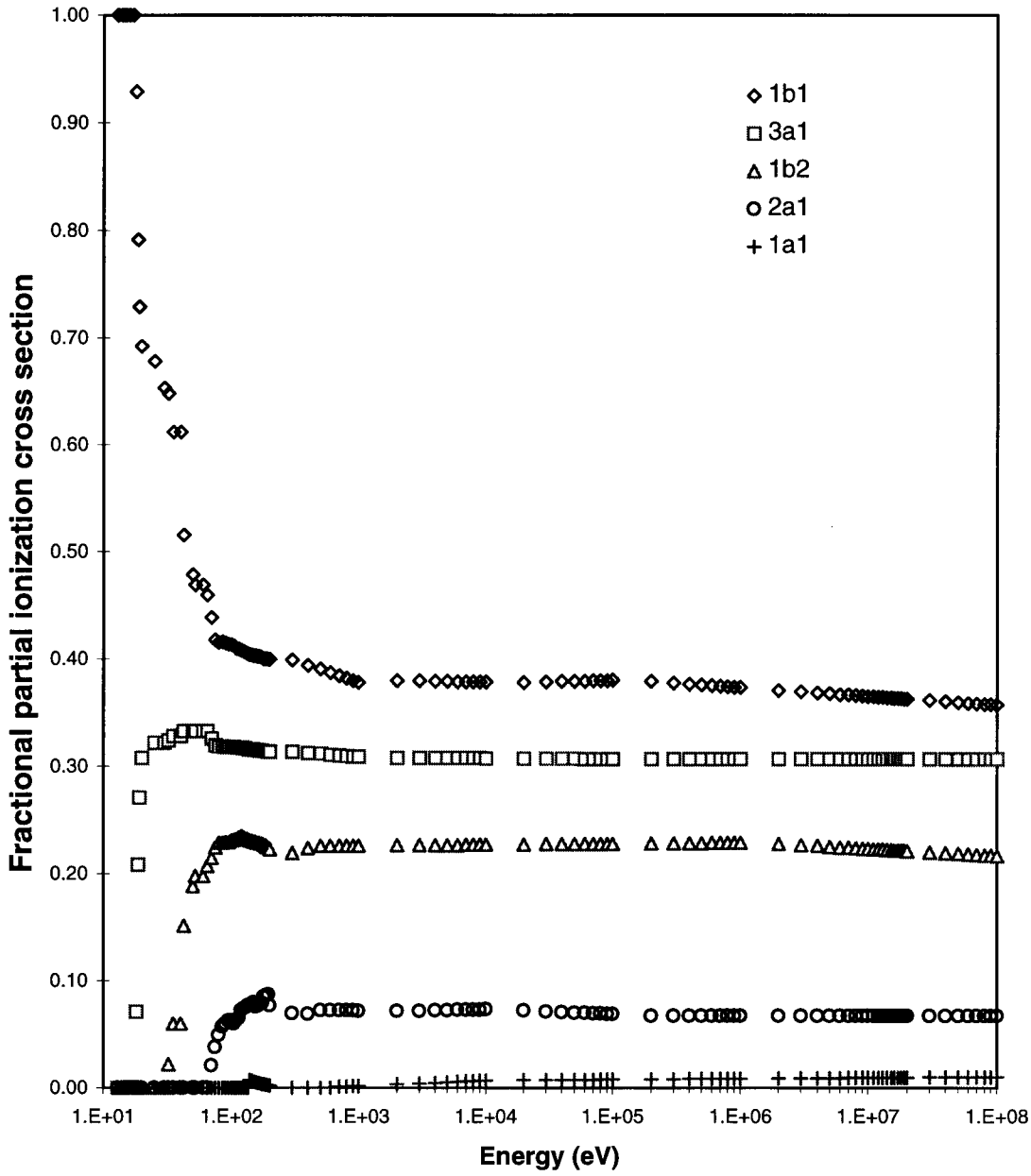

Figure 3.3 Fractional partial ionization cross section

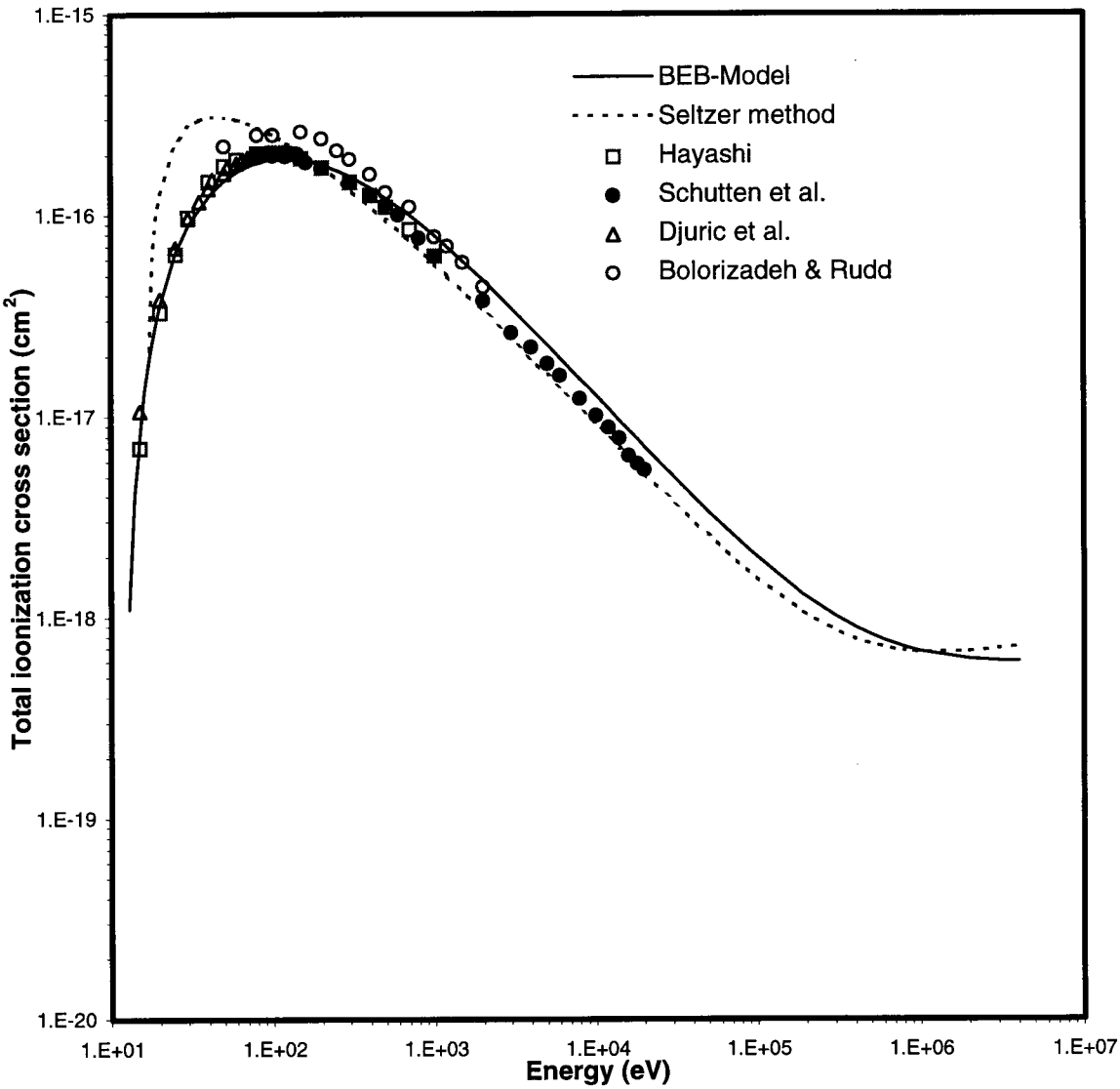

Figure 3.4 Total ionization cross section for water vapor, symbols are experimental data of Hayashi [88]; Schutten et al. [103]; Djuric et al. [104]; and Bolorizadeh and Rudd [105], the solid curve is the BEB-modle and the dot curve is Seltzer method.

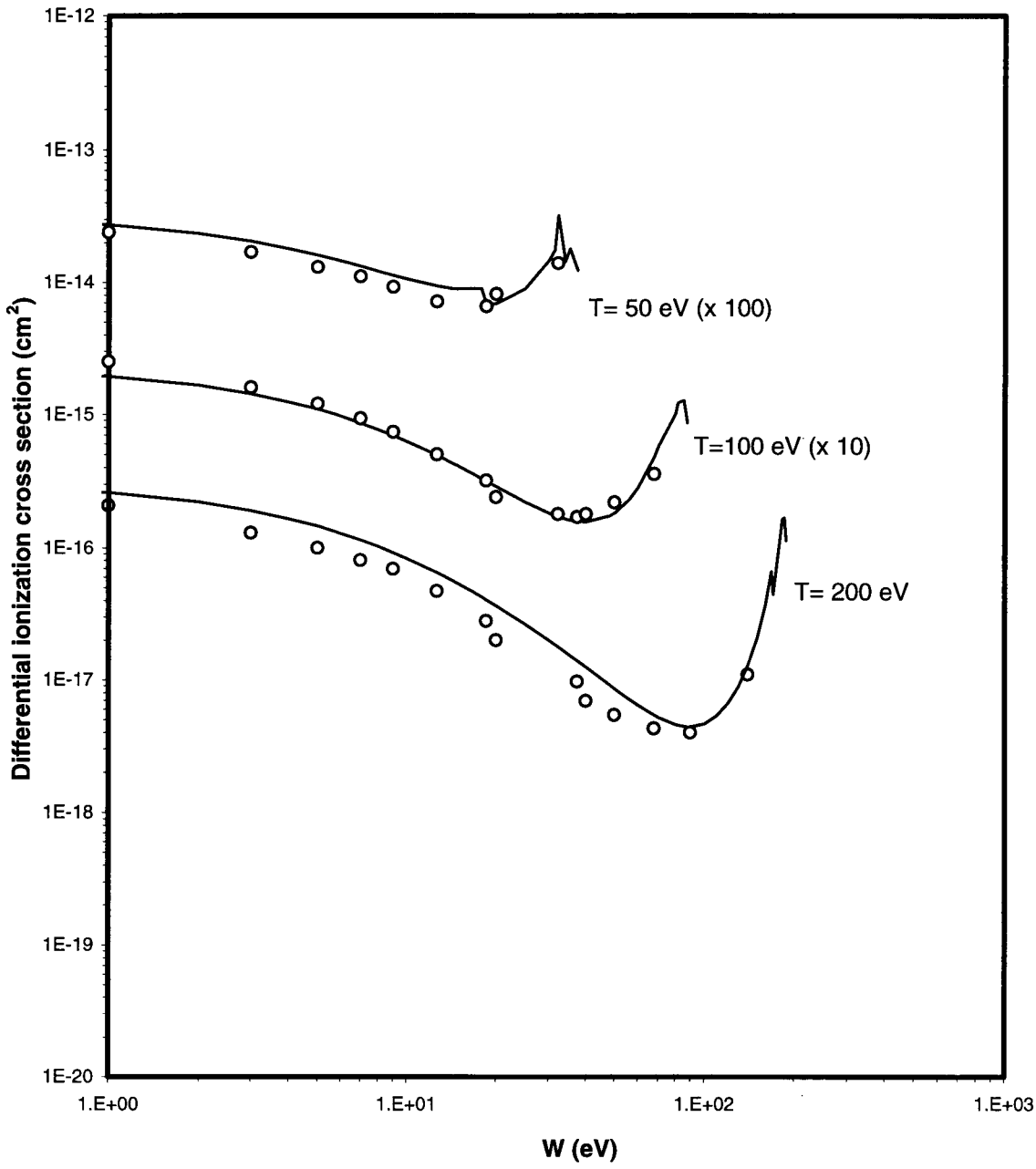

Figure 3.5 Differential ionization cross section for water vapor for primary electron energies of 50, 100 and 200 eV: symbols are the experimental data of Bolorizadeh and Rudd [105].

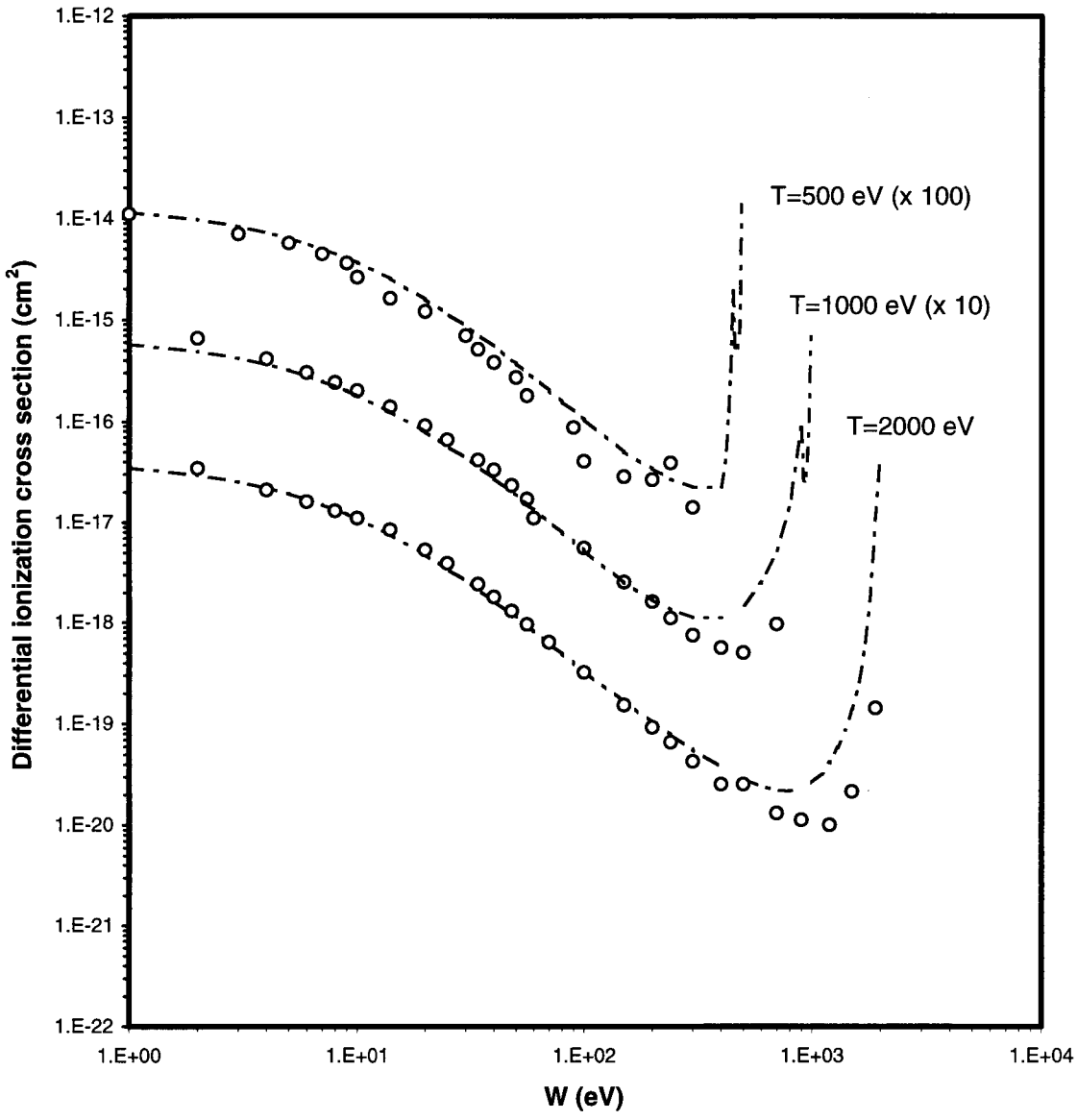

Figure 3.6 Differential ionization cross section for water vapor for primary electron energies of 500, 1000 and 2000 eV; symbols are the experimental data of Bolorizadeh and Rudd [105].

3.4 Electronic Excitation Cross Section

As mentioned at the beginning of the previous section, an incident electron of large impact parameter could transfer part of its kinetic energy to the orbital electrons of an atom or molecule permitting the rearrangement of orbital electrons into one of many possible higher energy excited states. The exact state of the atom or molecule after an excitation event does not need to be known, but rather the scattered electron state after the collision needs to be determined. This is because the de-excitation process which occurs subsequent to a typical excitation collision, and which is dependent on the orbital electrons configuration, does not usually give rise to secondary particles with energy of any consequence, and so can be ignored.

The values of excitation cross sections for different excitation levels increase gradually with increasing impact energy from threshold energies and then slowly decreases at higher energies. Thus, the electronic excitation events have a great importance in the low energy region especially at energies right below the ionization potential.

The electronic excitation cross sections for various excitation states, each of energy threshold W_{exc}^{j}, were evaluated by the analytical form developed by Dayashankar and Green [106]:

$$\sigma_{exc}^{j}(T) = \left(\frac{4\pi a_0^2 R^2 f}{W_{exc}^{j}}\right)\left(\frac{2}{m_0 c^2 \beta^2}\right)\left[\ln\left(\frac{1-\beta^2}{\beta^2}\right) - \beta^2 + \ln\left(\frac{m_0 c^2}{2W_{exc}^{j}}\right) + \Gamma_j\, d\right] \qquad (3\text{-}40)$$

where

$$f = \frac{a W_{exc}^{j}}{R} \tag{3-41}$$

$$\Gamma_j = \frac{(T - W_{exc}^{j})^{\nu}}{\kappa (W_{exc}^{j})^{\nu} + (T - W_{exc}^{j})^{\nu}} \tag{3-42}$$

and

$$\kappa = |p\, d| \tag{3-43}$$

a, ν, p and d are unit-less fitting parameters listed in Table 3.5 [106].

These fitting parameters are based on combinations of the Fano plot, with constants obtained by Berger [72] using recent experimental relativistic cross section data, and the non-relativistic cross section data set assembled by Green et al. [107] and Olivero et al.[108]. For the triplet states, the following analytical form should be used instead of that of equation (3-39), [107,108]

$$\sigma_{exc}^{j}(T) = \left(\frac{4\pi a_0^2 R^2 f}{(W_{exc}^{j})^2} \right) \left(\frac{W_{exc}^{j}}{T} \right)^{\Omega} \left[1 - \left(\frac{W_{exc}^{j}}{T} \right)^{p} \right]^{\nu} \tag{3-44}$$

where $\Omega = 3$, the value of f is taken to be the value of a in Table 3.5 .

Both of the above two analytical forms, equations (3-40) and (3-44), cover non-relativistic as well as relativistic energy regions. Figures 3.5 to 3.9 show the different electronic excitation cross sections $\sigma_{exc}^{j}(T)$ leading to the most important excitation lines and bands calculated using these two analytical forms. The total excitation cross section is shown in Figure 3.10.

State	W_{exc}^{j} (eV)	a	d	v	p
Direct Excitation					
Rydberg (A+B), n=3	10.0	7.913×10^{-2}	-7.710×10^{-1}	1.1	0.8
Rydberg (A+B), n≥4	11.8	4.957×10^{-2}	-7.945×10^{-1}	1.1	0.8
Rydberg (C+D), n=3	11.0	1.450×10^{-1}	-8.027×10^{-1}	1.1	0.8
Rydberg (C+D), n≥4	12.05	1.397×10^{-1}	-8.170×10^{-1}	1.1	0.8
Diffuse Bands	13.32	5.142×10^{-1}	-8.114×10^{-1}	1.1	0.8
Dissociative continuum 1	7.40	9.922×10^{-2}	-7.225×10^{-1}	1.1	0.8
Dissociative continuum 2	9.67	1.148×10^{-1}	-5.191×10^{-1}	1.1	0.8
Triplet 1	4.50	2.116×10^{-2}	3.0	3.0	1.0
Triplet 2	9.81 *(12.5 for fitting)*	1.959×10^{-2}	3.0	1.1	1.0
Dissociative Excitations					
Lyman α	18.50	3.720×10^{-2}	1.604×10^{1}	2.2	1.876
Balmer α	18.50	7.784×10^{-3}	1.603×10^{1}	2.2	1.878
Balmer β	18.60	1.493×10^{-3}	1.458×10^{1}	2.2	1.677
Balmer γ	18.90	6.382×10^{-4}	1.356×10^{1}	2.2	2.161
Balmer δ	19.10	2.453×10^{-4}	1.274×10^{1}	2.2	2.043
OI 8447	17.30	6.607×10^{-4}	1.349×10^{1}	2.2	1.862
OI 7774	17.60	8.247×10^{-6}	3.797×10^{2}	2.2	1.515×10^{-2}
OH 3064	9.10	8.355×10^{-2}	-1.795	0.9663	2.455
OH 2800	11.0	1.331×10^{-5}	3.526×10^{2}	2.749	3.084×10^{-3}

Table 3.5 Analytic cross section parameters for electronic excitation.

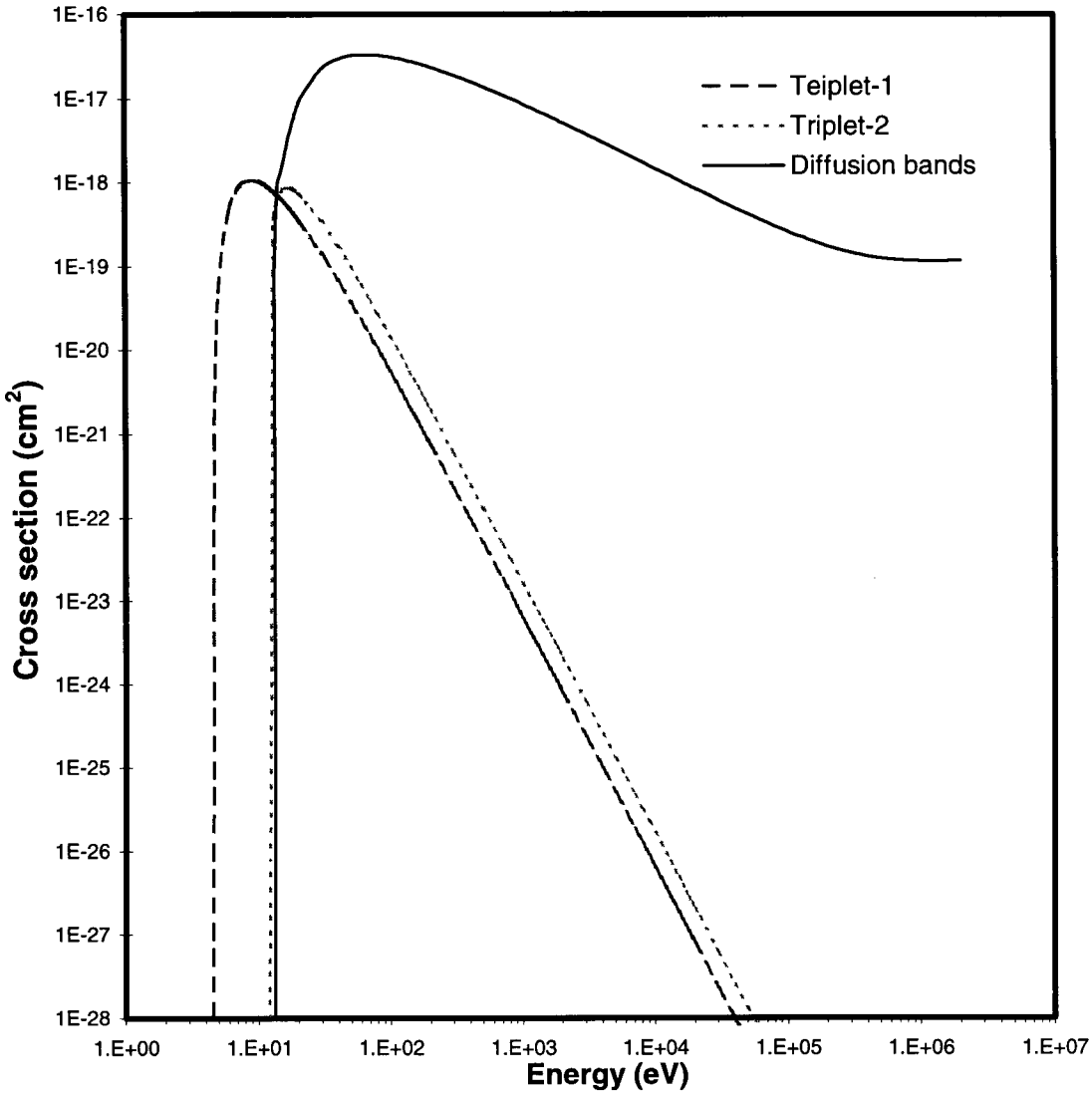

Figure 3.7 Excitation cross section for triplet-1, triplet-2 and diffusion bands.

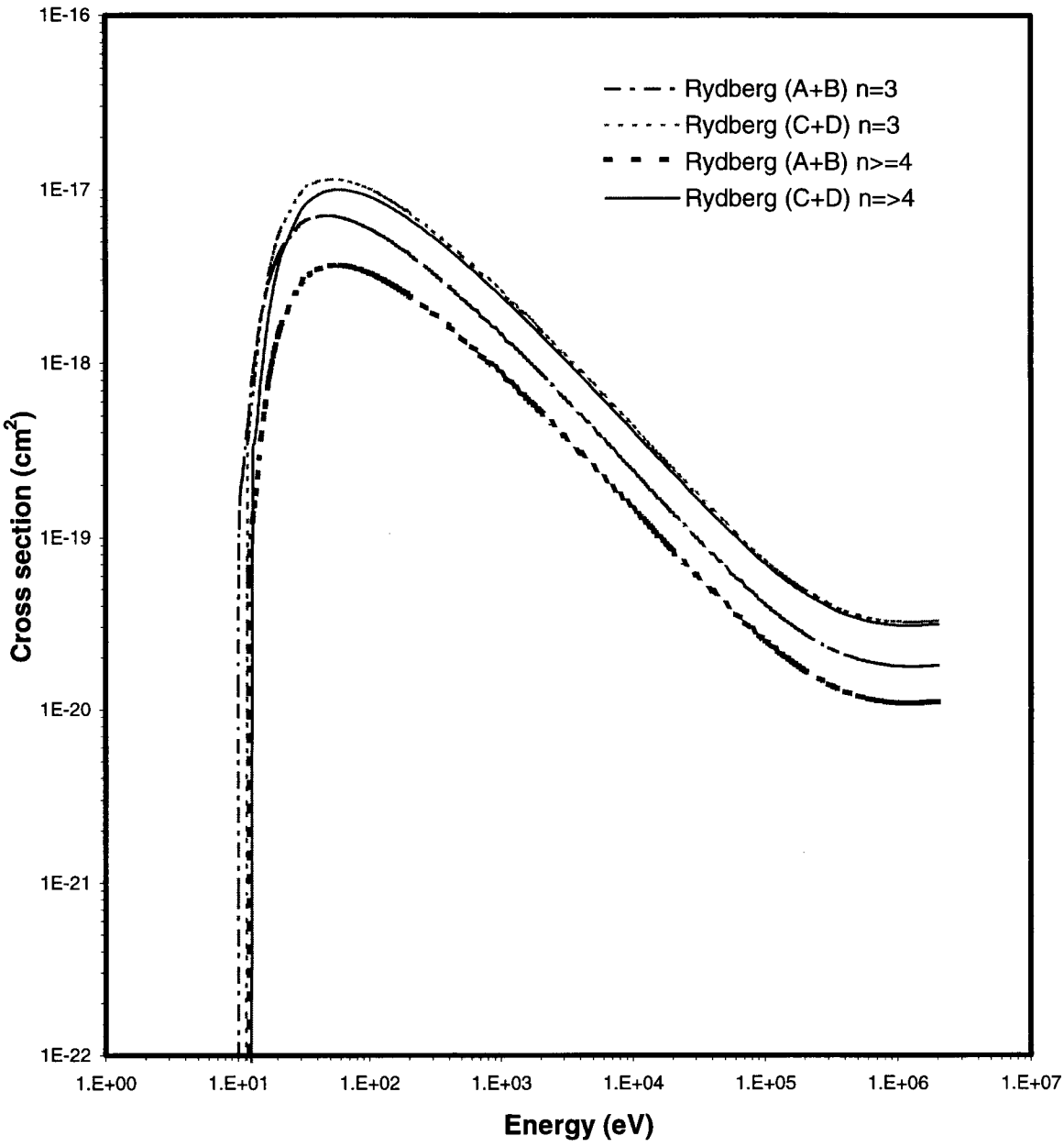

Figure 3.8 Excitation cross sections for Rydberg states (A+B); n=3 and n≥4, and (C+D); n=3 and n≥4.

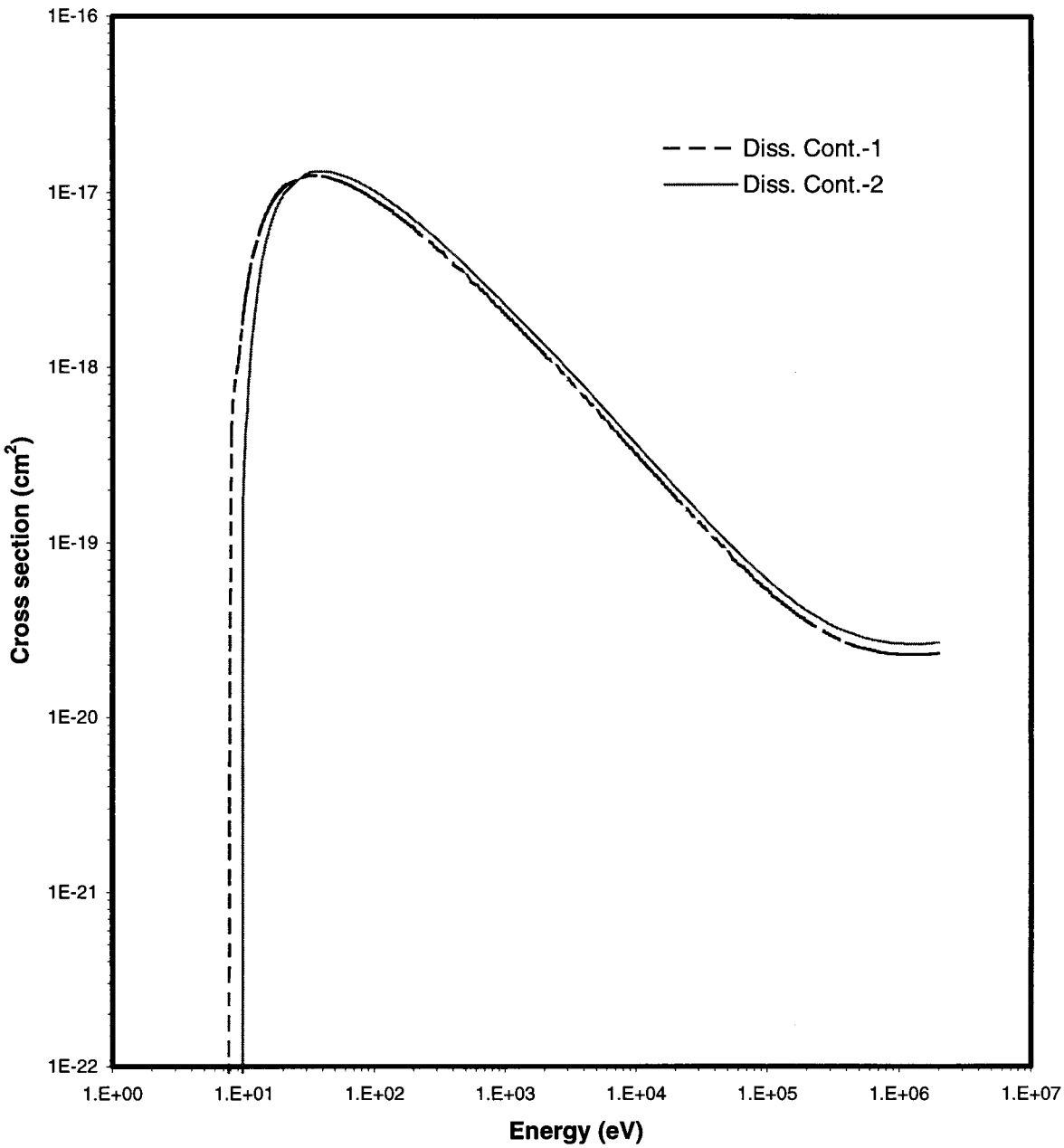

Figure 3.9 Excitation cross sections for dissociative continua 1 and 2 .

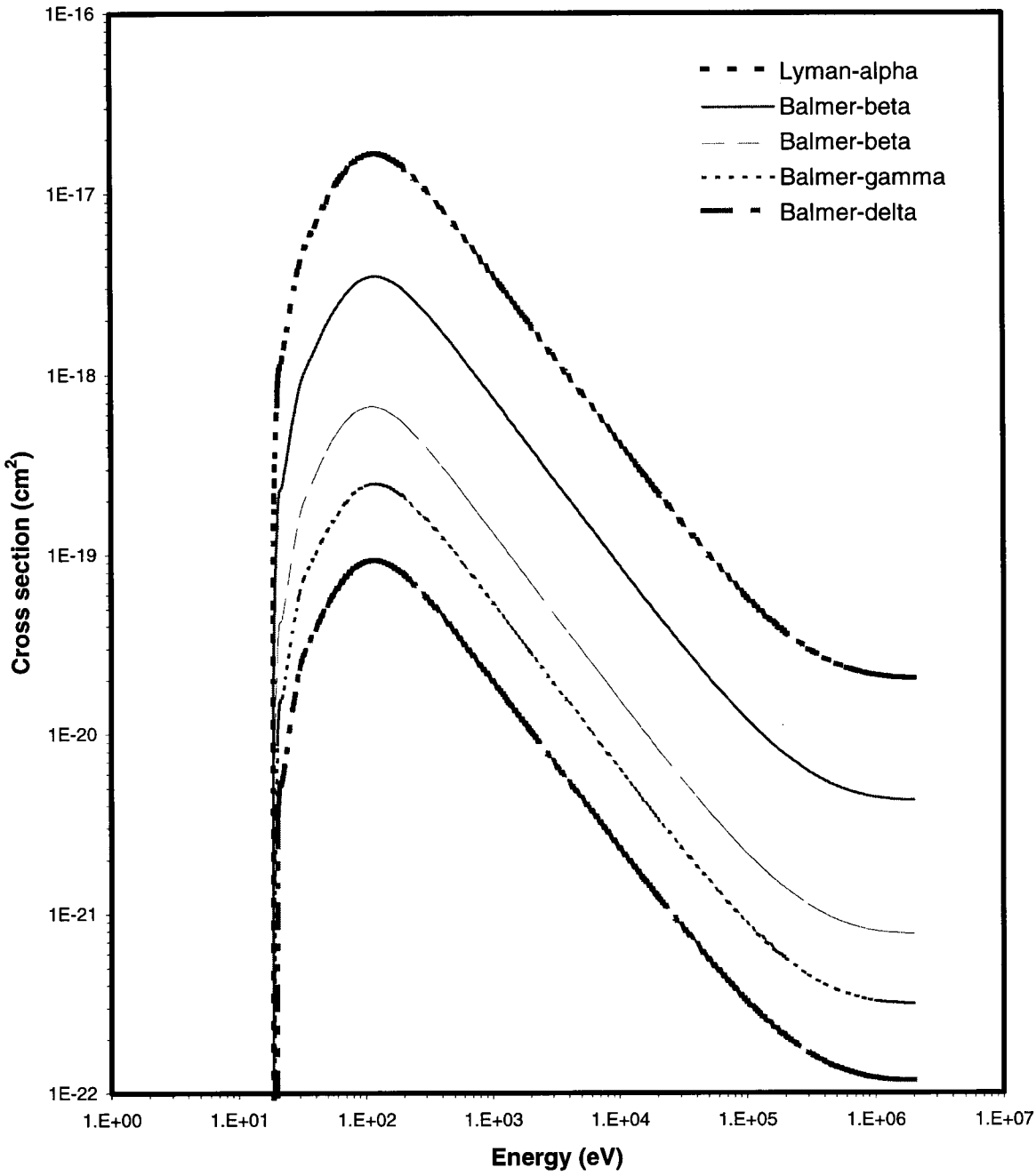

Figure 3.10 Excitation cross sections for Lyman-α, Balmer-α, Balmer-β, Balmer-γ, and Balmer-δ dissociative excitation states.

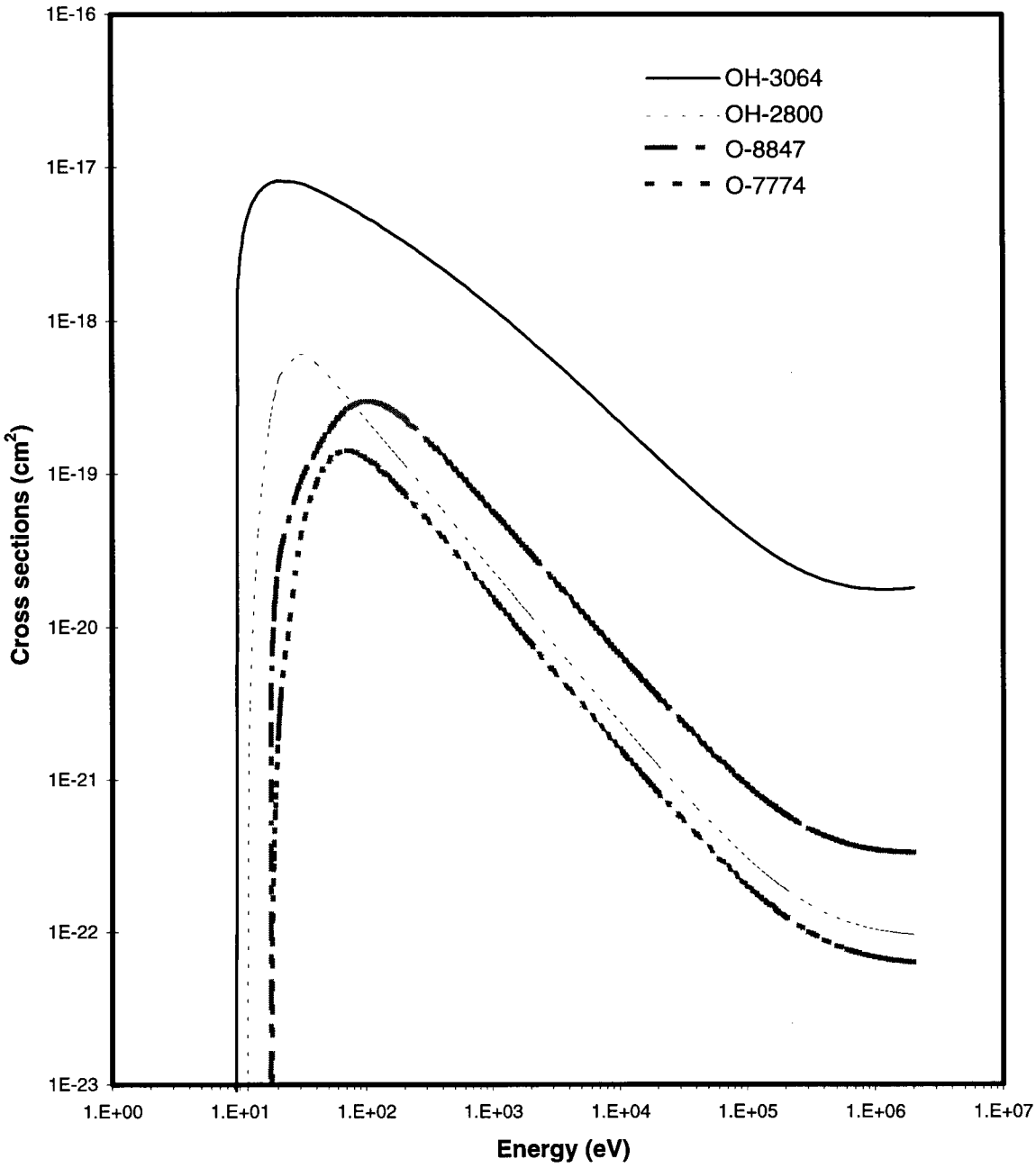

Figure 3.11 Excitation cross sections for OH-3064, OH-2800, O-8447, and O-7774 dissociative excitation states

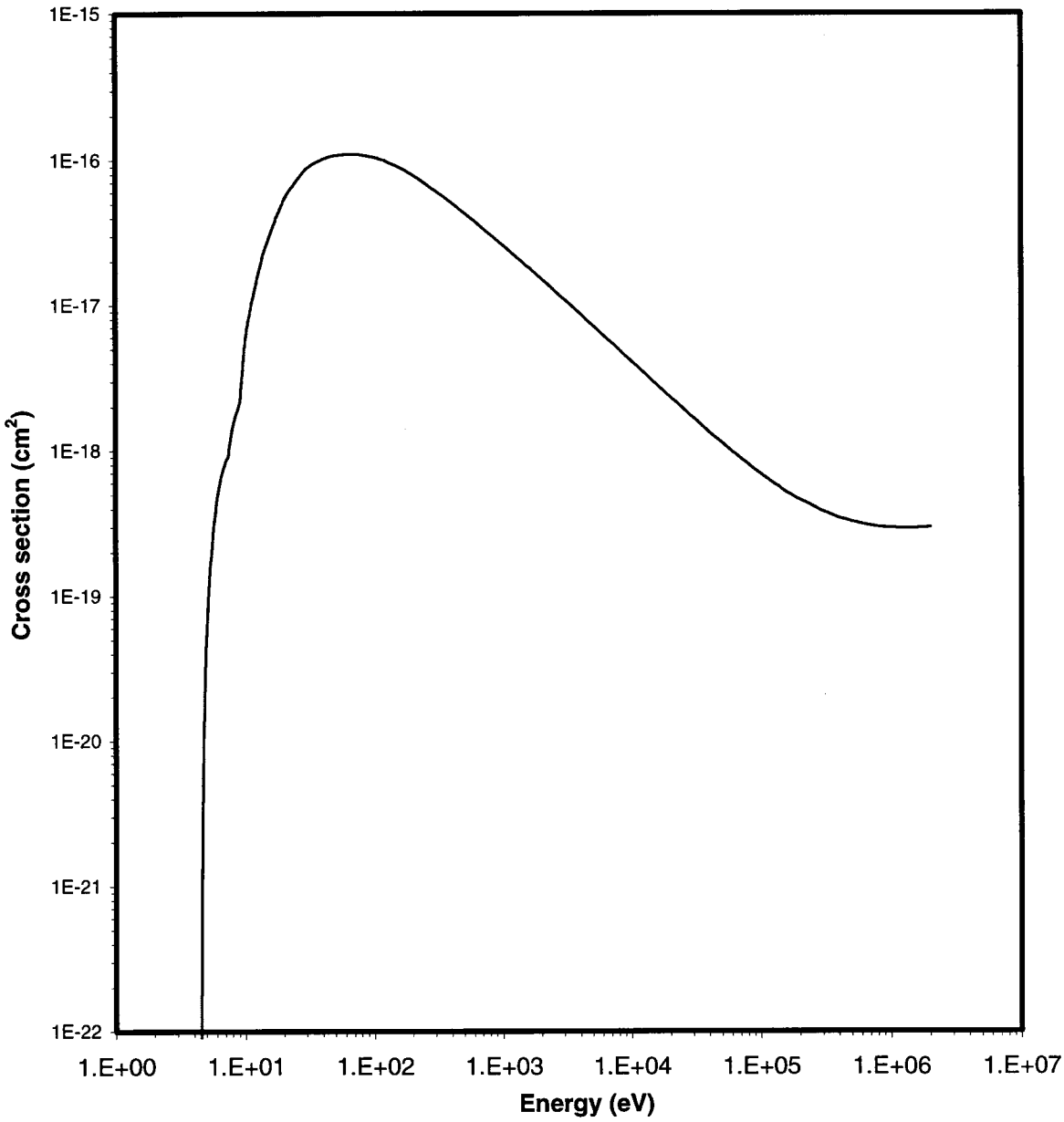

Figure 3.12 Total excitation cross section..

3.5 Dissociative Attachment Cross Section

When a molecule in the ground vibro-electronic state interacts with an electron of specific energy (i.e., resonant energy), the electron is then trapped in the corresponding molecular negative ion, which will start vibrating. During the vibrational motion the negative molecular ion can either detach the extra electron transforming the kinetic energy into vibrational energy of the neutral molecule or ends in the formation of a neutral and negative atom. The first trend of the reaction is the vibratinal excitation reaction (discussed in the following section) and the second trend is the dissociative attachment reaction. Thus, the dissociative attachment reaction is an energy-resonant process proceeds via the negative ion H_2O^- [109-112]:

$$H_2O + e^- \rightarrow \begin{cases} H_2 + O^- \\ H + H + O^- \\ OH + H^- \\ O + H + H^- \end{cases} \tag{3-45}$$

The significance of this process is limited to the energy range of 5 to 20 eV. The dissociative attachment cross sections were evaluated using the analytical form developed by Olivero et al. [108] where

$$\sigma_i^H(T) = \sum_{j=1}^{2} \frac{A_j e^{t_j}}{U_j} \frac{1}{(1+e^{t_j})^2} \tag{3-46}$$

$$\sigma_i^o(T) = \sum_{j=3}^{5} \frac{A_j\, e^{t_j}}{U_j} \frac{1}{(1+e^{t_j})^2} \tag{3-47}$$

and

$$t_j = \frac{T - W_j}{U_j} \tag{3-48}$$

This form is based on the five energy peaks for the formation of H^- (6.5 and 8.6 eV) and O^- (6.9, 8.9 and 11.4 eV) [112]. The values of A_j, U_j and W_j are listed in Table 3.6 [108].

j	Ion Peak	W_j (eV)	A_j (eV . cm^2)	U_j (eV)
1	H-I	6.5	8.45×10^{-18}	0.310
2	H-II	8.6	2.44×10^{-18}	0.468
3	O-I	6.9	3.20×10^{-19}	0.400
4	O-II	8.9	4.75×10^{-19}	0.320
5	O-III	11.4	2.33×10^{-18}	0.663

Table 3.6 Analytic cross section parameters for Dissociative Attachment (Negative Ion) processes.

Figures 3.13 and 3.14 present the dissociative attachment analytical and experimental cross sections for oxygen-ion and hydrogen-ion formations, respectively.

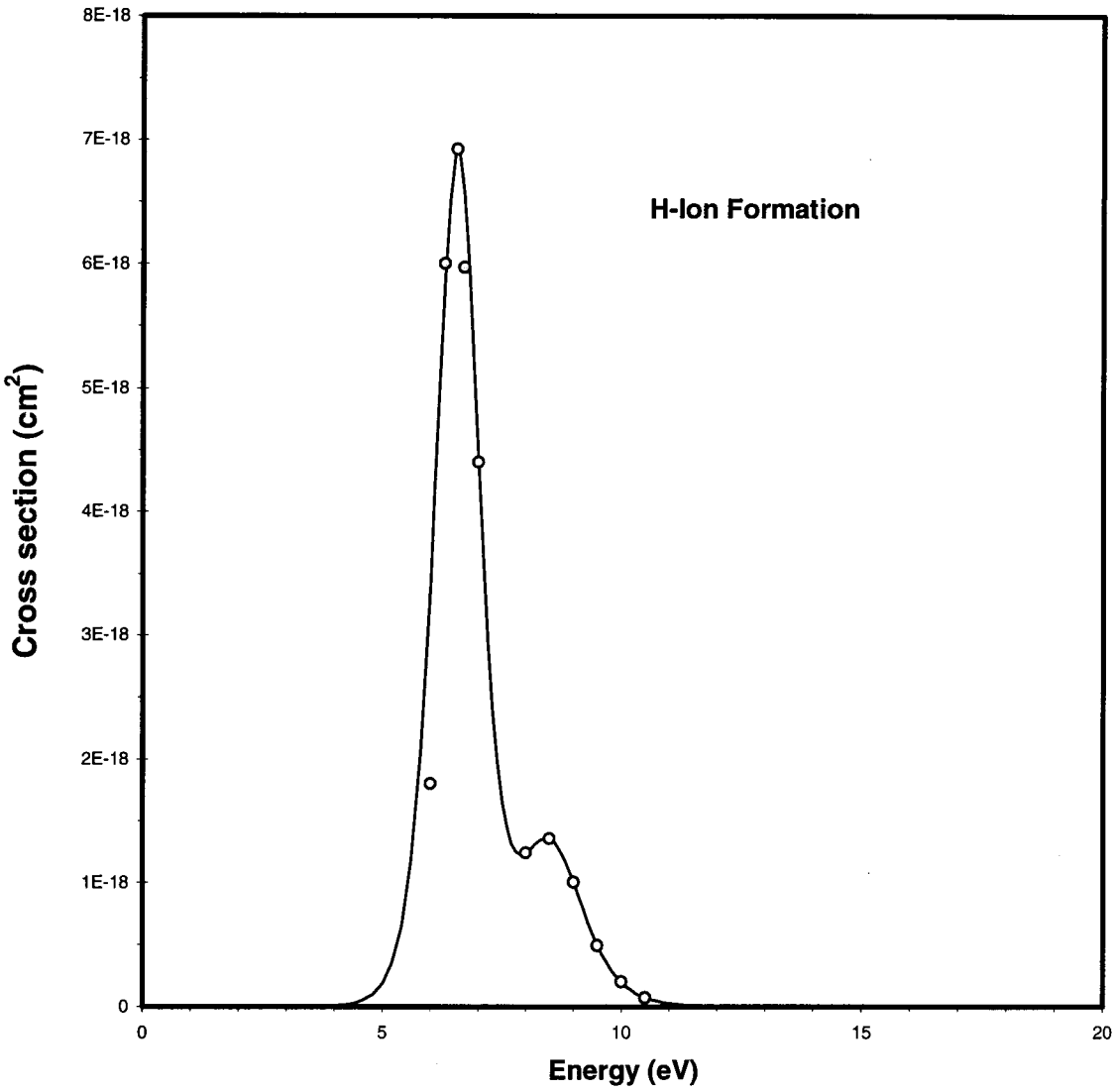

Figure 3.13 Dissiociative-attachment (H-Ion formation) state cross section; the solid line denotes analytical fit, and the symbols are experimental data points [112].

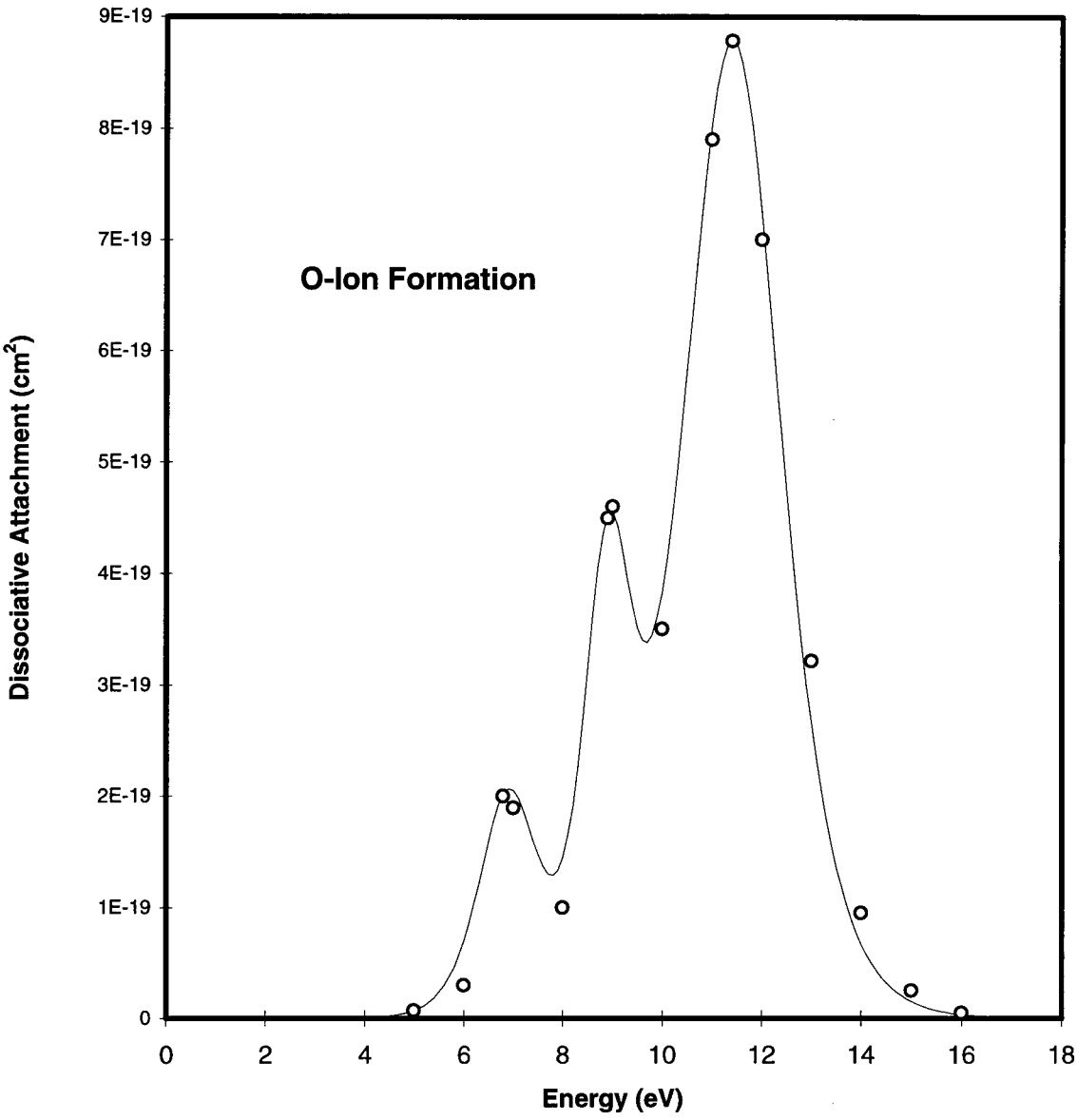

Figure 3.14 Dissiociative-attachment (O-Ion formation) state cross section; the solid line denotes analytical fit, and the symbols are experimental data points [112].

3.6 Vibrational Excitation Cross Section

An incident electron of low kinetic energy, i.e., within the sub-excitation domain, loses its kinetic energy, mainly, through vibrational excitation events. In a vibrational excitation event, an incident electron, with kinetic energy matches one of the unoccupied orbits of the molecule, could be temporarily captured within the molecule, causing an abrupt change in the electromagnetic field of the nuclear motion. This process is a resonance mechanism for vibration excitation. When the captured incident electron escapes from the molecular field, the incident electron leaves the nuclear motion excited. Besides the resonance scattering, there is a direct interaction process which occurs when an incident low-energy electron interacts directly with nuclear motion. The vibrational excitation cross sections were evaluated using a modified form based on Green's analytical form [113]

$$\sigma_{exc}^{v}(T) = \frac{F_v}{\left(W_{exc}^{v}\right)^2}\left[\left(\frac{2X_v}{1+X_v^2}\right)^2 + m_v\left(\frac{2Y_v}{1+Y_v^{n_v}}\right)\right] \tag{3-49}$$

where

$$X_v = \frac{T - W_{exc}^{v}}{\Gamma_v} \tag{3-50}$$

$$Y_v = \frac{T - W_{exc}^{v}}{\Delta_v} \tag{3-51}$$

Γ_v, is the width of the peak or energy distance from threshold to the resonance

Δ_v, is the energy distance from threshold to the broad peak

m_v, is a peak ratio factor

W_{exc}^{v}, is the threshold or excitation energy of the state v

F_v and n_v, are fitting constants.

All of the parameters of equations (3-49) to (3-51) were evaluated using least square fitting of up-to-date experimentally determined vibrational excitation cross sections data. The vibartional excitation cross sections have been separated into three groups. The first group is the cross sections for state v_2 with threshold energy of 0.198 eV. The second group is a combination of two closed threshold states (v_1 +v_3 or v_{13})with a nominal threshold of 0.453 eV. The last group combines all the rest states not included in the first two parts (v_r), assuming an average threshold of 1 eV [88]. The experimental data used to evaluate the analytical form parameters were : the measurements of Seng et al. [114] for the first part (i.e., v_2) and the second part (i.e., v_1 +v_3 or v_{13}) for energy range from thresholds to 10 eV; the measurements of Shyn et al. [115] for the first and second parts for energy range from 2.2 eV to 20 eV; and the vibrational excitation cross sections values recommended by Hayashi [88] for the third part (v_r) since the experimental data for this part do not exist. The evaluated parameters are listed in Table 3.7 .

Figures 3.15 to 3.17 show the vibrational excitation cross sections for each of the three parts, i.e., $\sigma_{exc}^{v_2}$, $\sigma_{exc}^{v_{13}}$ and $\sigma_{exc}^{v_r}$, receptively.

Part	State(s)	W_{exc}^{v} (eV)	F_v	Γ_v (eV)	Δ_v (eV)	m_v	n_v
1	v_2	0.198	0.018×10^{-16}	0.15	4.10	0.085	1.89
2	v_{13}	0.453	0.651×10^{-16}	0.11	7.95	0.147	1.89
3	v_r	1.00	0.500×10^{-16}	0.07	7.50	0.500	1.82

Table 3.7 Parameters for vibrational cross sections evaluation

3.7 Cross Section Accuracy

The evaluated cross sections cover relativistic and non-relativistic electron energies and for several kinds of interactions. The electron kinetic energy loss in a single collision covers wide range of values starts from the lowest vibrational excitation threshold, i.e., 0.198 eV. Most of the formulas used for cross sections evaluation were customized for water vapor and presented in its most simple form. Table 3.8 summaries the sources of the analytical cross sections forms.

It is good practice to verify the evaluated microscopic cross sections using experimental data on macroscopic quantities such as average energy loss due to excitation collisions and mass collision stopping power.

3.7.1 Mean Excitation Energy

The mean energy $\langle W_{exc}(T) \rangle$ transferred in excitation events was calculated as follows:

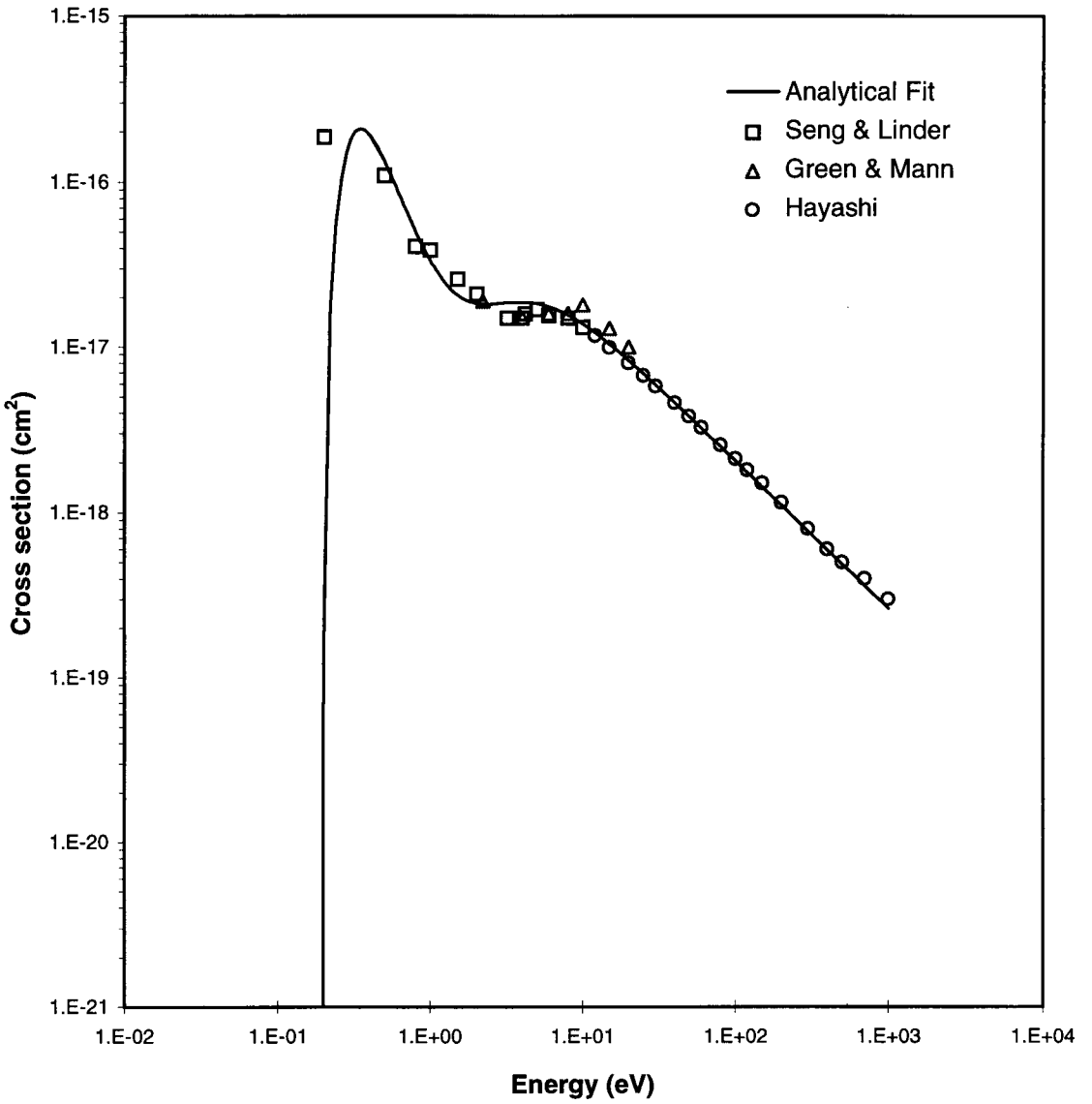

Figure 3.15 Vibrational excitation cross section for the first group (i.e., v_2).

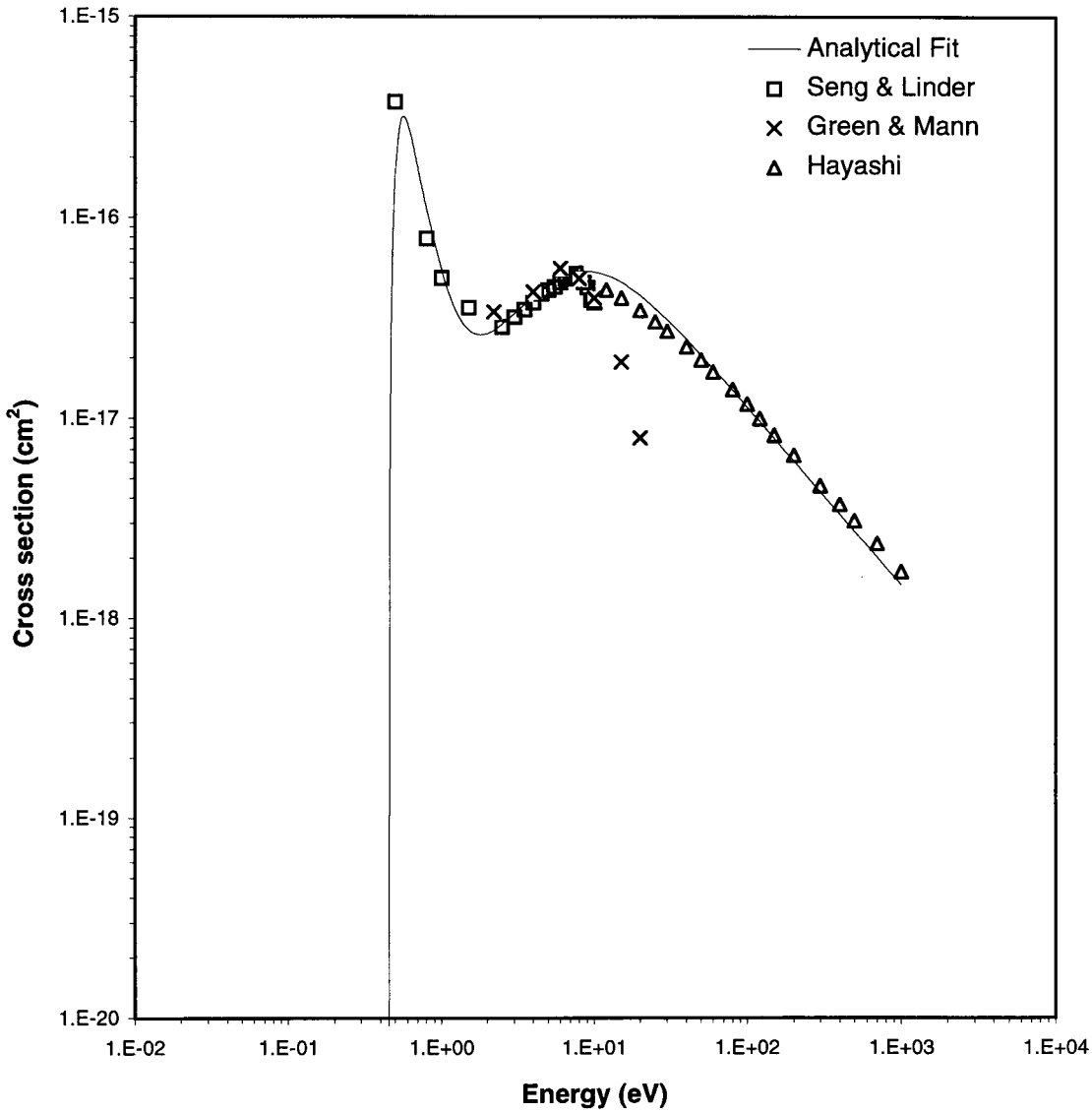

Figure 3.16 Vibrational excitation cross section for the second group (i.e., v_{13}).

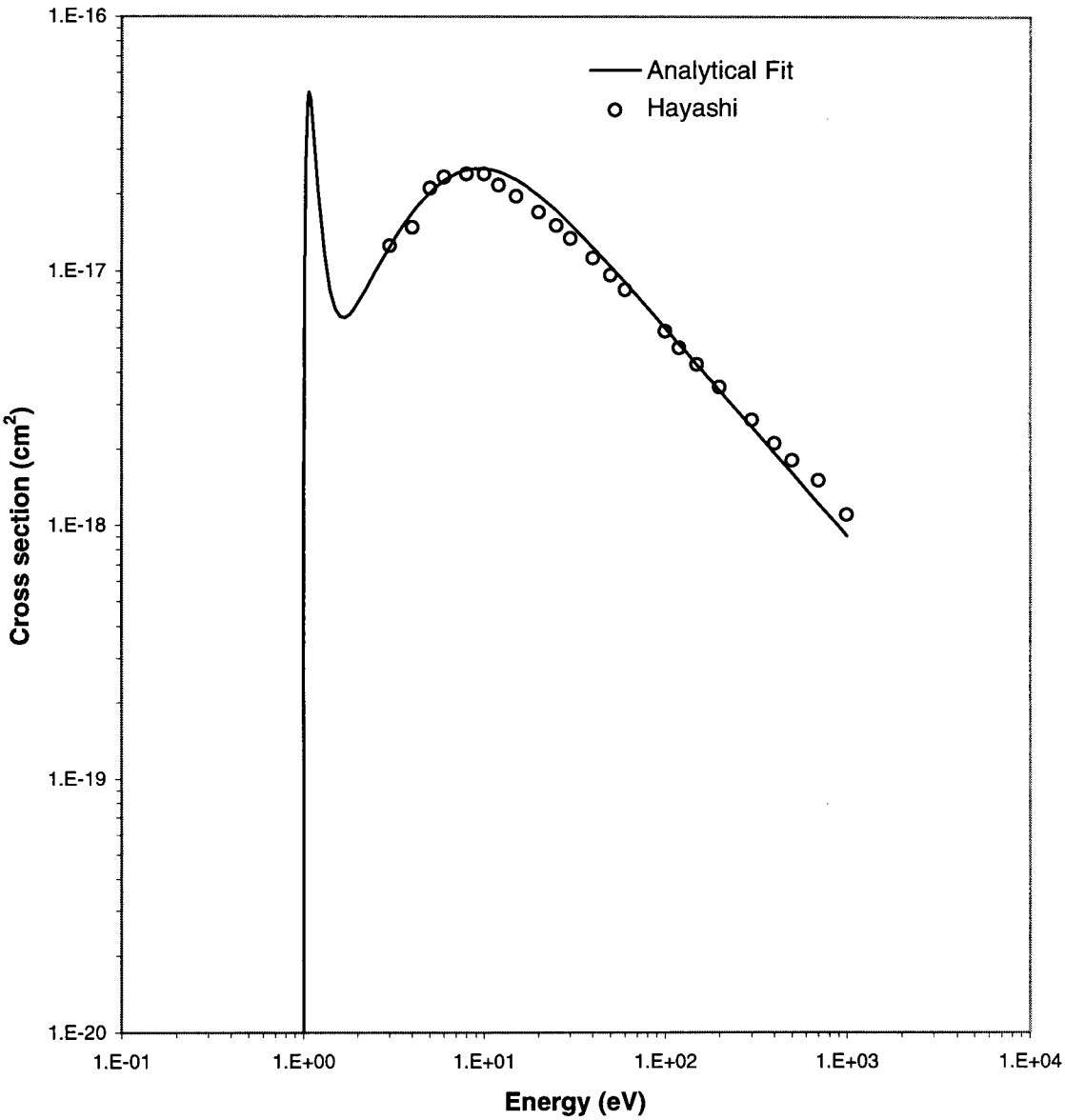

Figure 3.17 Vibrational excitation cross section for the last group (i.e., v_r.).

Collision Type	Energy Range	Cross Section Form	Equation
Elastic	T > 200 eV	Rutherford's theoretical form with Seltzer modified screening parameter.	(3-5)
	T ≤ 200 eV	Analytical form analogous to Porter's with parameters evaluated based on up-to-date experimental data .	(3-6)
Ionization	T > 200 eV	Berger's analytical form (based on Fano plot) with parameters evaluated based on cross sections calcualted using Weiszäcker-William method.	(3-37) (3-25)
	T ≤ 200 eV	Following the theoretical BEB-model with Q-parameter evaluated based on up-to-date cross section experimental data.	
Excitation		Following the analytical forms introduced by Dayasharkar and Green, and Olivero et al..	(3-39) (3-44)
Dissociative Attachment		Following the analytical form introduced by Olivero et al..	
Vibrational Excitation		modified form of Green's analytical formula	(3-48)

Table 3.8 Summary of the formulas used to evaluates cross sections.

$$\left\langle W_{exc}(T) \right\rangle = \frac{\sum W_{exc}^{j}\, \sigma_{exc}^{j}(T)}{\sum \sigma_{exc}^{j}(T)} \tag{3-52}$$

The value of $\left\langle W_{exc}(T) \right\rangle$ was found weakly dependent on electron energy T and rises from about 5 eV to about 13 eV in the energy range between 8 eV and 200 eV, then decreases very slowly , Figure 3.18. This is very much similar to the value obtained by Paretzke and Berger [116]

3.7.2 Mass Collision Stopping Power

A calculation of the mass collision stopping power composed of ionization and excitation components was performed to confirm the reliability of the evaluated ionization and excitation cross sections. The approach used to evaluate the mass collision stopping power is exact and based on the microscopic excitation and ionization cross sections

$$-\frac{1}{\rho}\left(\frac{dT}{dx}\right)_{col} = -\left[\frac{1}{\rho}\left(\frac{dT}{dx}\right)_{kin} + \frac{1}{\rho}\left(\frac{dT}{dx}\right)_{pot} + \frac{1}{\rho}\left(\frac{dT}{dx}\right)_{exc}\right] \tag{3- 53}$$

where

$$-\frac{1}{\rho}\left(\frac{dT}{dx}\right)_{kin} = \frac{N_A}{A}\, \sigma_{ion}(T) \sum_{j=1}^{5} f_j \left\langle W_j \right\rangle \tag{3-54}$$

$$f_j = \sum_{j=1}^{5} \frac{\sigma_{Ion}^{j}(T)}{\sigma_{Ion}(T)} \left\langle W_j \right\rangle \tag{3-55}$$

$$\left\langle W_j \right\rangle = \int_{0}^{\frac{T-B_j}{2}} W \left(\frac{d\sigma_{ion}^{j}}{dW} \right) \frac{dW}{\sigma_{ion}^{j}} \tag{3-56}$$

$$-\frac{1}{\rho}\left(\frac{dT}{dx}\right)_{pot} = \frac{N_{Av}}{A} \sigma_{ion}(T) \sum_{j=1}^{5} \frac{\sigma_{ion}^{j}(T)}{\sigma_{ion}} B_j \tag{3-57}$$

$$-\frac{1}{\rho}\left(\frac{dT}{dx}\right)_{exc} = \frac{N_{Av}}{A} \sigma_{exc}(T) \left\langle W_{exc} \right\rangle \tag{3-58}$$

$\left\langle W_j \right\rangle$ is the mean energy of the secondary electrons emitted from the jth orbital. N_{Av} is the Avogadro number and A is the molecular weight of water. The computed collision mass stopping power is presented in Figure 3.19.

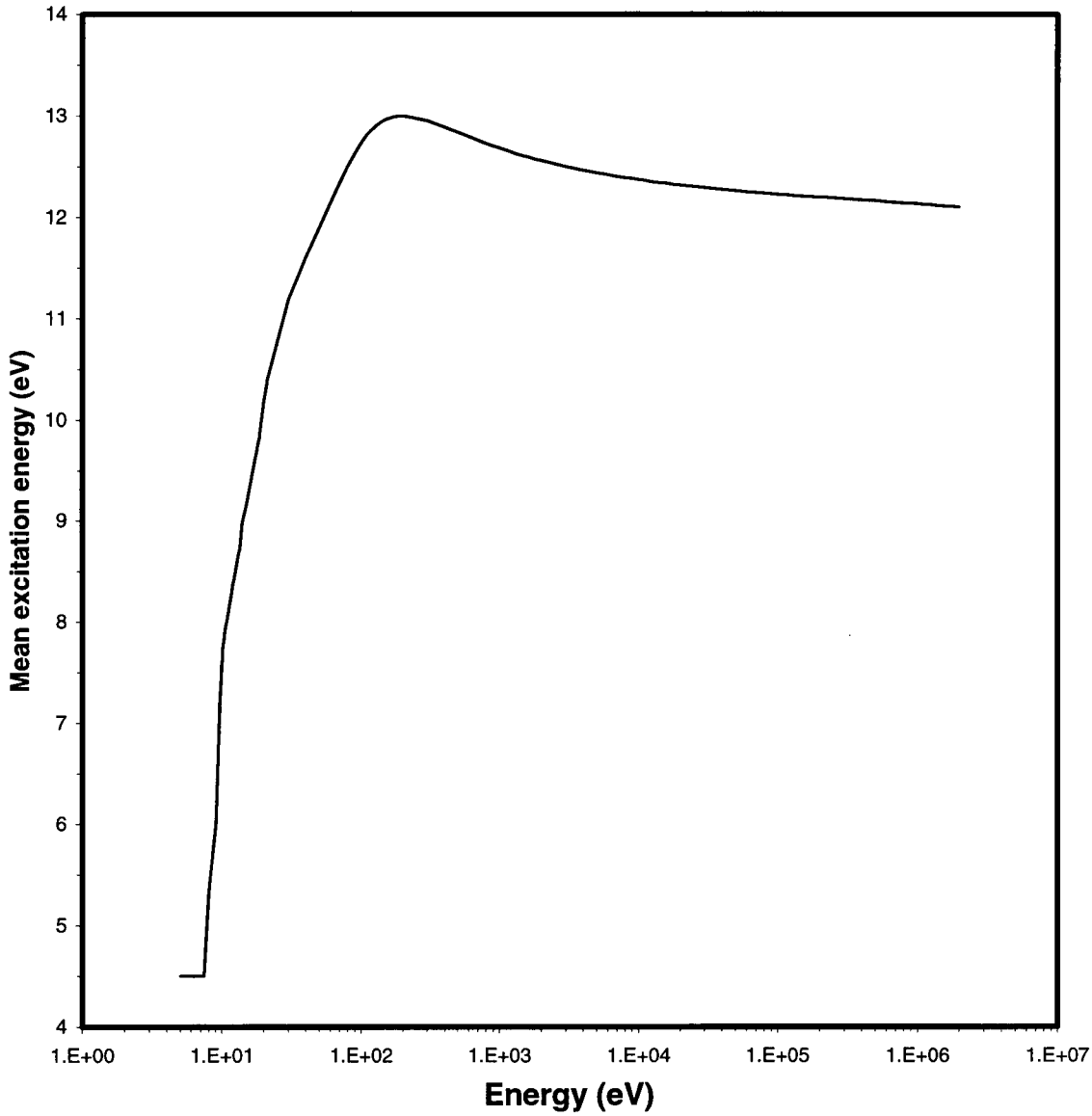

Figure 3.18 Mean excitation energy, $\langle W_{exc}(T) \rangle$ of electrons in water vapor.

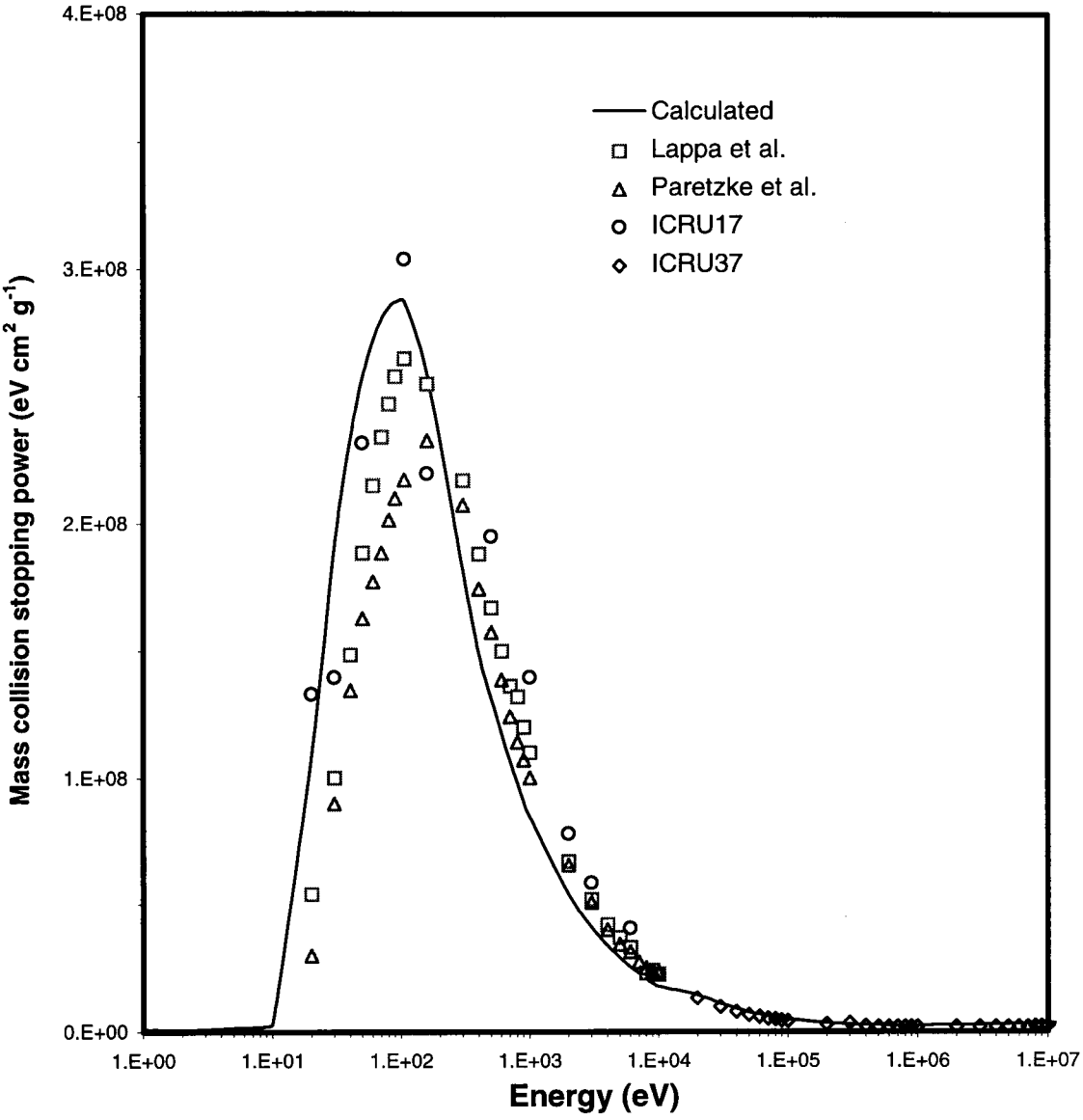

Figure 3.19 Collision mass stopping power of water vapor as a function of electron energy; the solid curve is the caluclated values and the symbols are obtained from Lappa et al. [117], ICRU-16 [118]; ICRU-37 [77]; Paretzke et al. [119].

4. ELECTRON TRACK STRUCTURE SIMULATION

4.1 Monte Carlo Simulation Method

Monte Carlo technique is used to simulate electron track structure with the aid of a computer. It is a numerical analysis method that uses random sampling to construct the solution of a physical or mathematical problem. In general, Monte Carlo method requires four basic elements to solve the particle transport problem [120]:

1- Probability density functions (PDF's) governing the stochastic model of the stochastic process under consideration.

2- Method of sampling the probability distribution functions.

3- Random number generator.

4- Required solution estimators.

When traversing a medium, an electron faces very large number of collisions (compared to neutrons or gamma rays) which results in a small number of catastrophic collisions where it may lose a major fraction of its energy or may be turned through a large angle. Because of the huge number of interactions, it becomes an essential task to minimize the computational steps required in the electron track simulation by following different strategies such as the use of simplified cross section forms to minimize the computation time per history. In this work, different cross section forms based on

theoretical and available experimental data have been evaluated for water vapor specifically (Chapter 3).

Sampling method has a significant effect on the computation speed. For instance, direct sampling is the fastest method but may not be applied easily for non-invertable probability distribution functions.

4.2 Direct Sampling Method

If $f(x)$ is a probability density distribution function, then, the accumulated probability distribution can be written as

$$F(x) = \int_{x_{min}}^{x} f(x')\,dx' \tag{4-1}$$

and the normalized probability distribution function is defined by

$$\frac{F(x)}{F(x_{max})} = \frac{F(x)}{\int_{x_{min}}^{x_{max}} f(x')dx'} \tag{4-2}$$

which is monotonically increasing on the interval [0,1]. If a number ξ ,chosen at random from a uniform distribution on the interval [0,1], is equated to the normalized probability distribution function, then this normalized probability distribution function is inverted to

determine at which value of x the normalized probability distribution function is equal to the random number, as

$$x = F^{-1}(\xi) \tag{4-3}$$

Where F^{-1} represents the inverted function such that

$$\xi = F(x) \tag{4-4}$$

This is the direct sampling method. It is applicable whenever the probability distribution function can be inverted.

4.3 Rejection Sampling Method

In the rejection sampling method, the probability distribution function $f(x)$ is normalized to have a maximum value of one, that is

$$\frac{f(x)}{f^*} = \frac{f(x)}{Max[f(x)]} \tag{4-5}$$

Then, an x value ($x_{min} \leq x \leq x_{max}$) is sampled based on generated random number ξ_1

$$x = x_{\min} + (x_{\max} - x_{\min})\,\xi_1 \tag{4-6}$$

The normalized probability distribution function is evaluated based on the sampled x, then its value compared with another random number ξ_2. If the second random number is less than the value of the probability distribution function at the given point x, then the point x is accepted. If not, it is rejected and a different possible x value is chosen using a third random number and tested by comparing the normalized probability distribution function with a fourth random number and so on.

Rejection sampling technique is applicable to all situations. Nevertheless, the efficiency of this technique, defined as the fraction of successful samplings, will be low when the density function is not close to uniformity.

4.4 Algorithm of Electron Analog Monte Carlo Simulation

In the analog Monte Carlo method, the electron track is simulated event by event. The general flow of the analog Monte Carlo simulation code is illustrated in Figure 4.1. The initial energy T_0 of the primary electron and its direction (θ_0, ϕ_0) are sampled. Accordingly, the probabilities of different kinds of interactions are calculated, that is

$$R_i(T) = \frac{\sum_{j=1}^{2} \sigma_i^j(T)}{\sigma_{Total}(T)} \tag{4-7}$$

$$R_{el}(T) = \frac{\sigma_{el}(T)}{\sigma_{Total}(T)} \tag{4-8}$$

$$R_{Ion}(T) = \frac{\sum_{j=1}^{5} \sigma_{Ion}^{j}(T)}{\sigma_{Total}(T)} \tag{4-9}$$

$$R_{exc}(T) = \frac{\sum_{j=1}^{18} \sigma_{exc}^{j}(T)}{\sigma_{Total}(T)} \tag{4-10}$$

$$R_{vex}(T) = \frac{\sum_{j=1}^{3} \sigma_{exc}^{v_j}(T)}{\sigma_{Total}(T)} \tag{4-11}$$

Where

$$\sigma_{Total}(T) = \sum_{j=1}^{2} \sigma_{i}^{j}(T) + \sigma_{el}(T) + \sum_{j=1}^{5} \sigma_{Ion}^{j}(T) + \sum_{j=1}^{18} \sigma_{exc}^{j}(T) + \sum_{j=1}^{3} \sigma_{exc}^{v_j}(T) \tag{4-12}$$

and

R_i; is the probability of having a dissociative attachment event

R_{el}; is the probability of having an elastic scattering.

R_{Ion}; is the probability of having an ionization collision.

R_{exc}; is the probability of having an electronic excitation collision.

R_{vex}; is the probability of having a vibrational excitation collision.

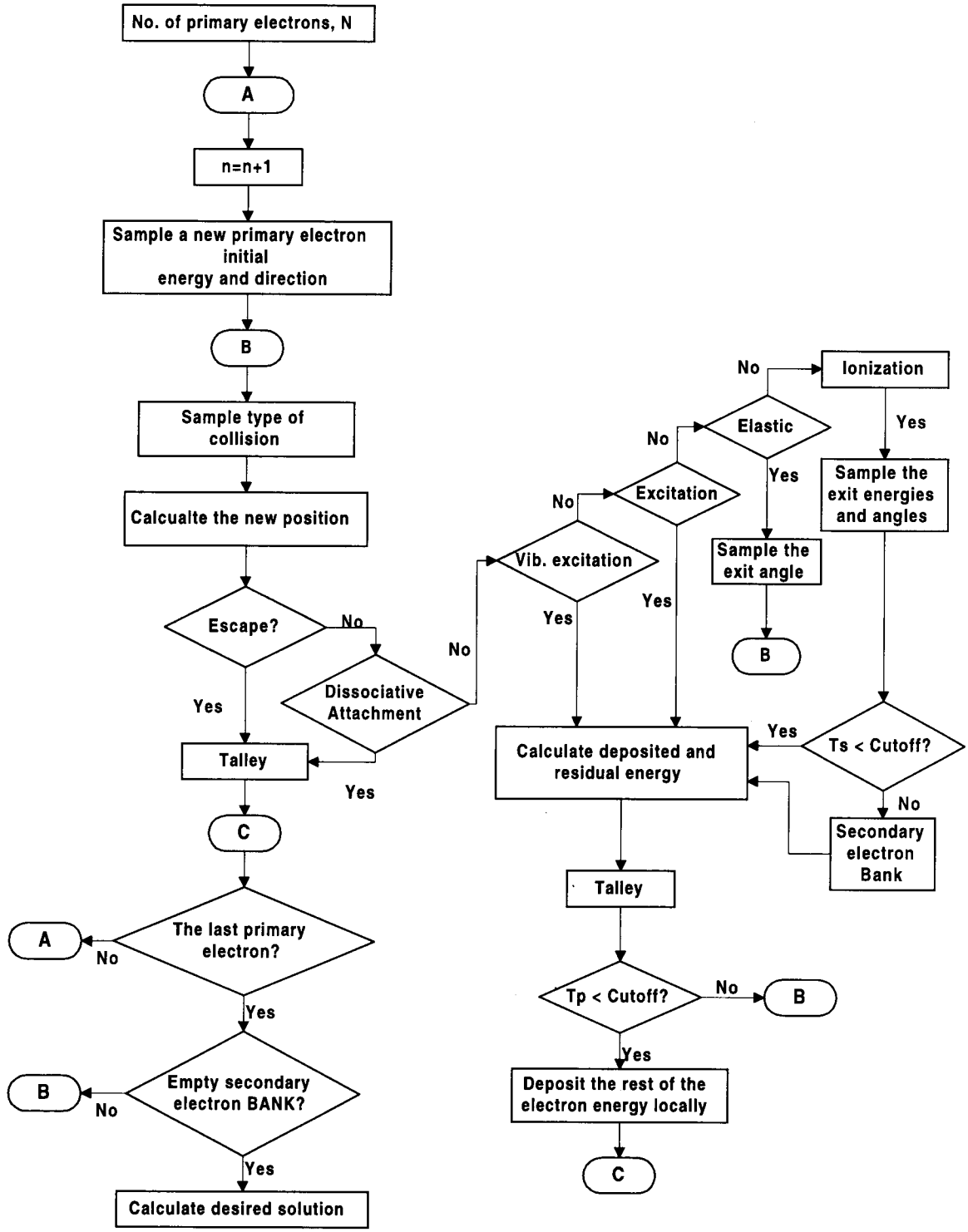

Figure 4.1 Flowchart for the Analog Monte Carlo Simulation .

Then, the type of interaction is chosen by comparing a uniformly distributed random number ξ in the interval [0-1] with the interaction probabilities, that is

$$0 \leq \xi < R_i$$

Dissiocaitive attachment event (4-13)

$$R_i \leq \xi < R_i + R_{el}$$

Elastic scattering event (4-14)

$$R_i + R_{el} \leq \xi < (R_i + R_{el}) + R_{Ion}$$

Ionization collision event (4-15)

$$(R_i + R_{el} + R_{ion}) \leq \xi < (R_i + R_{el} + R_{ion}) + R_{exc}$$

Electronic excitation collision event (4-16)

$$(R_i + R_{el} + R_{ion} + R_{exc}) \leq \xi < 1.0$$

Vibartional excitation collision event (4-17)

The dissociative attachment interaction is considered only when the electron energy is within 5 to 20 eV range because the reaction probability beyond this range is highly insignificant.

The position of the electron at each new collision site is determined with the aid of the mean free path and the pre-collision direction angles (θ_n, ϕ_n). This new position is checked if it is still within the volume of interest, i.e., for the purpose of this work, within the cell. If the position is beyond the volume of interest or in other words the electron escaped the cell, then the electron history will be terminated and another new electron history proceeds. In case the electron has not escaped, the next event proceeds.

There are three possible ways for electron history termination; the electron escapes, its energy falls below the cutoff energy 0.198 eV (the lowest vibrational excitation threshold), or the interaction is a dissociative attachment event.

4.4.1 Dissociative Attachment Events

If the collision is a dissociative attachment event, then further investigation of the type of the formed ion is conducted

$$0.0 \leq \xi < R_i^{H}(T) \qquad \text{H-Ion formation} \qquad (4\text{-}18)$$

$$R_i^{H}(T) \leq \xi < R_i^{H}(T) + R_i^{O}(T) \quad (=R_i) \qquad \text{O-Ion formation} \qquad (4\text{-}19)$$

where

$$R_i^{H}(T) = \frac{\sigma_i^{H}(T)}{\sigma_{Total}(T)} \qquad (4\text{-}20)$$

and

$$R_i^O(T) = \frac{\sigma_i^O(T)}{\sigma_{Total}(T)} \tag{4-21}$$

In the dissociative attachment event the electron disappears from the track at the interaction position as it attaches to the molecule, hence, its track is terminated. The electron energy before the dissociatve attachment interaction is considered to be totally deposited at the interaction position.

4.4.2 Elastic Scattering Events

If the collision is elastic, then the polar angle after collision θ_{n+1} is randomly sampled from the probability distribution function

$$F(T,\theta) = \frac{\int_0^{\theta} \left(\frac{d\sigma_{el}(T,\theta')}{d\theta'} \right) d\theta'}{\sigma_{el}(T)} \tag{4-22}$$

Figure 4.2 shows the probability distribution function of the elastic scattering polar angle θ for different electron energies. The azimuthal angle ϕ_{n+1} after the elastic collision is randomly sampled uniformly in the interval $(0, 2\pi)$.

4.4.3 Ionization Collision Events

If the collision cause ionization, then further investigation of the orbital which is involved in the event is required, that is

$$(R_i + R_{el}) \leq \xi < (R_i + R_{el}) + R^1_{Ion}$$

1b1-orbital (j=1) (4-23)

$$(R_i + R_{el}) + R^1_{Ion} \leq \xi < (R_i + R_{el}) + \sum_{j=1}^{2} R^j_{Ion}$$

3a1-orbital (j=2) (4-24)

$$(R_i + R_{el}) + \sum_{j=1}^{2} R^j_{Ion} \leq \xi < (R_i + R_{el}) + \sum_{j=1}^{3} R^j_{Ion}$$

1b2-orbital (j=3) (4-25)

$$(R_i + R_{el}) + \sum_{j=1}^{3} R^j_{Ion} \leq \xi < (R_i + R_{el}) + \sum_{j=1}^{4} R^j_{Ion}$$

2a1-orbital (j=4) (4-26)

$$(R_i + R_{el}) + \sum_{j=1}^{4} R^j_{Ion} \leq \xi < (R_i + R_{el}) + \sum_{j=1}^{5} R^j_{Ion}$$

1a1-orbital (j=5) (4-27)

Where

$$\sum_{j=1}^{n} R_{Ion}^{j}(T) = \frac{\sum_{j=1}^{n} \sigma_{Ion}^{j}(T)}{\sigma_{Total}(T)} \tag{4-28}$$

and n has the values from one to five.

The energy probability distribution function of the secondary electron is governed by the corresponding single differential ionization cross section normalized to unity

$$F_j(T,W) = \frac{\int_0^W \left(\frac{d\sigma_{Ion}^{j}(T,W')}{dW'} \right) dW'}{\sigma_{Ion}^{j}(T)} \tag{4-29}$$

The energy loss due to an ionization collision, i.e., the energy deposited at the ionization event position, is equal to the binding energy of the electron B_j. If the sampled energy of the secondary electron is below the cutoff energy, then the deposited energy is

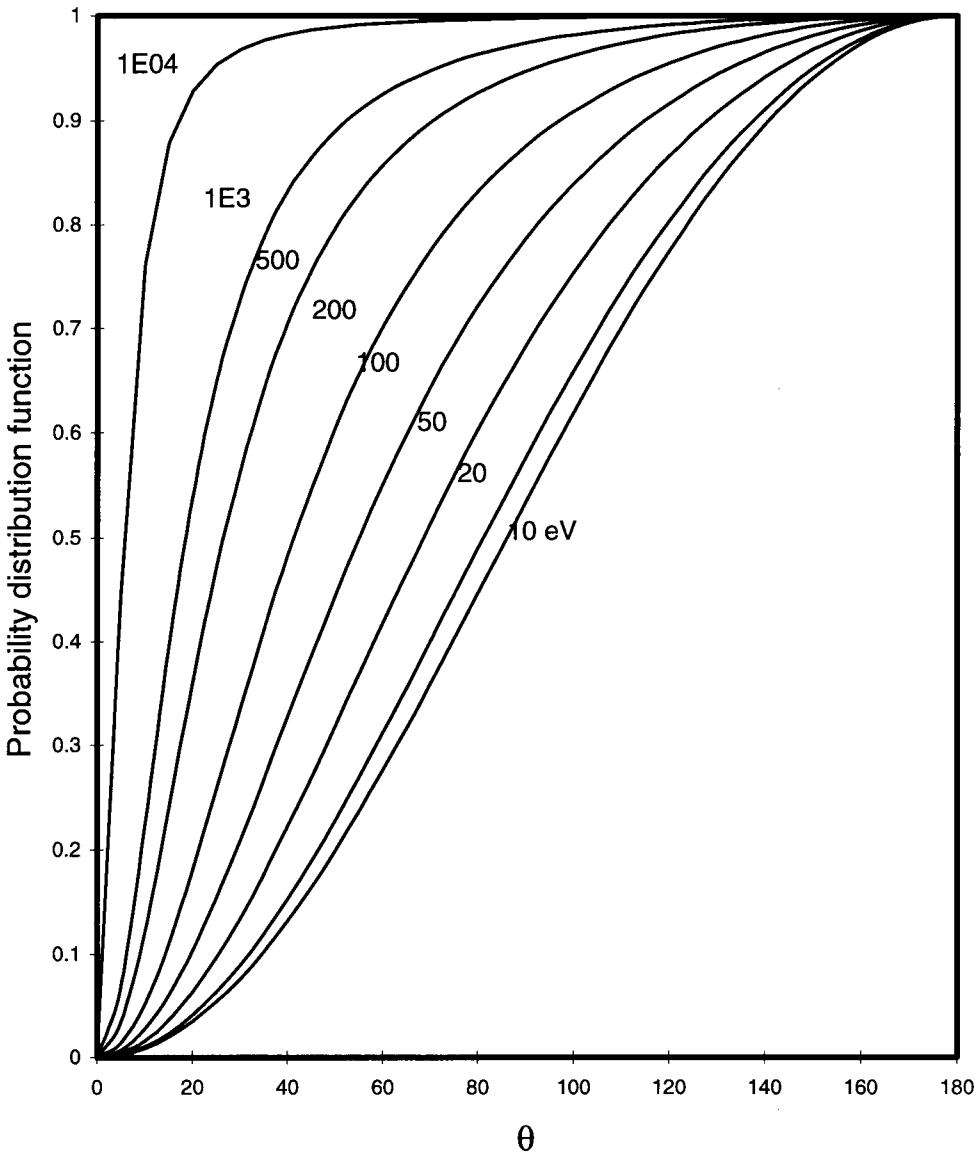

Figure 4.2 Probability distribution function $F(T,\theta)$ of the elastic scattering polar angle for different electron energies.

the summation of the binding energy and the secondary electron energy (i.e., $B_j + W$) and the secondary electron will not be banked for later simulation. On the other hand,the primary electron history will be terminated when the value of its energy after collision falls below the value of the cut off energy. Figures 4.3 to 4.7 present the probability distribution function $F_j(T,W)$ of the energy of the secondary electrons for five electron orbitals.

The polar angle of the primary electron θ_p after collision can be evaluated, for energies above 100 eV, as [72]

$$\sin^2(\theta_p) = \frac{\left(\frac{W}{T}\right)}{\left(1-\frac{W}{T}\right)\left(\frac{T}{2m_0c^2}\right)+1} \tag{4-30}$$

For lower energies, i.e., less than 100 eV, the additional assumption is made that the primary electron polar angles after collision are uniformly distributed between zero and $\pi/4$ [121].

The secondary electron polar angles θ_s , for secondary electron energies higher than 200 eV, can be calculated as [120]

$$\sin^2(\theta_s) = \frac{1-\left(\frac{W}{T}\right)}{\left(1+\frac{W}{T}\right)} \tag{4-31}$$

For secondary electrons of lower energy, i.e., less than 200 eV, the treatment suggested by Grosswendt and Waibel, based on measurement, was followed [123]. Despite the value of the primary electron energy, the secondary electron with energies less than 50 eV are scattered isotropically. In the energy range of secondary electrons between 50 eV and 200 eV there is 90% chance that the secondary electrons scatter uniformly in the angles range $\pi/4$ to $\pi/2$ and for the rest 10% chance the scattering is isotropic.

The azimuthal angle of the primary electron after collision Φ_p is taken to be isotropic, and the azimuthal angle of the secondary electron Φ_s is set equal to $\Phi_p - \pi$.

The errors in the above angular distribution treatment after ionization impact are not significant because the spatial distribution of the energy deposition is more affected by elastic scattering interactions.

4.4.4 Electronic Excitation Events

Once the interaction has been sampled to be electronic excitation event, further investigation has to be carried out to specify the mode of excitation among the eighteen pre-specified modes

$$(R_i + R_{el} + R_{lon}) \leq \xi < (R_i + R_{el} + R_{ion}) + R^I_{exc}$$

Rydberg (A+B), n=3 (4-32)

$$(R_i + R_{el} + R^1_{Ion}) + R^1_{exc} \leq \xi < (R_i + R_{el} + R_{ion}) + \sum_{j=1}^{2} R^j_{exc}$$

Rydberg (A+B), n≥4 (4-33)

$$(R_i + R_{el} + R_{Ion}) + \sum_{j=1}^{2} R^j_{exc} \leq \xi < (R_i + R_{el} + R_{Ion}) + \sum_{j=1}^{3} R^j_{exc}$$

Rydberg (C+D), n=3 (4-34)

$$(R_i + R_{el} + R_{Ion}) + \sum_{j=1}^{3} R^j_{exc} \leq \xi < (R_i + R_{el} + R_{Ion}) + \sum_{j=1}^{4} R^j_{exc}$$

Rydberg (C+D), n≥4 (4-35)

$$(R_i + R_{el} + R_{Ion}) + \sum_{j=1}^{4} R^j_{exc} \leq \xi < (R_i + R_{el} + R_{Ion}) + \sum_{j=1}^{5} R^j_{exc}$$

Diffuse Bands (4-36)

$$(R_i + R_{el} + R_{Ion}) + \sum_{j=1}^{5} R^j_{exc} \leq \xi < (R_i + R_{el} + R_{Ion}) + \sum_{j=1}^{6} R^j_{exc}$$

Dissociative continuum 1 (4-37)

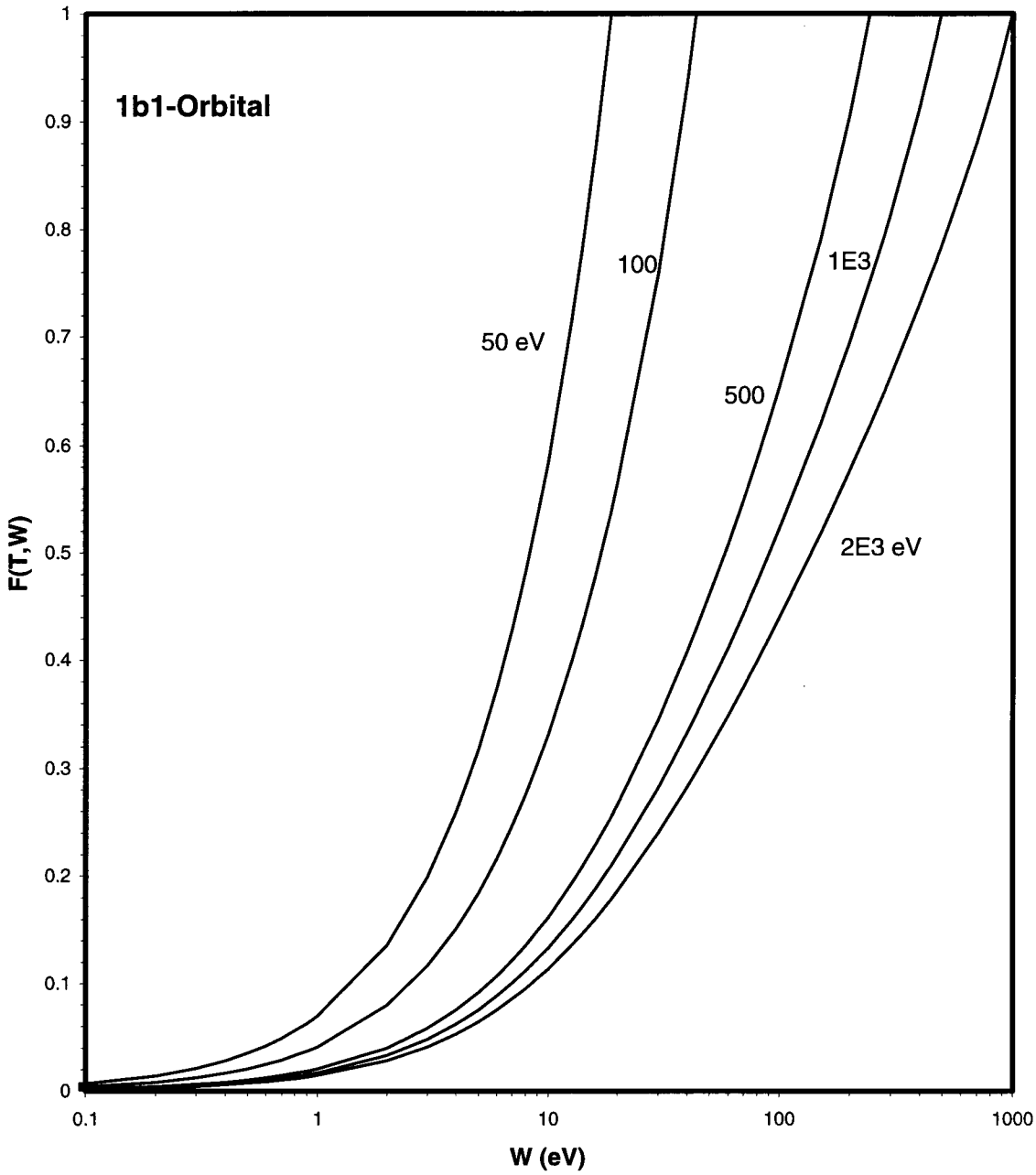

Figure 4.3 Probability distribution function $F_j(T,W)$ of the secondary electron energy for 1b1-Orbital, different curves for different primary electron energies.

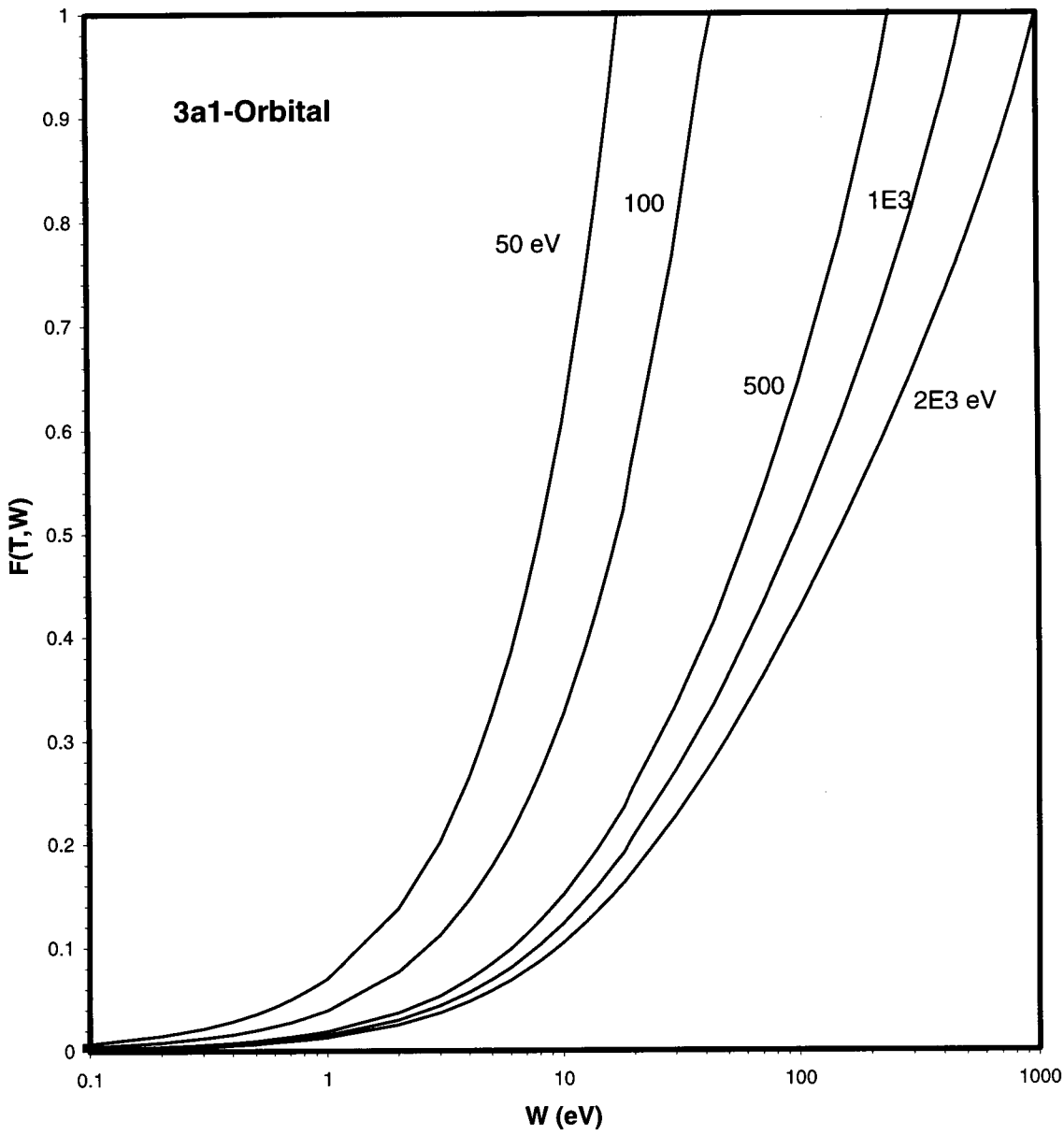

Figure 4.4 Probability distribution function $F_j(T,W)$ of the secondary electron energy for 3a1-Orbital, different curves for different primary electron energies.

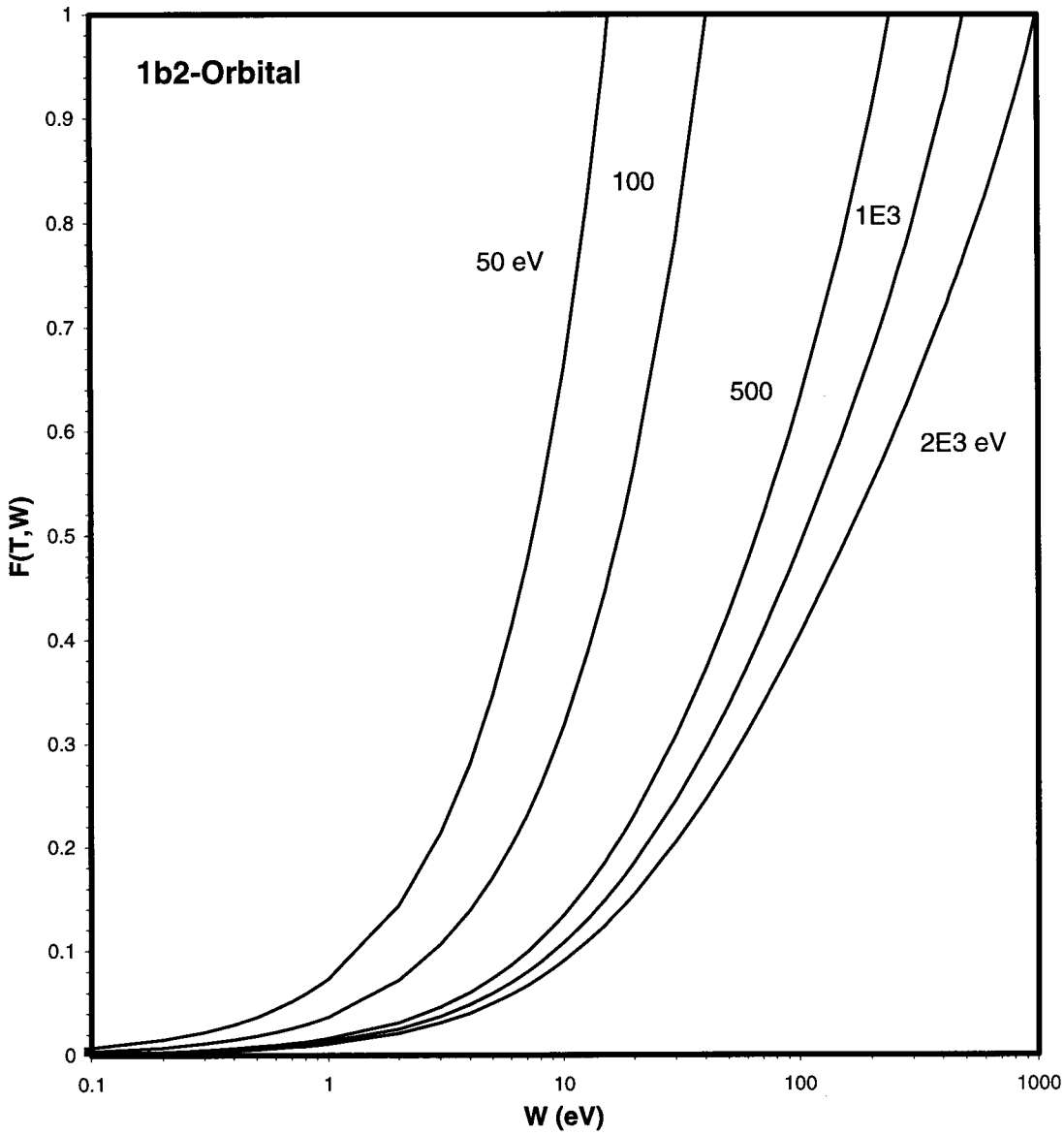

Figure 4.5 Probability distribution function $F_j(T,W)$ of the secondary electron energy for 1b2-Orbital, different curves for different primary electron energies.

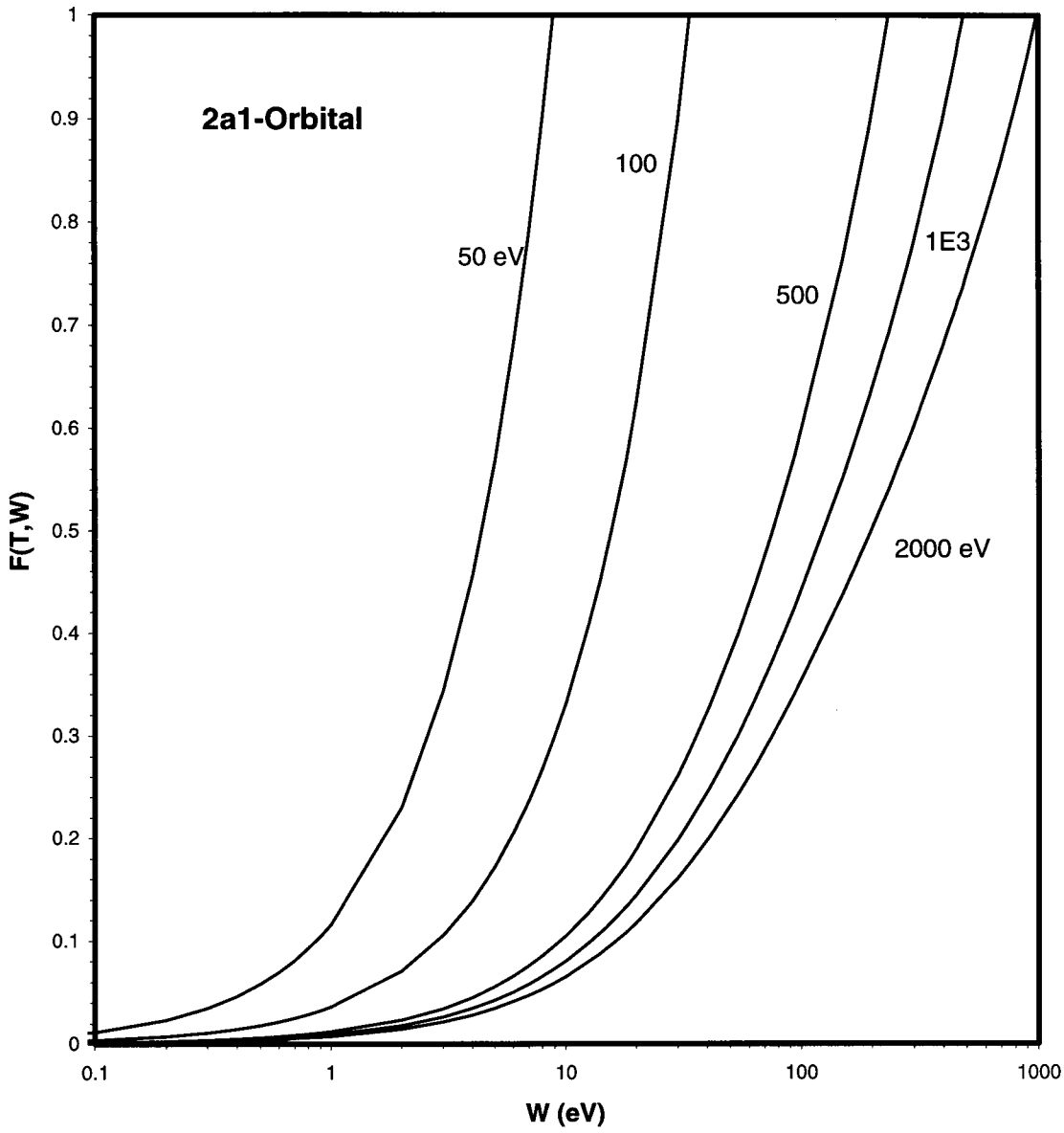

Figure 4.6 Probability distribution function $F_j(T,W)$ of the secondary electron energy for 2a1-Orbita, different curves for different primary electron energies.

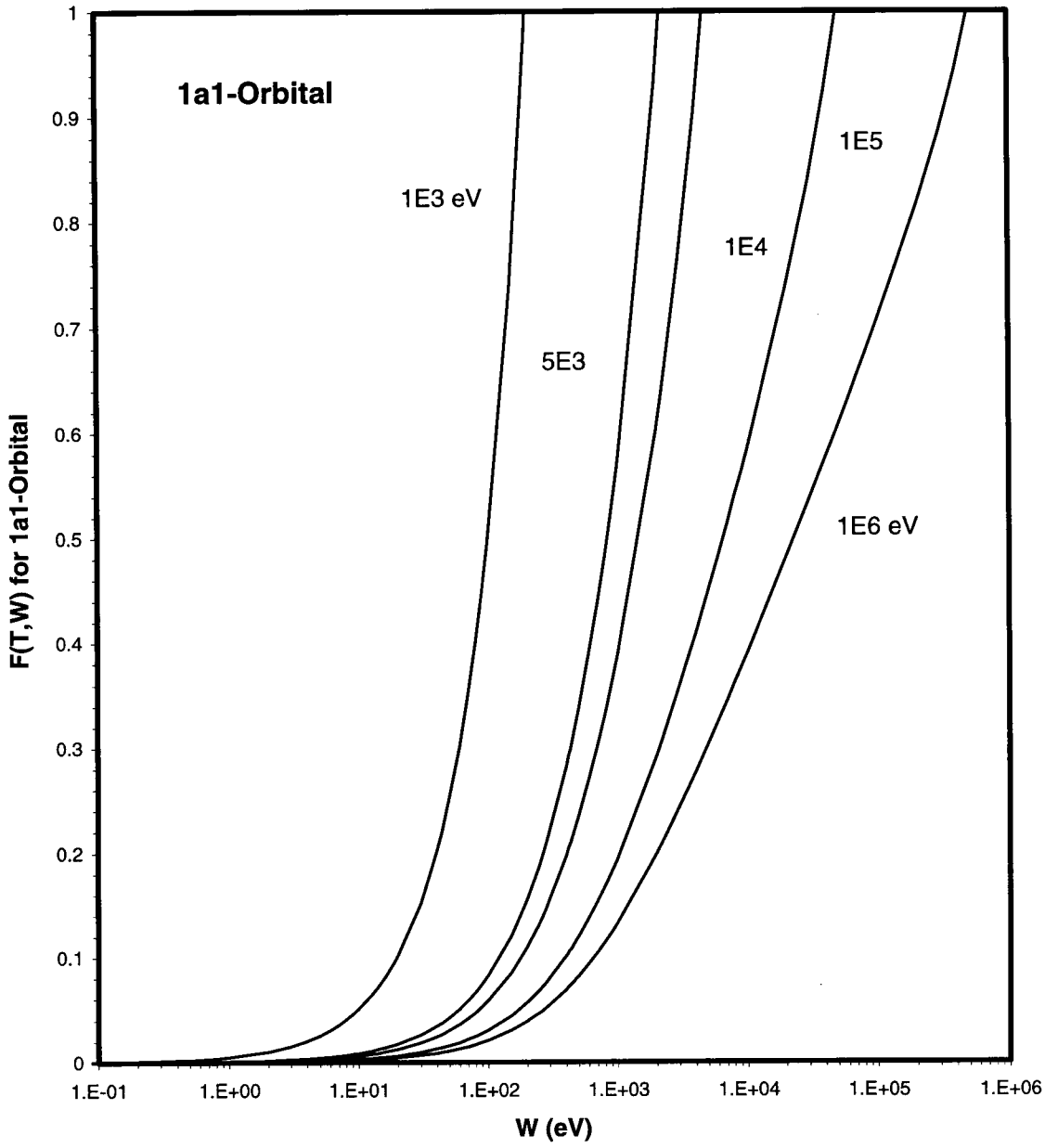

Figure 4.7 Probability distribution function $F_j(T,W)$ for the secondary electron energy for 1a1-Orbital.

$$(R_i + R_{el} + R_{Ion}) + \sum_{j=1}^{6} R_{exc}^{j} \leq \xi < (R_i + R_{el} + R_{Ion}) + \sum_{j=1}^{7} R_{exc}^{j}$$

Dissociative continuum 2 (4-38)

$$(R_i + R_{el} + R_{Ion}) + \sum_{j=1}^{7} R_{exc}^{j} \leq \xi < (R_i + R_{el} + R_{Ion}) + \sum_{j=1}^{8} R_{exc}^{j}$$

Triplet-1 (4-39)

$$(R_i + R_{el} + R_{Ion}) + \sum_{j=1}^{8} R_{exc}^{j} \leq \xi < (R_i + R_{el} + R_{Ion}) + \sum_{j=1}^{9} R_{exc}^{j}$$

Triplet-2 (4-40)

$$(R_i + R_{el} + R_{Ion}) + \sum_{j=1}^{9} R_{exc}^{j} \leq \xi < (R_i + R_{el} + R_{Ion}) + \sum_{j=1}^{10} R_{exc}^{j}$$

Lyman α (4-41)

$$(R_i + R_{el} + R_{Ion}) + \sum_{j=1}^{10} R_{exc}^{j} \leq \xi < (R_i + R_{el} + R_{Ion}) + \sum_{j=1}^{11} R_{exc}^{j}$$

Balmer α (4-42)

$$(R_i + R_{el} + R_{Ion}) + \sum_{j=1}^{11} R_{exc}^{j} \leq \xi < (R_i + R_{el} + R_{Ion}) + \sum_{j=1}^{12} R_{exc}^{j}$$

Balmer β (4-43)

$$(R_i + R_{el} + R_{Ion}) + \sum_{j=1}^{12} R_{exc}^{j} \leq \xi < (R_i + R_{el} + R_{Ion}) + \sum_{j=1}^{13} R_{exc}^{j}$$

Balmer γ (4-44)

$$(R_i + R_{el} + R_{Ion}) + \sum_{j=1}^{13} R_{exc}^{j} \leq \xi < (R_i + R_{el} + R_{Ion}) + \sum_{j=1}^{14} R_{exc}^{j}$$

Balmer δ (4-45)

$$(R_i + R_{el} + R_{Ion}) + \sum_{j=1}^{14} R_{exc}^{j} \leq \xi < (R_i + R_{el} + R_{Ion}) + \sum_{j=1}^{15} R_{exc}^{j}$$

OI 8447 (4-46)

$$(R_i + R_{el} + R_{Ion}) + \sum_{j=1}^{15} R_{exc}^{j} \leq \xi < (R_i + R_{el} + R_{Ion}) + \sum_{j=1}^{16} R_{exc}^{j}$$

OI 7774 (4-47)

$$(R_i + R_{el} + R_{Ion}) + \sum_{j=1}^{16} R_{exc}^{j} \leq \xi < (R_i + R_{el} + R_{Ion}) + \sum_{j=1}^{17} R_{exc}^{j}$$

OH 3064 (4-48)

$$(R_i + R_{el} + R_{Ion}) + \sum_{j=1}^{17} R_{exc}^{j} \leq \xi < (R_i + R_{el}\, R_{Ion}) + \sum_{j=1}^{18} R_{exc}^{j}$$

OH 2800 (4-49)

Where

$$\sum_{j=1}^{n} R_{exc}^{j}(T) = \frac{\sum_{j=1}^{n} \sigma_{exc}^{j}(T)}{\sigma_{Total}(T)} \tag{4-50}$$

and n has the values from one to eighteen.

Photons emitted after electronic excitation impact are assumed to be absorbed at their point of origin. The experimental measurements of Trajmar et al. [122] show that the angular distribution of electrons after exciting molecular levels is strongly peaked forward. Furthermore, because the spatial distribution of electrons is dominated by elastic scattering, it is justified to assume that no change in the direction of flight of the incident electron takes place during excitation. The energy deposition at the electronic excitation position is equivalent to the threshold energy of the particular excitation mode.

4.4.5 Vibrationl Excitation Events

In this work, the vibrational excitation of water molecules is divided into three groups or states. Each state has a pre-specified energy threshold and interaction cross section. Decision on the state of vibrational excitation is made randomly

$$(R_i + R_{el} + R_{ion} + R_{exc}) \leq \xi < (R_i + R_{el} + R_{ion} + R_{exc}) + R^1_{vex}$$

state ν_{13} (4-51)

$$(R_i + R_{el} + R_{ion} + R_{exc}) + R^1_{vex} \leq \xi < (R_i + R_{el} + R_{ion} + R_{exc}) + \sum_{j=1}^{2} R^j_{vex}$$

state ν_2 (4-52)

$$(R_i + R_{el} + R_{ion} + R_{exc}) + \sum_{j=1}^{2} R^j_{vex} \leq \xi < (R_i + R_{el} + R_{ion} + R_{exc}) + \sum_{j=1}^{3} R^j_{vex}$$

state ν_r (4-53)

where

$$\sum_{j=1}^{n} R_{vex}^{j}(T) = \frac{\sum_{j=1}^{n} \sigma_{vex}^{j}(T)}{\sigma_{Total}(T)} \tag{4-54}$$

n has the values from one to three.

It is assumed that the electron does not change its direction after a vibrational excitation event.

4.5 Energy Spectrum of Beta-Particle

In β-decay, the kinetic energy of the daughter nucleus is a negligible fraction of the total mass defect caused by the β-decay. Therefore, the energy equivalent to total mass defect is shared by an electron and a neutrino. The emitted electron is decelerated by positive nuclear Coulomb force near the nucleus. Therefore, the β energy spectrum is shifted to a lower-energy range than the initial spectrum of electron energy. The electrostatic potential of atomic electrons also affects the energy spectrum. It, further, reduces the energy of the emitted electron (i.e., β-particle). However, the screening by atomic electrons is considered to cause a little change in the β-spectrum.

Fermi's theory of nuclear decay has been extensively reviewed by Evans [123]. In Fermi's theory, the energy distribution of electrons emitted in β-decay is evaluated considering three factors:

1. The statistical factor, for allowed transitions.
2. The nuclear Coulomb factor.

3. The screening by atomic electrons.

In the present work, the approximation given by Evans [123] is used. The normalized energy distribution function can be written as [124,125]

$$N(T) = \frac{f_0(T)\, f_1(T)\, f_c(Z,T)}{\int_0^{T_{max}} f_0(T)\, f_1(T)\, f_c(Z,T)\, dT} \tag{4-55}$$

where

$f_0(T)$ is the statistical factor

$f_1(T)$ is the correction factor for first-forbidden unique transition

$f_c(T,Z)$ is the correction factor for Coulomb interaction

T_{max} is the endpoint energy of the spectrum

Z is the atomic number of the daughter nucleus

The statistical factor, f_0 , for an allowed transition is given by

$$f_0(T) = \eta W (W_{max} - W)^2 \tag{4-56}$$

W is the total energy in the electron rest mass unit, i.e.,

$$W = \frac{T}{m_0 c^2} + 1 + V_0 \tag{4-57}$$

V_0 is the screening potential due to atomic electrons in electron rest mass unit

$$V_0 = \frac{1.13|Z|^{4/3}}{\alpha^2} \tag{4-58}$$

α is the fine structure constant and η is the electron momentum in $m_0 c$

$$\eta = \frac{p}{m_0 c} \tag{4-59}$$

$$p = \frac{\sqrt{E^2 - m_0^2 c^4}}{c} \tag{4-60}$$

$$E = T + m_0 c^2 - V_0 \, m_0 c^2 \tag{4-61}$$

so that

$$\eta = \sqrt{W^2 - 1} \tag{4-62}$$

The correction factor for a first-forbidden unique transition is

$$f_1(T) = \eta^2 + (W_{\max} - W)^2 \tag{4-63}$$

$f_1(T)$ is taken to be one for allowed transition or forbidden transitions other than first-forbidden unique.

The relativistic Coulomb correction factor can be written as

$$f_c(T,Z)=\eta^{2(\gamma-1)}\, e^{\pi y}\left|\Gamma(\gamma+iy)\right|^2 \tag{4-64}$$

where

$$\gamma=\sqrt{1-(\alpha Z)^2} \tag{4-65}$$

$$y=\frac{\alpha Z W}{\eta} \tag{4-66}$$

and Γ is the complex Gamma-function. It can be evaluated numerically by following the numerical algorithm described by Kuki [126].

The beta spectrum of ^{90}Y (T_{max} = 2.27 MeV and $t_{1/2}$ = 2.67 days) is shown in Figure 4.8. The beta-energy span was divided into 42 energy bins, as listed in table 4.1. Histogram of the beta energy spectrum based on these bins is shown in Figure 4.9.

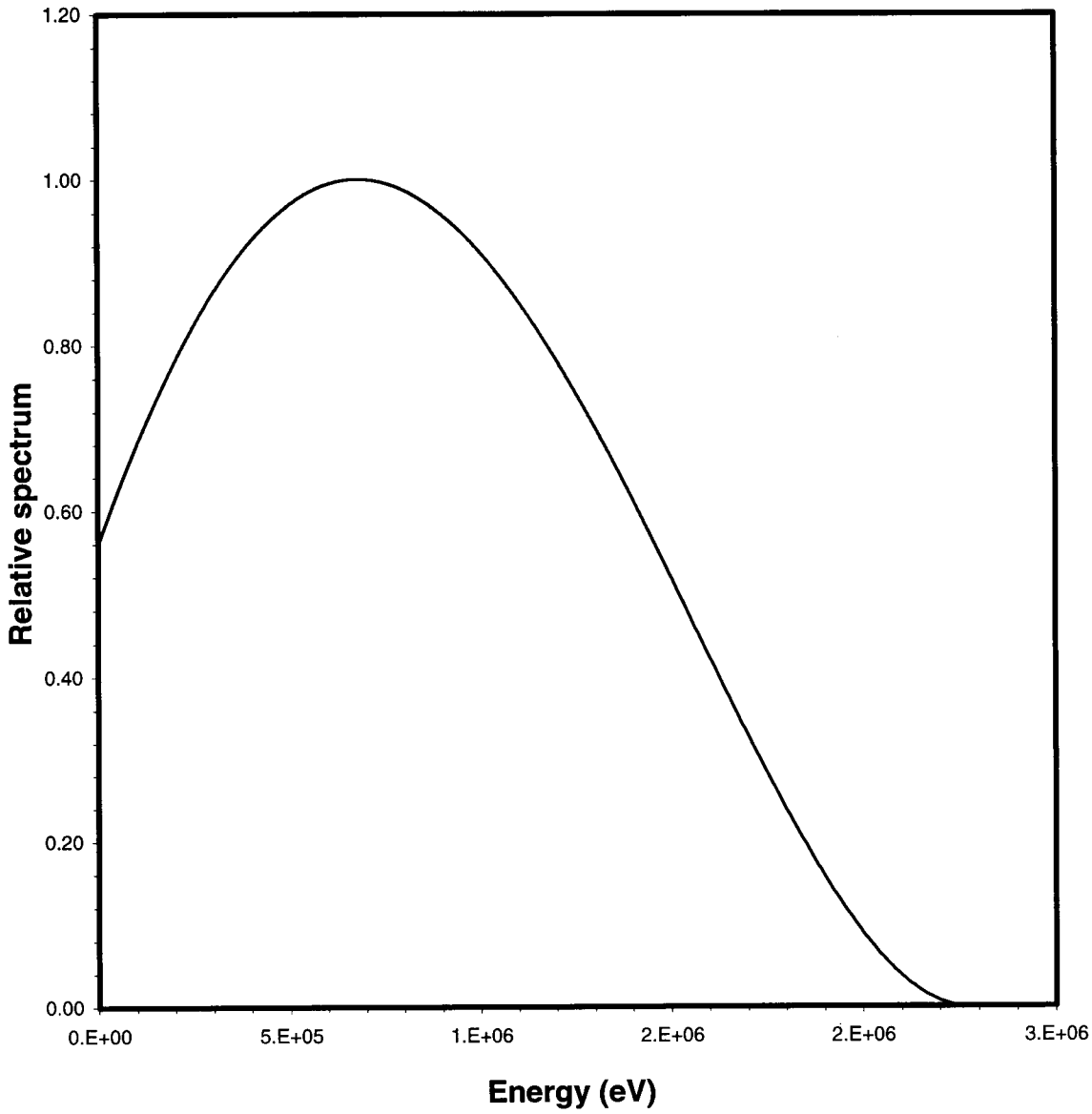

Figure 4.8 Relative beta spectrum of ^{90}Y.

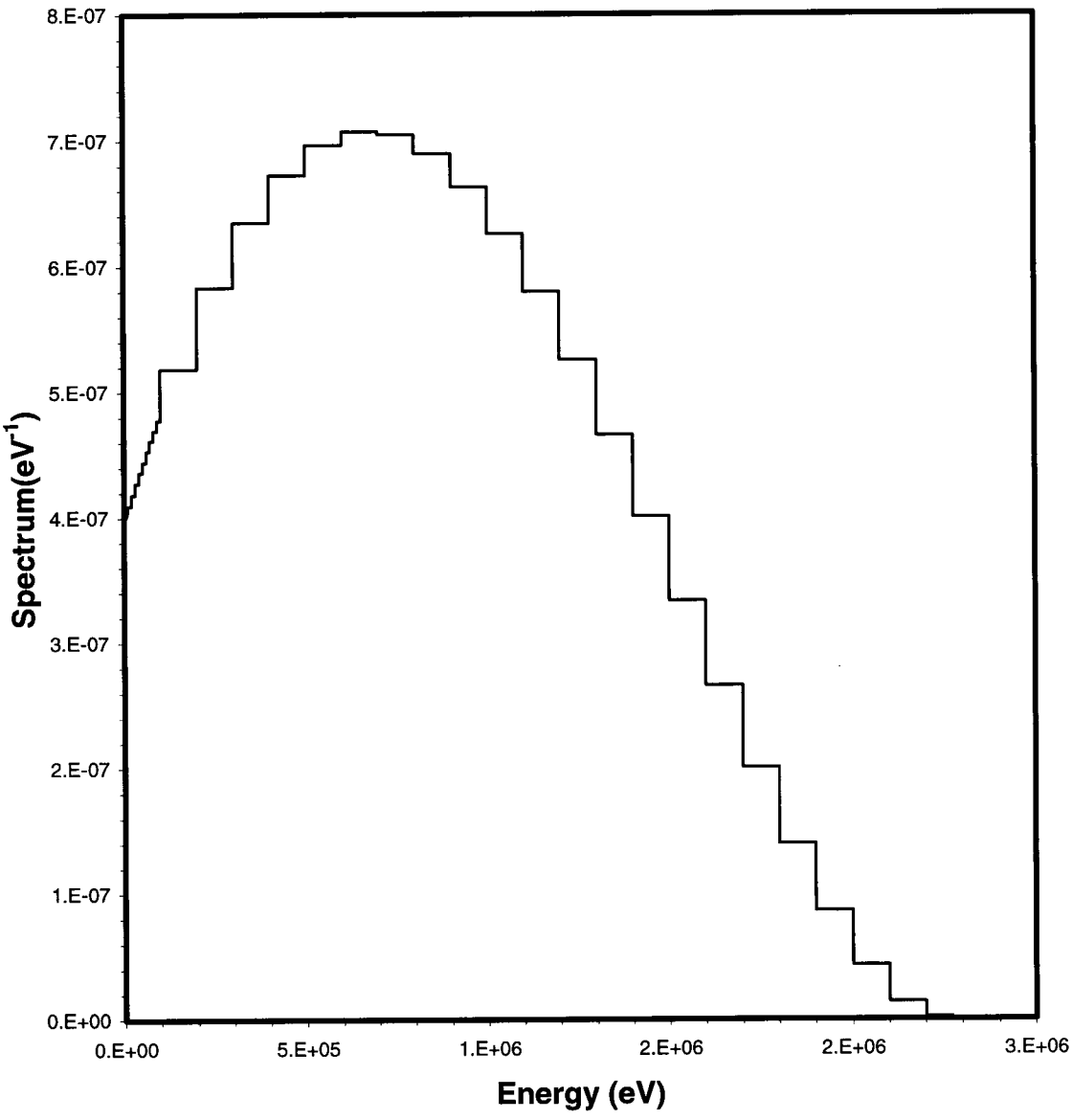

Figure 4.9 Histogram of the beta spectrum of ^{90}Y.

Energy bin No.	Energy
1	0.00E00
2	1.00E03
3	2.00E03
4	3.00E03
5	4.00E03
6	5.00E03
7	6.00E03
8	7.00E03
9	8.00E03
10	9.00E03
11	1.00E04
12	2.00E04
13	3.00E04
14	4.00E04
15	5.00E04
16	6.00E04
17	7.00E04
18	8.00E04
19	9.00E04
20	1.00E05
21	2.00E05
22	3.00E05
23	4.00E05
24	5.00E05
25	6.00E05
26	7.00E05
27	8.00E05
28	9.00E05
29	1.00E06
30	1.10E06
31	1.20E06
32	1.30E06
33	1.40E06
34	1.50E06
35	1.60E06
36	1.70E06
37	1.80E06
38	1.90E06
39	2.00E06
40	2.10E06
41	2.20E06
42	2.27E06

Table 4.1 Energy bins used for Beta histogram evaluation.

5. RESULTS

5.1 ^{90}Y Beta Dose Point Kernel

Calculation of the beta dose distribution from the activity distribution is straight forward if the medium is homogeneous with regard to electron transport properties. In the homogeneous situation, the principle of linearity ensures that once the dose distribution from a unit point source is established, then the dose may be calculated for any activity distribution. The dose response, as a function of the radial distance , r, to a point source of beta emitting radionuclide is termed beta dose point kernel $k(r)$.

In this work, MCNP-4B has been used to calculate dose distribution from a point-source of ^{90}Y. The point-source is isotropic and surrounded by water. Due to energy loss fluctuations during transport, electrons show range straggling. However, the nominal Continuous Slowing Down Approximation range R_{CSDA} , defined as a function of electron energy, provides a useful index for the maximum path length. The value of the R_{CSDA} can be calculated as follows

$$R_{CSDA}(T_0) = \int_0^{T_0} \left(\frac{dT}{dx}\right)^{-1} dT \qquad (5\text{-}1)$$

where T_o is the end point of the beta spectrum

and $\frac{dT}{dx}$ is the electron stopping power.

In the case of beta spectrum, the maximum beta particle range is that of the end point energy of the spectrum, i.e., $T_o = T_{max}$ in equation (5-1)

In order to consider the energy loss fluctuation, the maximum path length of an electron is taken to be 1.2 R_{CSDA} [39]. Therefore, an electron of energy equal to or less than the end point energy of the beta spectrum of ^{90}Y has a negligible probability to deliver an impact on a target unless the target is located within a distance equal to 1.2 $R_{CSDA}(T_{max}) = 1.35$ cm .

The calculation of beta dose point kernels was performed for a point source located at the center of 1.35 cm radius water sphere. This saves time needed to follow electrons beyond the maximum path length because they are insignificant in delivering energy to the target. This strategy allows an improvement in the counting by tracking additional initial electrons. The water sphere was divided into 100 spherical shells. The value of minimum cut-off energy used in MCNP-4B is 1 keV; however, another calculation with a cut-off value of 2 keV was performed as well for comparison purpose with other published data. The energy deposited in each shell was divided by the shell mass which is then taken to be the dose at the mean radius of the shell. Figure 5.1 compares the dose distribution from a point source of ^{90}Y in a water medium as calculated by Simpkin and Mackie using the EGS4 code [34], by Cross et al. using the ACCEPT code [35], by Berger using the ETRAN code [cited in 35], by Prestwich et al. [39] and the results of Spencer who numerically solved the transport equation in CSDA taking into account multiple scattering [25]. The results of the Monte Carlo codes (EGS4,

ACCEPT and ETRAN) were derived by averaging dose values for monoenergetic electrons over the beta spectrum

$$D(r) = Y \int_0^{T_{max}} N(T)\ D(r,T)\ dT \qquad (5\text{-}2)$$

Where Y is the number of beta particles per disintegration and $N(T)$ is the beta spectrum (beta particles per eV). In order to avoid dose singularity at the origin the dose values were multiplied by r^2. An analytical representation of the MCNP-4B results of the point kernels was obtained by least square fitting

$$D(r) = \frac{\exp^{\sum_{i=0}^{4} \alpha_i r^i}}{r^2} \qquad (5\text{-}2)$$

Where r is in centimeters, $D(r)$ is in nGy Bq^{-1} hr^{-1} and α's are the equation parameters. These have the following values for the given results:

$\alpha_0 = 4.536318$
$\alpha_1 = 1.172486$
$\alpha_2 = -11.8628$
$\alpha_3 = 16.9837$
$\alpha_4 = -14.5089$

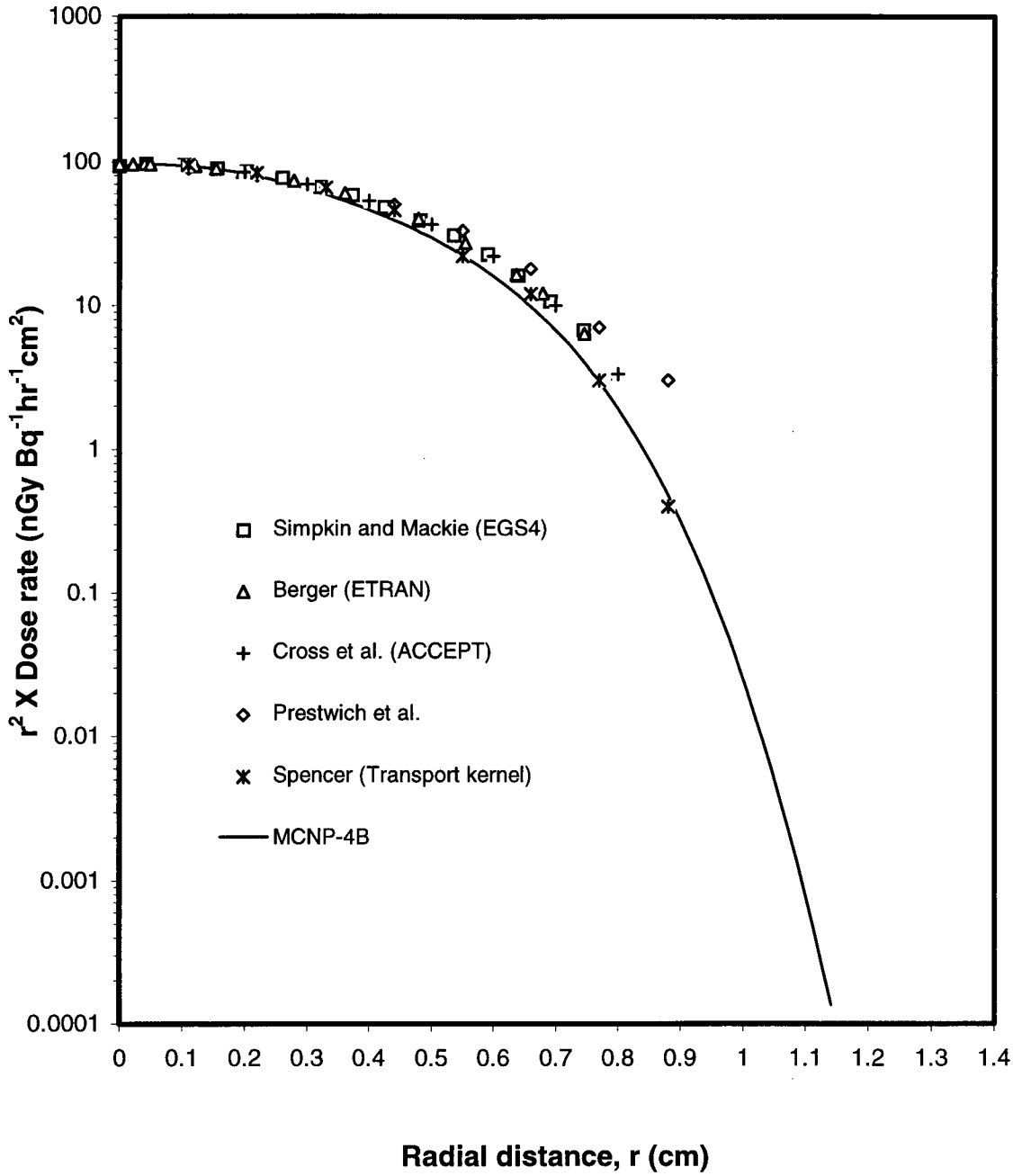

Figure 5.1 Comparison between the beta dose distributions for ^{90}Y, calculated by Simpkin and Mackie using the EGS4 [34], Berger using the ETRAN [cited in 35], Cross et al. using the ACCEPT [35], Prestwich et al [39], Spencer [25], andMCNP-4B.

The electron energy-spectra at different radial distances from a ^{90}Y point source were calculated and are shown in Figures 5.2 to 5.5. The shape of the spectrum becomes harder as the radial distance increases; also the values of the probable energy, average energy and end-point energy decrease, Figure 5.6.

5.2 Cold-region Effect

The effect of cold-regions, i.e., regions with no or low monoclonal antibody concentration, has been investigated by assuming the ideal situation of uniform distribution of monoclonal antibodies within the tumor mass. The cold region was assumed to have a spherical shape and is located at a distance at least one maximum range (R_{max}) from the tumor boundary as seen in Figure 5.7. It is further assumed that there is zero ^{90}Y activity within the region.

The absorbed dose profile as fraction of the equilibrium dose (i.e., the absorbed dose in the hot-region at distances greater than or equal to the maximum beta range of ^{90}Y from the tumor outer edge) across the cold-region was calculated for different cold-region radii: 0.354 cm (0.263 R_{max}), 0.27 cm (0.2 R_{max}), 0.237 cm (0.175R_{max}) and 0.202 cm (0.15R_{max}) as seen in Figure 5.8.

The radiation dose to successive shells of the tumor cold-region at increasing distances, x (with $x_{max} = R_{CR}$), from the hot-cold regions boundary as seen in Figure 5.7, decreases rapidly. In relatively large cold-regions (cold-regions with radii comparable to the maximum electron range), a region of tumor appears which does not receive any radiation dose at distances for which x comparable to R_{max}. The MCNP-4B results show

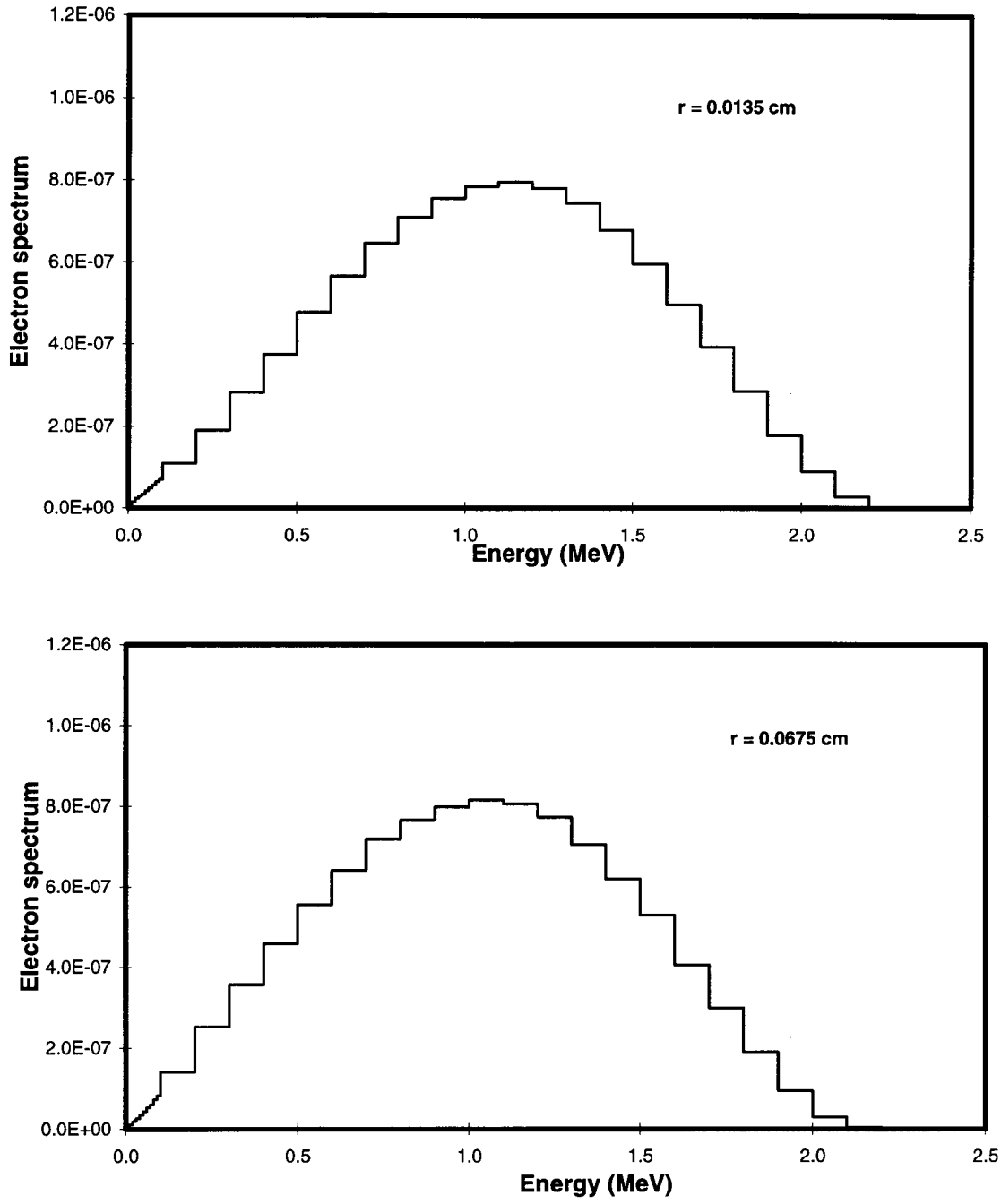

Figure 5.2 Electron energy-spectra at r = 0.0135 and r = 0.0675 centimeters.

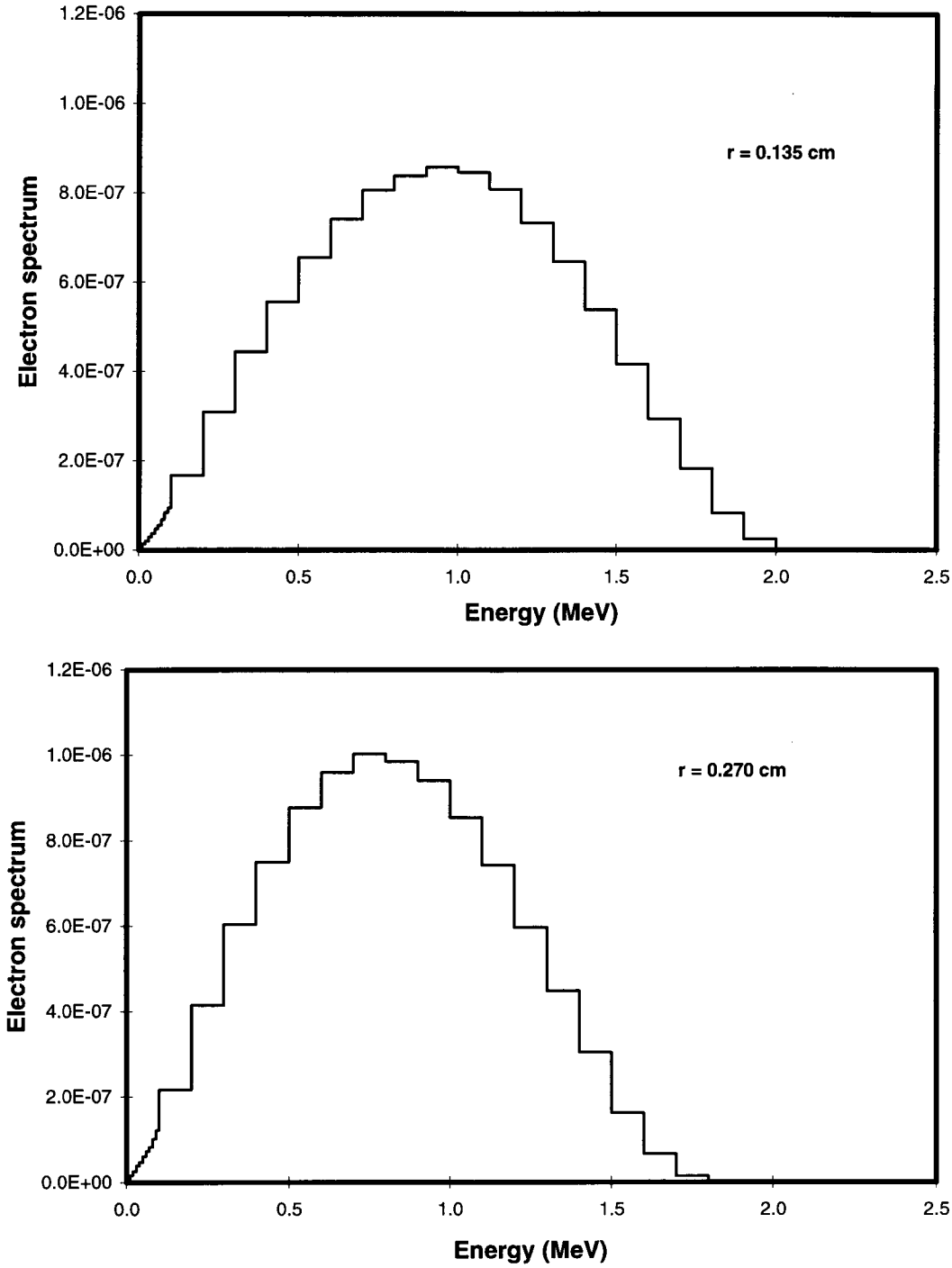

Figure 5.3 Electron energy-spectra at r = 0.135 and r = 0.270 centimeters.

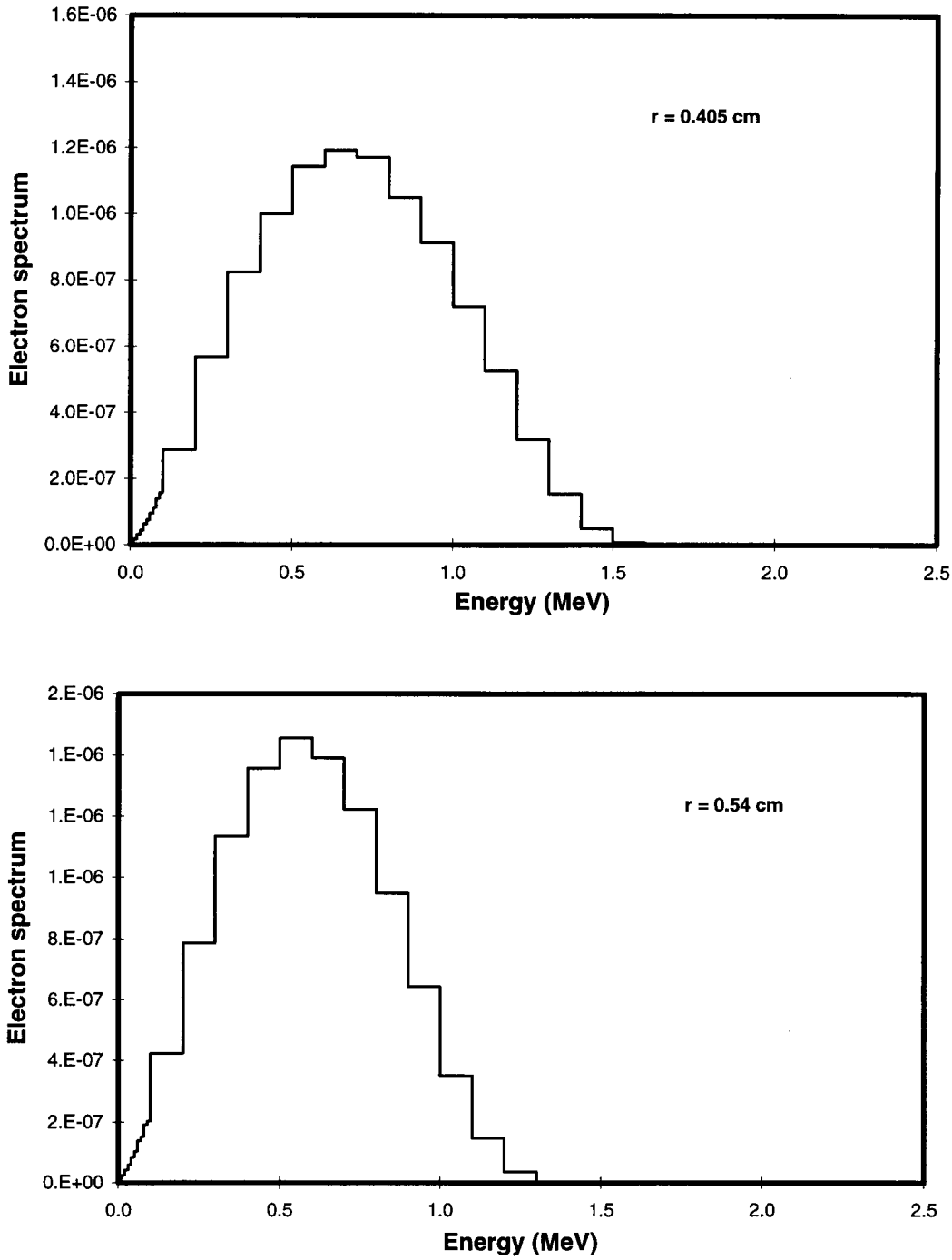

Figure 5.4 Electron energy-spectra at r = 0.405 and r = 0.540 centimeters.

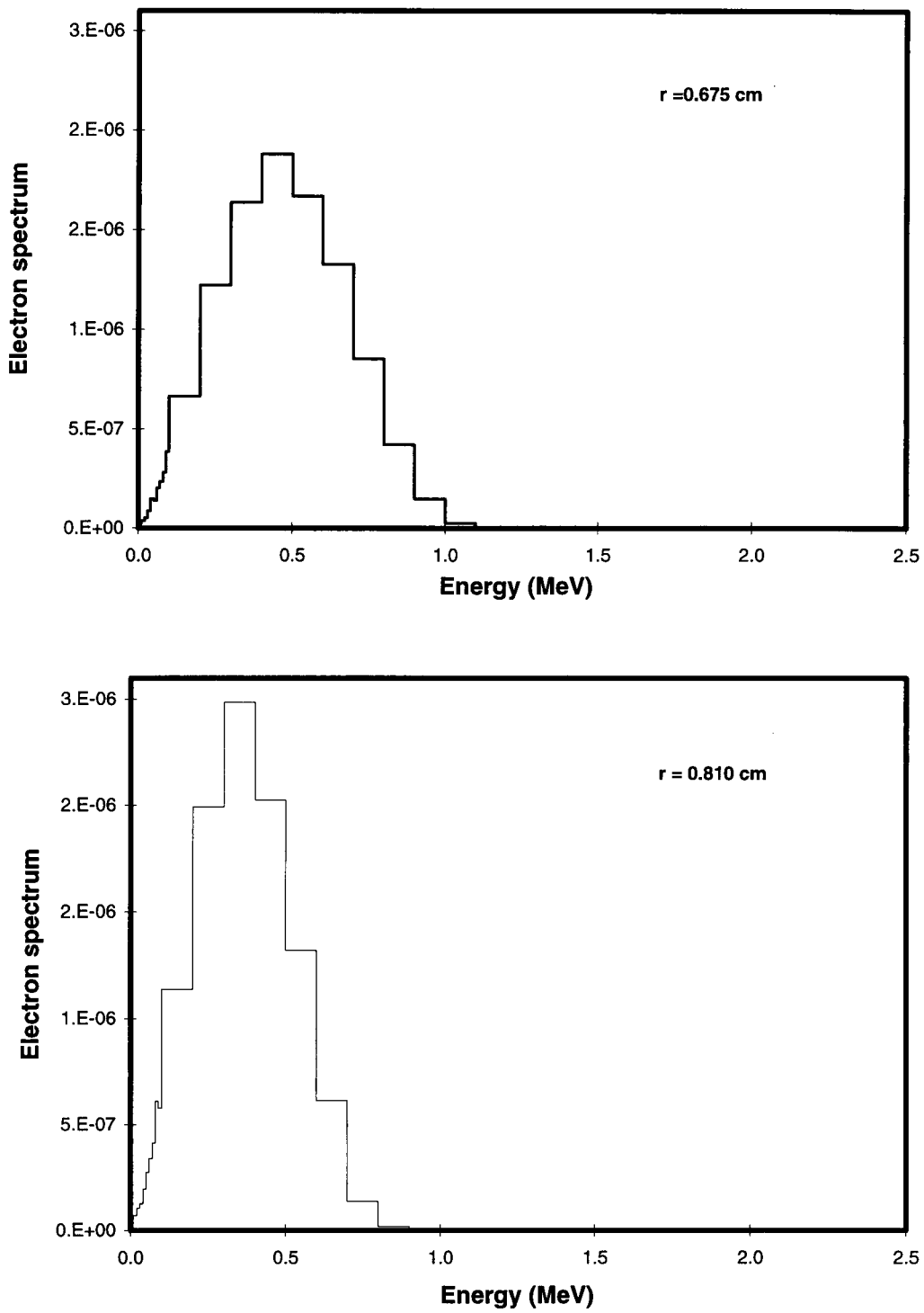

Figure 5.5 Electron energy-spectra at r = 0.675 and r = 0.810 centimeters.

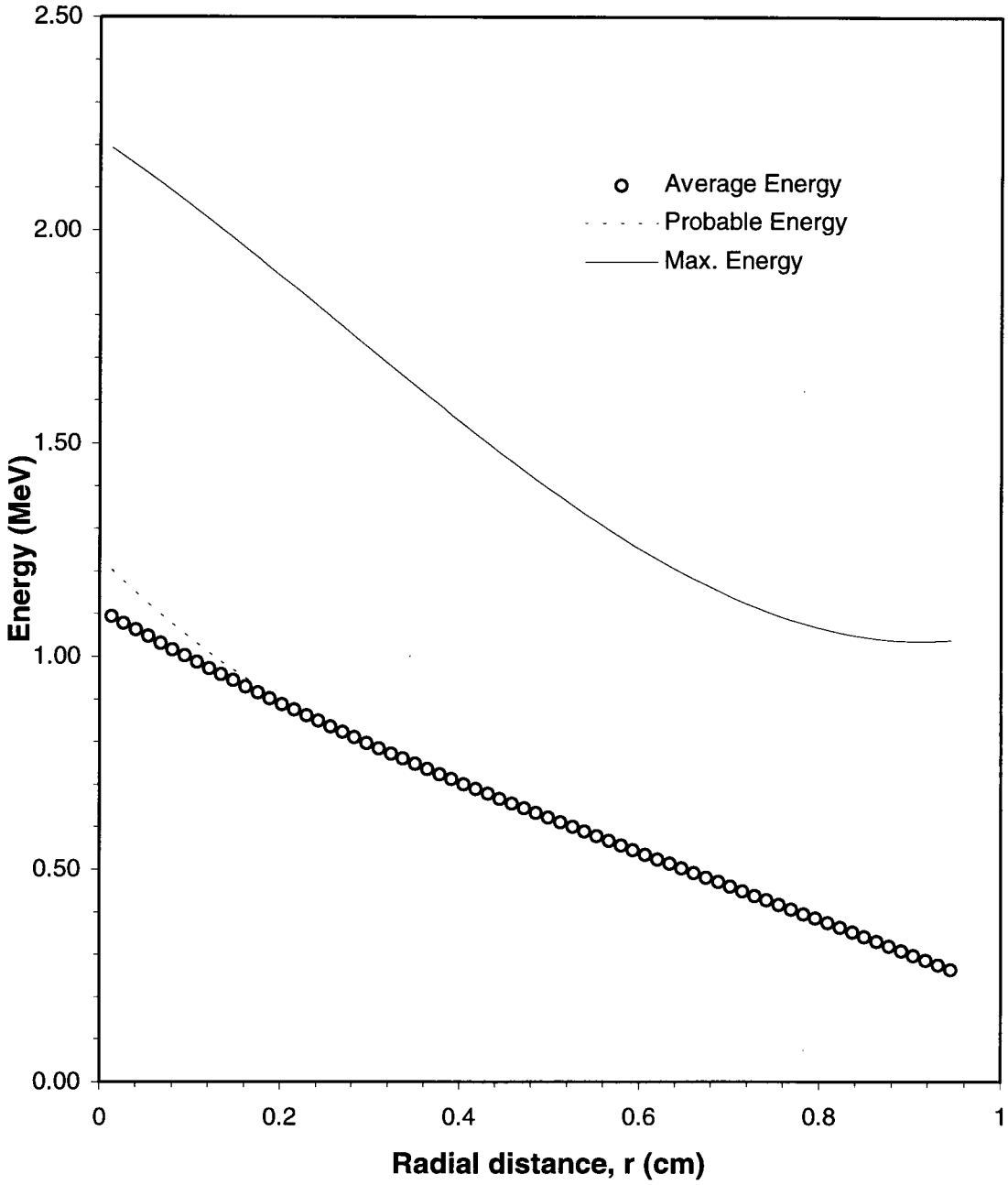

Figure 5.6 Electron average, probable, and maximum energies at different radial distances from ^{90}Y point source.

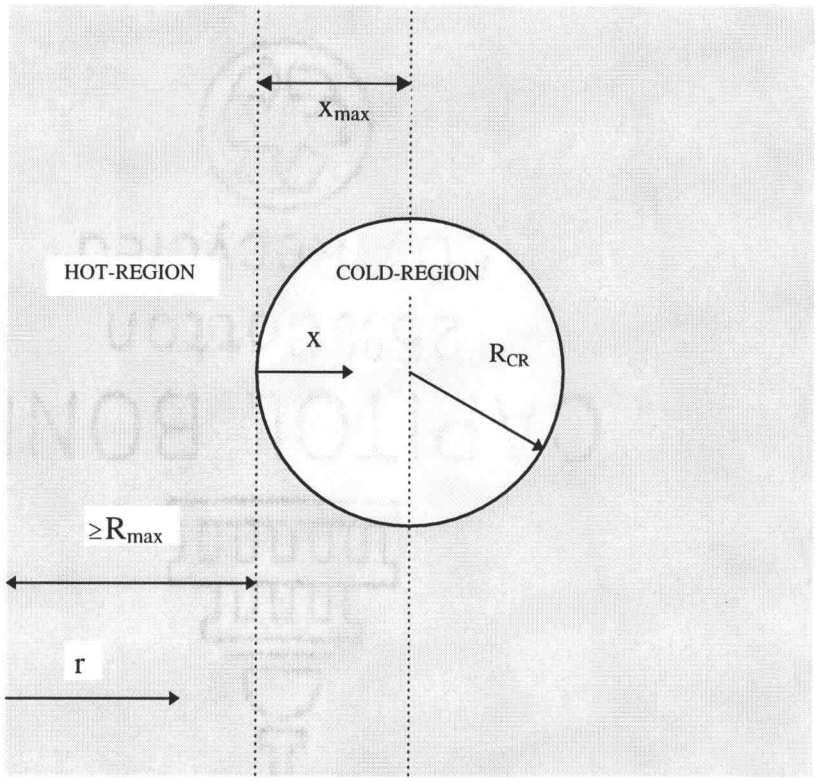

Figure 5.7 Diagram of the simple model used for the calculations of radiation dose profile across tumor cold-region.

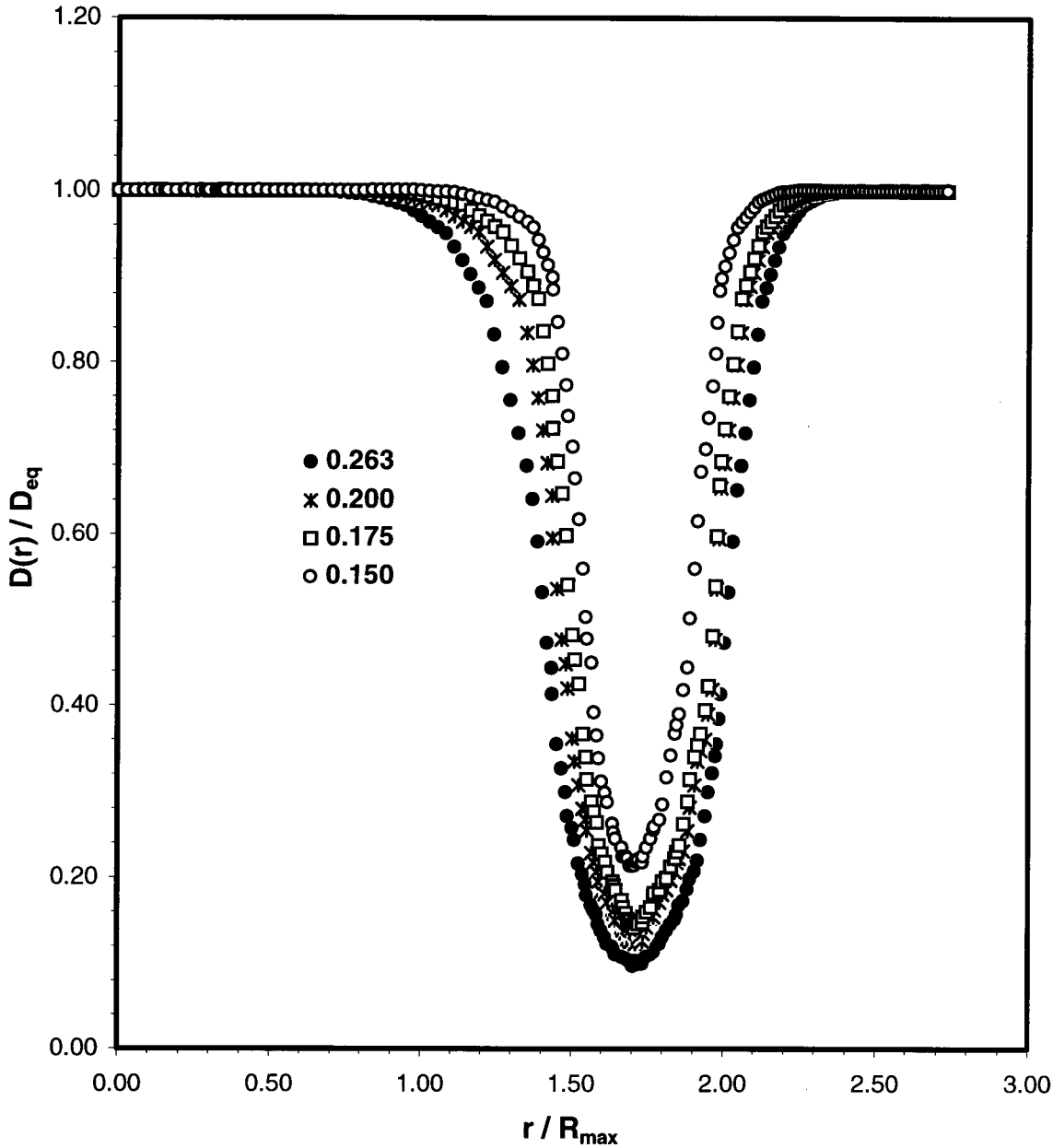

Figure 5.8 Profile of ^{90}Y beta-particle absorbed dose fraction across cold-region of radius R_{CR} (R_{CR}/R_{max} = 0.263, 0.2, 0.175, and 0.15) within tumor, surrounded by uniform distribution of ^{90}Y labeled monoclonal antibodies (hot-region).

that the minimum dose fraction for a cold region of $0.15R_{max}$ radius is 0.214 while for a $0.200R_{max}$ radius it is 0.123 and 0.097 for $0.263R_{max}$ radius. The value of the minimum dose-fraction for a cold-region of 0.025 cm radius was evaluated by extrapolation and found to be 0.84 .

5.3 ^{90}Y- Microdosimetry

5.3.1 General Remarks

An emitted beta particle may or may not result in energy deposition in the target of interest. Despite the number of interactions, a beta particle which leads to a non-zero energy deposition in the target is counted as an event. Therefore, a single event is one with any value of non-zero energy deposition. Accordingly, the mere passage of a beta particle or its secondary electrons without energy transfer to the site of interest therefore is not counted as an event. The cumulative single event density, denoted by $F_1(z)$, is the probability that the specific energy is equal or less than z. The specific energy z is the quotient of imparted energy ε by the target mass , m, [126]:

$$z = \frac{\varepsilon}{m} \tag{5-3}$$

The single event density $f_1(z)$ is the derivative of $F_1(z)$ with regard to z

$$f_1(z) = \frac{dF_1(z)}{dz} \tag{5-4}$$

The event probability, ω, is the probability that a beta particle results in an event within a specific target. With multiple primary emissions, the event probability is the fraction of total primary emission that lead to an event in a given target site. When a ^{90}Y source emits multiple primary beta particles, the target may experience no event, a single event, or multiple events. Therefore, the expected number of events, *n*, resulted from a number *N* beta particles emitted from the source is

$$n = \omega N \tag{5-5}$$

$$n = \frac{D}{\bar{z}_1} \tag{5-6}$$

Where $\bar{z}_1$ is the mean value of the single event distribution

$$\bar{z}_1 = \int_0^\infty z\, f_1(z)\, dz \tag{5-7}$$

Because events are statistically independent, the probability for the actual number of events ν can be approximated by the Poisson distribution

$$P_n(\nu)=\frac{e^{-n}\, n^{\nu}}{\nu!} \tag{5-8}$$

Consequently, the overall impact on a target should include all possible number of events. Each possibility of the number of events is accompanied by its corresponding probability density function. For a single event ($\nu=1$), the probability density is the single event density $f_1(z)$ while for two events ($\nu=2$) it is $f_2(z)$; and so on. The contribution due to different number of events, due to multiple primary emission, can be represented as a superposition of multi-events spectra $f_\nu(z)$, according to Poissonian probabilities for the occurrence of ν events

$$\begin{aligned} f(z) &= \sum_{\nu=1}^{\infty} P_n(\nu)\, f_\nu(z) \\ &= \sum_{\nu=1}^{\infty} \frac{e^{-n}\, n^{\nu}}{\nu!} f_\nu(z) \end{aligned} \tag{5-9}$$

The spectra $f_\nu(z)$ which belong to exactly ν ($\nu > 1$) events can be obtained as a convolution of lower order event densities

$$\begin{aligned} f_\nu(z) &= f_{\nu'} * f_{\nu-\nu'}(z) \\ &= \int_{z'>0}^{z} f_{\nu-\nu'}(z-z')\, f_{\nu'}(z')\; dz' \end{aligned} \tag{5-10}$$

for $\nu > 1$ and $0 < \nu' < \nu$

Fourier transformation can be used to minimize the number of convolutions required for obtaining multiple group event density, thus equation (5-9) is transformed to

$$F\{f(z)\} = \sum_{\nu=1}^{\infty} \frac{e^{-n} n^{\nu}}{\nu!} F\{f_{\nu}(z)\} \tag{5-11}$$

Where

$$\begin{aligned} F\{f_{\nu}(z)\} &= F\{f_1 * f_{\nu-1}(z)\} \\ &= F\{f_1(z)\}\ F\{f_{\nu-1}(z)\} \\ &= F_1\ F_{\nu-1} \\ &= F_1^{\nu} \qquad \text{for } \nu > 1 \end{aligned} \tag{5-12}$$

Therefore, equation (5-11) can be expressed as

$$F\{f(z)\} = \sum_{\nu=1}^{\infty} \frac{e^{-n} n^{\nu}}{\nu!} F_1^{\nu}$$

$$F\{f(z)\} = e^{-n} \sum_{v=1}^{\infty} \frac{(n F_1)^v}{v!}$$

$$= e^{-n} e^{-nF_1} \tag{5-13}$$

Also, the Fourier transform of the specific energy distribution $F\{f(z)\}$ can be calculated once the Fourier transform of the single event density F_1 or $F\{f_1(z)\}$ is given. The Fourier transform of the single event density is defined as

$$F_1(t) = F\{f_1(z)\} = \int_{-\infty}^{\infty} e^{izt} f_1(z)\, dz \tag{5-14}$$

As the Fourier transform of the specific energy distribution is obtained, the specific energy distribution $f(z)$ is finally obtained by applying the inverse Fourier transformation to the Fourier transform

$$f(z) = F^{-1}\{F\{f(z)\}\}$$

$$= \int_{-\infty}^{\infty} e^{izt} F(t)\, dt \tag{5-15}$$

It is also desirable to obtain the yield of elementary radiation sub-lesions as a function of specific energy $\in(z)$

$$\in(D) = \int \in(z)\ f(z)\, dz \tag{5-16}$$

Where $\in(D)$ is the probability of specific biological end point which usually is a measurable quantity; and $\in(z)$ can be obtained based on the adopted biological radiation model. For example, in the Theory of Dual Radiation Action (TDRA) [63], $\in(z)$ can be obtained by knowing the probability density function of specific energy z for certain dose D, $f(z)$ (sometime referred as $f(z,D)$, which can be calculated based on a single event density $f_1(z)$ as described previously)

$$\in(z) = K z^2 \tag{5-17}$$

Where K is a constant, thus, from equation (5-16)

$$\in(D) = K \overline{z^2} \tag{5-17}$$

For a random variable, the above equation can be written as

$$\in(D) = K(\bar{z}^2 + \sigma_z{}^2) \tag{5-18}$$

Where

$$\sigma_z{}^2 = \xi D \tag{5-19}$$

$$\xi = \frac{\overline{z_1{}^2}}{\bar{z}_1} \tag{5-20}$$

Where

$$\bar{z}_1 = \int z f_1(z)\, dz \tag{5-21}$$

and

$$\overline{z_1{}^2} = \int z^2 f_1(z)\, dz \tag{5-22}$$

Finally

$$\in(D) = K(D^2 + \xi D) \tag{5-23}$$

In cell survival studies, $\in(D)$ is not the probability for cellular inactivation, S(D), instead

$$S(D) = e^{-\in(D)} \tag{5-24}$$

From the previous illustration, it is clear that the single event distribution, $f_1(z)$, is one of the basic quantities needed for evaluating the biological radiation effect. Thus, the single event distribution can be considered as a finger print for every combination of

primary radiation and interaction medium. Once $f_1(z)$ is evaluated for certain problem configurations, then the microdosimetric study of the biological effect of radiation can be performed at different levels of radiation dose, D. The evaluation of the single event density is made possible by the analog Monte Carlo simulation. This kind of simulation allows the tracking of an electron from its source and scoring all different kinds of interactions as well as the energy deposition within the specified target. Then the single event distribution can be constructed by simulating large numbers of electrons and by recording the scoring frequency of each specific energy value, z.

5.3.2 Sampling Procedure

The analog Monte Carlo electron track simulation code (EMCS) was developed and used to obtain the single event density $f_1(z)$ for two different cases. In the first case, ^{90}Y is uniformly distributed on the surface of the tumor cells, hence, the initial electron (beta particle) energy was sampled from the generated ^{90}Y beta-spectrum. For the second case, the ^{90}Y source is uniformly distributed within the tumor mass so that a tumor cell (at a distance of at least one beta maximum range from the tumor mass border) is expected to be affected by electrons within a sphere of one beta maximum range. The first case is representing the small metastasis of isolated cells, e.g., circulating leukemia cells, since the only radiation dose contribution to a tumor cell is assumed to be from ^{90}Y radionuclides bounded to that cell surface and there is no cross-fire effect from other cells. The second case is the situation found in a solid tumor. Because the single event

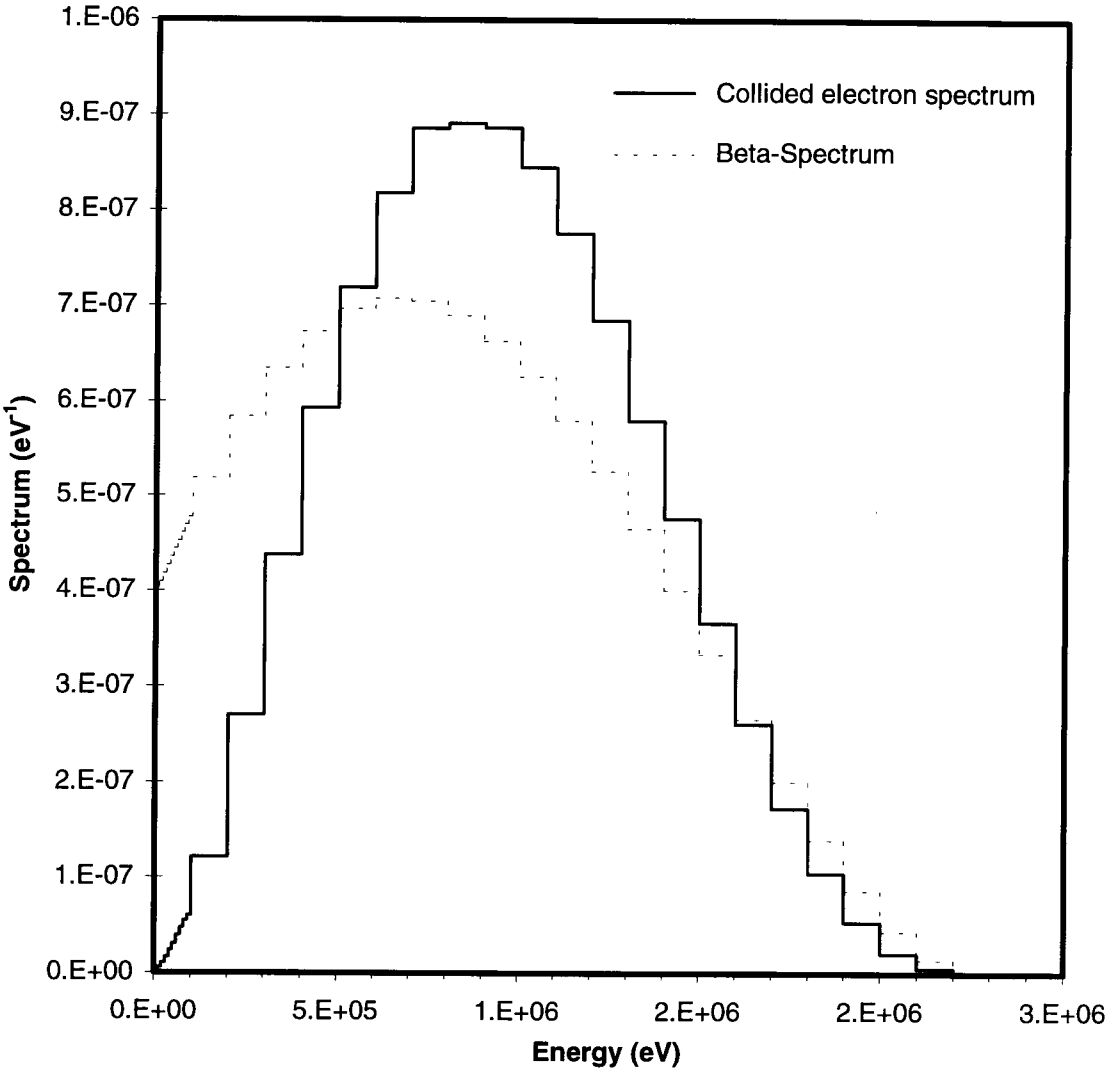

Figure 5.9 ^{90}Y beta-spectrum compared with the collided electron spectrum within tumor mass, which has a uniformly distributed ^{90}Y, calculated using MCNP-4B.

density is independent of absorbed dose D, the only difference in the two cases is the primary electron spectra. MCNP-4B was used to calculate the collided electron spectrum at the cell surface from the surrounding ^{90}Y. This is shown in Figure 5.9 compared to the ^{90}Y beta-spectrum.

The analog Monte Carlo electron track simulation code (EMCS) was used to generate randomly N primary electrons from the surface of the cell and score the corresponding value of specific energy z_i = 1, 2, ... z_n in the cell and nucleus. Certainly some of the primary electrons do not deposit their energy in the nucleus or in both the cell and the nucleus. The relationship for single event density is

$$f_1(z) = \frac{\Delta N_z}{N} \frac{1}{\Delta z} \tag{5-19}$$

Where ΔN_z is the number of primary electrons with specific energy value z_i between z and $z + \Delta z$ and N is the number of primary electrons which have energy deposition in the target. The sum distribution $F_1(>z)$ is then

$$F_1(> z) = \frac{N_z}{N} \tag{5-20}$$

The evaluation of $f_1(z)$ was performed for the nucleus and for the whole-cell. Figure 5.10 presents the single event distributions for the cell and the nucleus due to primary electrons with energy spectrum equivalent to ^{90}Y beta spectrum. Similarly, Figure 5.11

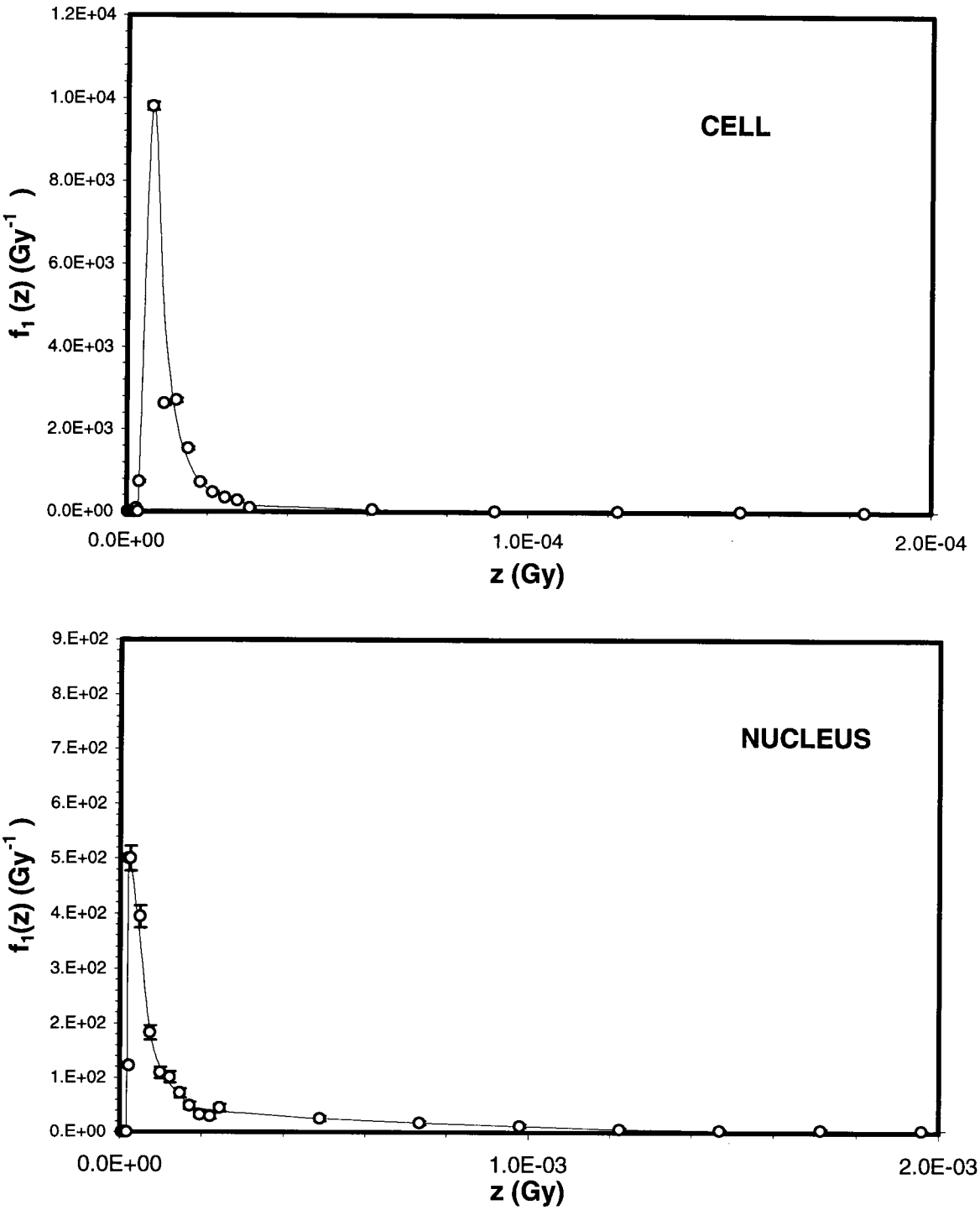

Figure 5.10 Single event distribution due to ^{90}Y for both cell and nucleus from the ^{90}Y beta spectrum.

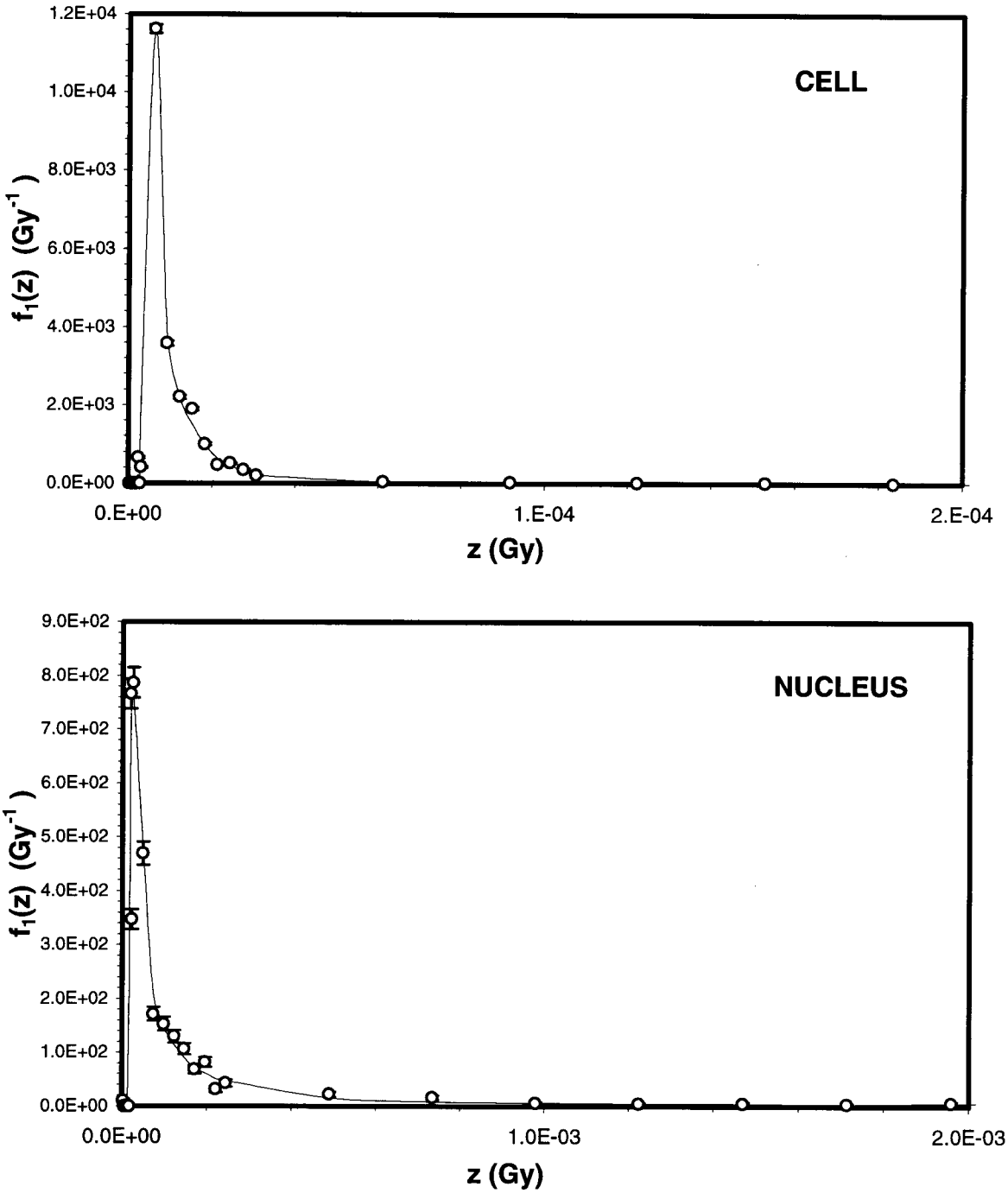

Figure 5.11 Single event distribution due to ^{90}Y for both cell and nucleus from the collided electron spectrum.

the same distribution but due to electrons with an energy spectrum equivalent to the collided electron energy spectrum shown in Figure 5.9. The number of histories was 40,000 for each case. The statistics can be improved by increasing the number of histories, however, because the electron was tracked down to very low energy (T_{cut} = 0.198 eV), the simulation time will be very long. In the low energy region, elastic scattering is the dominant interaction and the electron keeps bouncing until it escapes the cell or further losses some of its energy by one of the vibrational excitation modes. The error bars are calculated based on an assumed Poisson distribution for each point. As expected, the broadest distribution is observed for events within the nucleus. The differences between the two cases, i.e., ^{90}Y beta spectrum and collided electron spectrum, come from the different initial electron spectra. The average electron energy of ^{90}Y beta spectrum is 0.93 MeV while it is about 1.0 MeV for the collided electron energy spectrum. It is expected that for a certain target the higher the electron energies the lower the average single event specific energy. In other words, the distribution peak moves to lower energies as the initial electron energy increases.

The maximum uncertainty in all MCNP-4B calculations was lower than 10%. In the energy deposition tally (electron dose calculations) the variance reduction techniques other than those for the source card are not supported in the code. On the other hand, most of the variance techniques are supported in MCNP-4B code for other electron tallies such as in the case of calculating the electron energy spectra at different radial distances from ^{90}Y point source. In such a case, the maximum uncertainty was less than 2% within relatively feasible simulation time.

6. CONCLUSION AND DISCUSSION

6.1 Summary

Dosimetry of internally deposited beta-emitting radionuclides, particularly in radioimmunotherapy field, is complicated mainly because of their non-uniform distribution. For a known radionuclide concentration, within a homogeneous tumor body of infinite extent, the spatial distribution of radiation dose can be determined by convoluting the concentration distribution with the dose response to a point emitter in the object. Unfortunately, homogeneity of the tumor body is not the case in reality; therefore heterogeneity of the intra-tumor distribution of administered radionuclides (labeled monoclonal antibodies) can be estimated using imaging techniques. Then, calculation of the beta dose distribution from the activity distribution is straightforward if the medium is homogeneous with regard to electron transport properties

$$D(\vec{r}) = \int_V C(\vec{r}_s)\, k(|\vec{r} - \vec{r}_s|)\, dV \qquad (6\text{-}1)$$

where $C(\vec{r}_s)$ is the radionuclide concentration at $\vec{r}_s$, and $k(|\vec{r} - \vec{r}_s|)$ is the point kernel function or the dose at a point located at $\vec{r}$ due to a radionuclide concentration at $\vec{r}_s$. The beta dose distribution about a unit ^{90}Y-source in a water medium, i.e., beta dose kernel, $k(r)$, has been calculated using MCNP-4B code by direct sampling of beta particles from the generated ^{90}Y beta-spectrum. A correlation of the beta dose kernel was then

established in equation (5-2). Figure 6.1 shows the calculated beta dose kernel for the ^{90}Y point source. Figure 6.2 shows the relative radial dose profile for a uniformly distributed ^{90}Y source within a spherical volume of radius equal to twice the maximum beta range .

The effect of cold-regions and cross-fire on the dose distribution has been studied assuming a uniform distribution of ^{90}Y radionuclide within the tumor mass. The cold-regions were assumed to have spherical shapes and with zero ^{90}Y concentration. Different sizes of spherical cold-regions were studied and the dose profile across the cold-region as well as the minimum dose, due to the cross-fire effect of the surrounding ^{90}Y, were calculated for each cold-region size. For example, by extrapolating the current calculations, it was estimated that there is a maximum drop of 16 % in the dose at the center of 0.5 mm diameter cold-region.

Accurate cellular-dose estimates are essential to improve predictions of the biological effects of radiation especially when charged particle emitters are used as an internal radiation source. For small-size targets, such as the cell and the cell-nucleus, the randomness in energy deposition of beta particles at these sites becomes significant. This is because electrons (beta-particles) are weakly penetrating particles and have highly tortuous tracks. Thus, calculation of microdosimetric quantities is essential for better predictions of the biological effect of radiation. Specific energy and the single event density are among the basic microdosimetric quantities. These quantities are independent of the radiation dose and characterized by a given specific irradiation geometry, target size and shape and particle type. Therefore, they are considered as a fingerprint for the medium of certain geometrical and irradiation configuration. In this work the analog Monte Carlo code (EMCS) has been developed to simulate three dimensional histories of

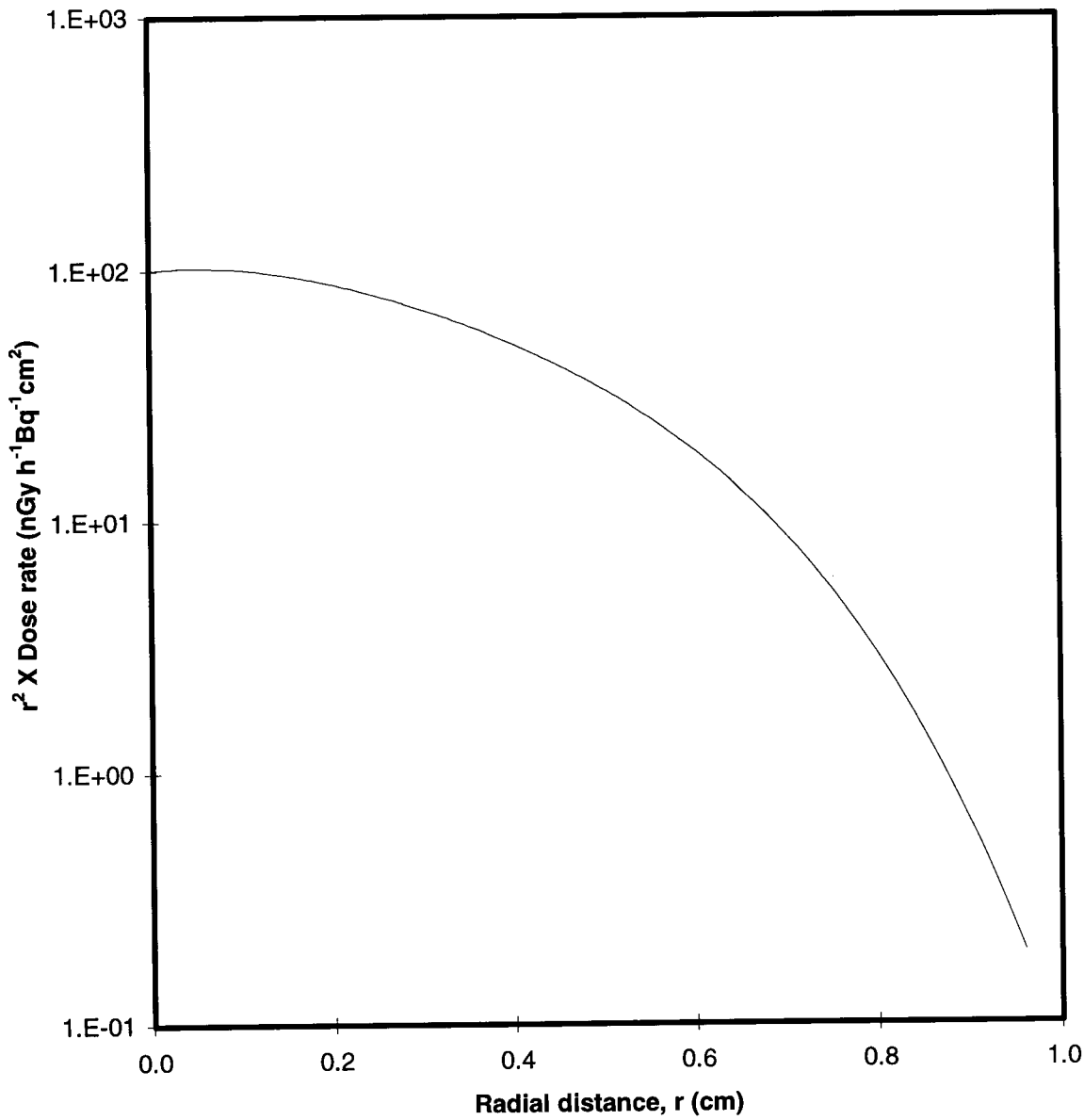

Figure 6.1 ^{90}Y beta point dose kernel calculated using MCNP-4B.

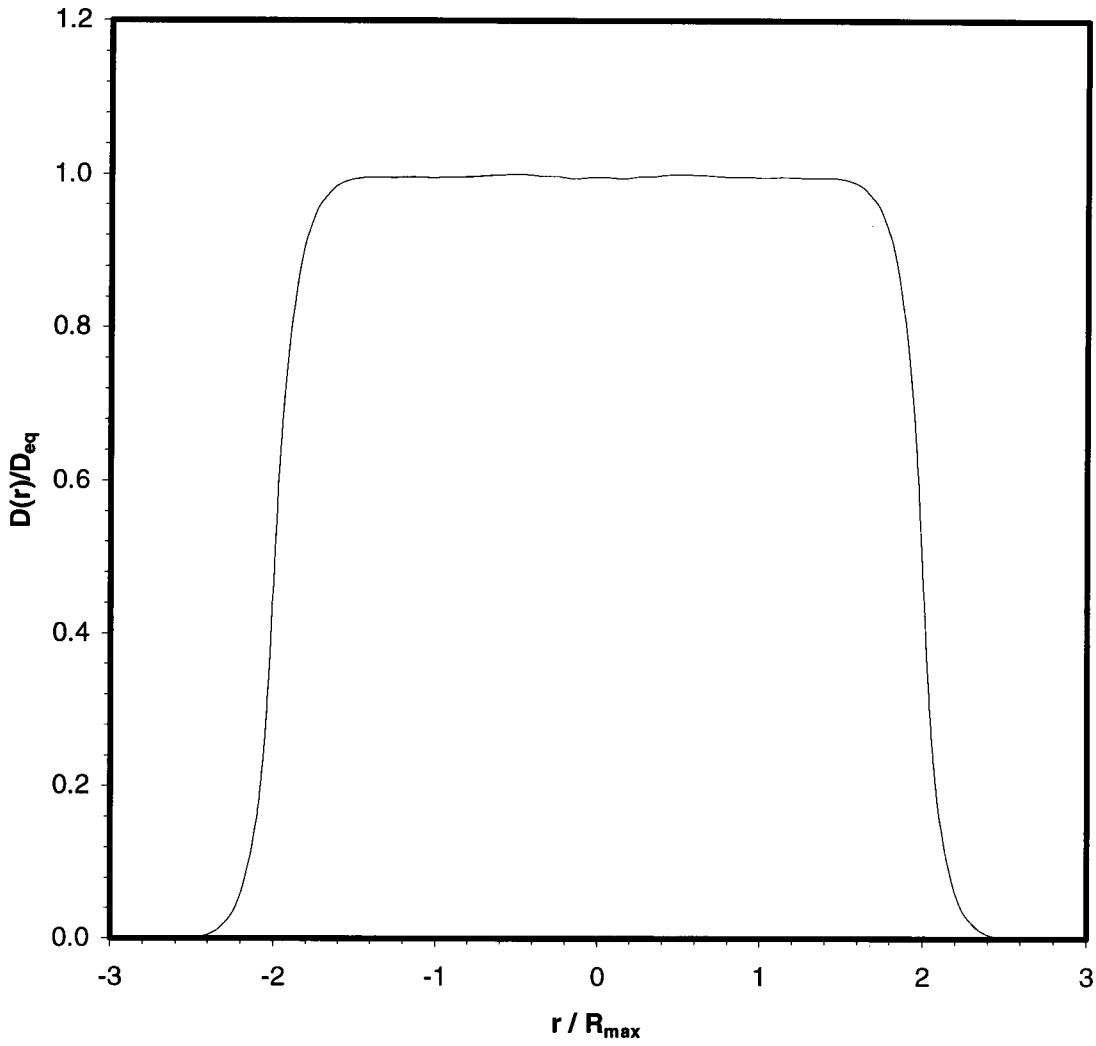

Figure 6.2 Relative radial dose profile due to a uniformly distributed ^{90}Y source within a spherical tumor of radius equal to twice the maximum beta particle range.

tracks of primary electrons (or beta particles) and molecular interactions in water vapor.

Full slowing down tracks of electrons were generated by the EMCS code which follows the full history of an electron with a starting energy sampled from a designated energy spectrum, including the history of all of its secondary electrons produced thereafter, to a selected lower energy limit, at which point the electron is diffused in a single step and its residual energy deposited at a single point The mean free path between collisions is based on energy dependent cross-sections obtained for water vapor by both measurements and theory.

The cross-sections were evaluated based on compilations of up-to-date experimental and theoretical data. The EMCS code tracks an electron down to the subexcitation energy region and the electron track is terminated when the electron energy falls bellow a cut-off energy of 0.198 eV (the lowest vibrational excitation threshold energy).

The simulation data were numerically manipulated to obtain the basic microdosimetric quantities. The single event density, $f_1(z)$, was evaluated for two different source configurations. The first is an isolated tumor cell with ^{90}Y bounded to the antigen at the cell surface and no cross-fire effect is considered (e.g., circulating leukemia). The second configuration is an individual cell within the radiation equilibrium region of a tumor mass assuming uniform ^{90}Y deposition within the tumor. Figures 6.3 and 6.4 show the single event distribution functions for both cell and nucleus for comparison and for both source configurations, respectively.

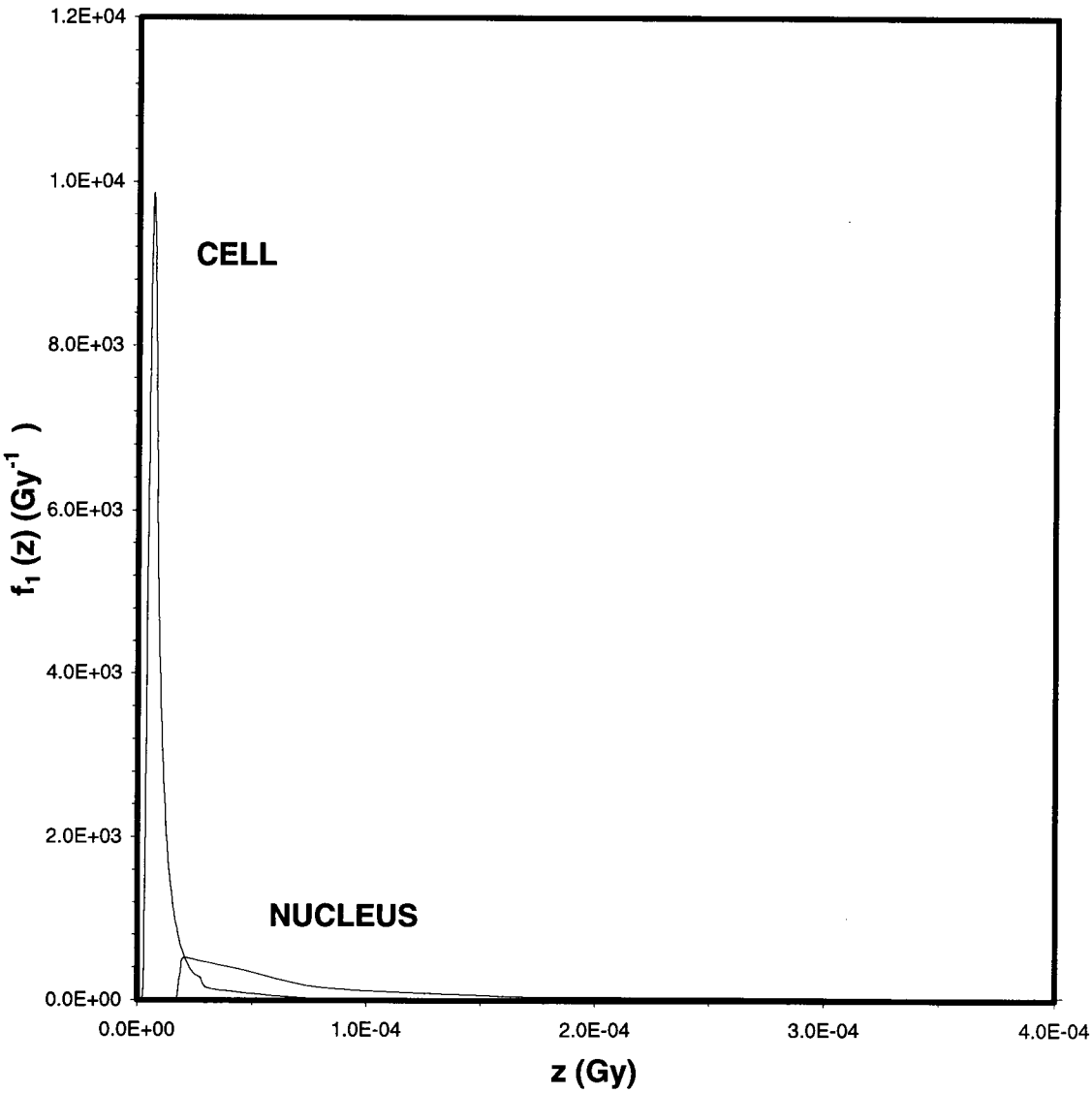

Figure 6.3 Single event distribution functions for both cell and nucleus from ^{90}Y beta-particles energy spectrum .

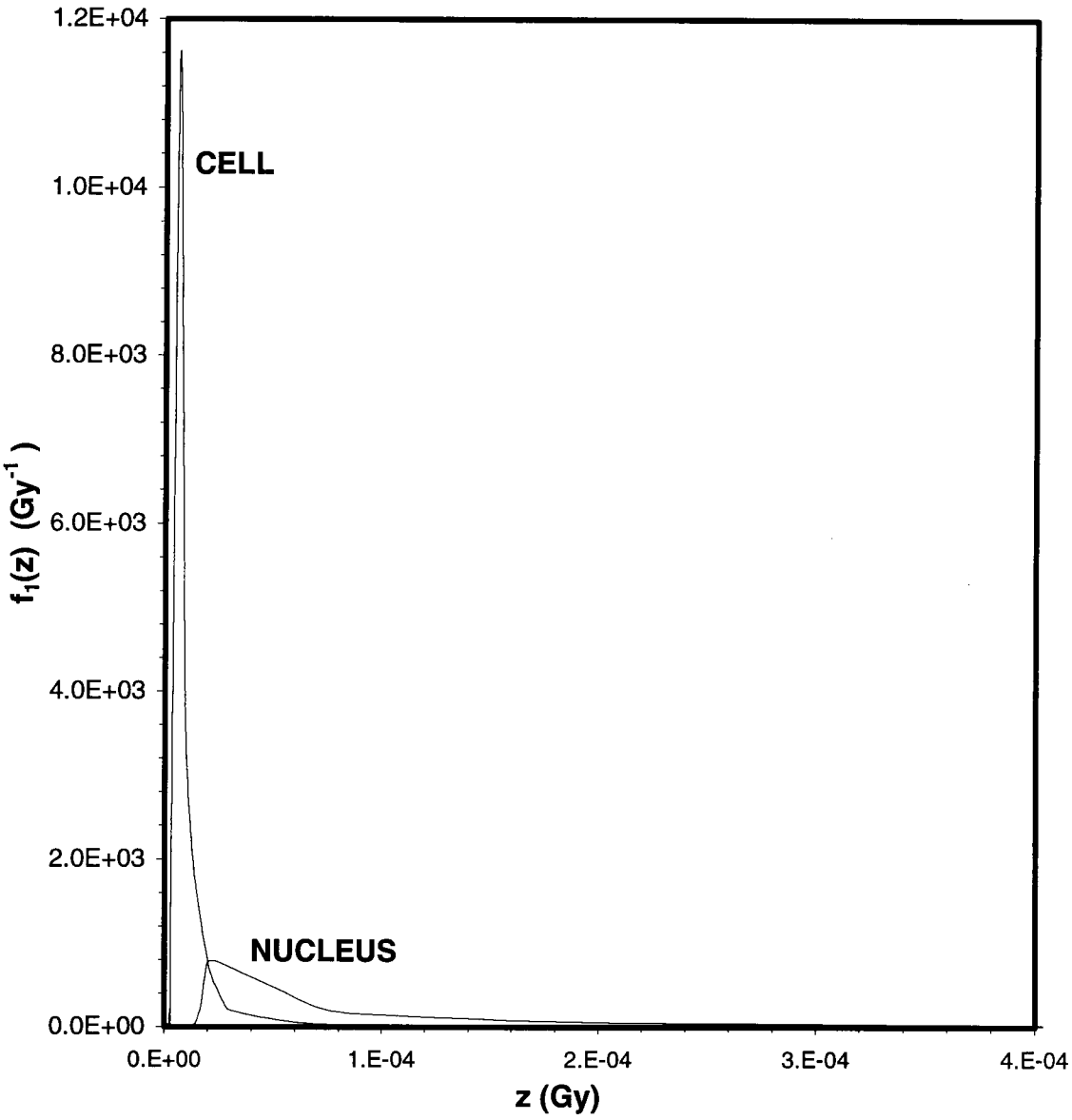

Figure 6.4 Single event distribution functions for both cell and nucleus from the collided electron spectrum within the tumor of uniformly distributed ^{90}Y

6.2 Discussion and Recommendations

In general, the MCNP-4B point kernel calculation agrees with the published data. However, the observed discrepancy with some of these published data is believed to be due to a common as well as specific causes. One of the common causes is the treatment followed in all published Monte Carlo data. In these codes, the simulation was performed for monoenergetic electrons, then averaged over the ^{90}Y beta spectrum, while in the MCNP-4B calculation, the initial electron was sampled directly from the generated ^{90}Y beta spectrum. Furthermore, the sizes of the shells used to calculate the dose profile were not similar. The cutoff energy of the EGS4 code was 10 keV which is one order of magnitude higher than the cutoff energy used in MCNP-4B calculations. The number of histories of the MNCP-4b calculation was 1.35 x 10^6, and the computation time was about 900 minutes. This number of histories was enough to reduce the statistical fluctuation down below 10%, especially for points far away from the point source. Unfortunately, there is no published data for dose distribution measurements in water.

The radiosensitivity of a population of tumor cells is often expressed by D_0, which is the reciprocal of the slope of the linear portion of the survival curve. Therefore, the dose, D, required to reduce the cell population to a certain level of cell survival, S, can be extrapolated from the equation

$$D = -D_o \ln S \tag{6-2}$$

For 1% cancer cell survivors, the required dose, D, is $4.605D_o$. However, because of the cold-regions, the total administered ^{90}Y activity should be sufficient to provide enough dose within the largest cold-region in the tumor. For example, the calculations of the cold-region effect show that for a 5 mm diameter cold-region, under the specified assumputions, the dose required to reduce the population of the survived cells within the cold-region to 1%, is 1.2 D. By using a different beta emitting radionuclides with lower endpoint energy, the dose received by that cold-region may not be enough to provide the required sterilization level within the cold-region. Consequently, the optimum radionuclide for radioimmunotherapy of solid tumors would be one in which the mean range of beta particles is comparable to the largest cold-region diameter in the tumor. However, in practice, information on cold-regions is not known and experimental studies on the extravascular movement of antibody through tumors are necessary to show the antigen distribution, hence, the size of the cold-regions. On the other hand, for a single cell cancer (e.g., circulating leukemia), the cross fire effect is undesirable because this may result in unnecessary dose to normal organs, especially bone marrow. In this case, a shorter range beta emitting or possibly alpha emitting isotopes are the best nominated sources. In this circumstance, the range should be comparable to the cell diameter.

Radiolabeled antibodies distribute non-uniformly in living tissue and tumors, resulting in non-uniform dose distribution. These will lead to non-uniform tissue response to radiation energy for a given absorbed dose. The absorbed dose is a statistical mean value of a large number of sub-units representing the specific energy imparted to microscopic parts of which the target tissue is consisted. The actual amount of specific energy is highly variable and depends on the microscopic distribution of individual

energy deposition events relative to the distribution of cell nuclei. An understanding of the relationships between localized dose and biological response may be obtained by examining the distribution of energy deposition at the appropriate cellular or sub-cellular level. A better understanding of these relationships may enable one to predict more accurately the effects of radiation, and thus improve treatment planning and, of course, radiation protection. The basic microdosimetric quantities, the specific energy and single event density, are the basic ingredients for several biological models, such as the theory of dual radiation action (TDRA), which are used to predict the biological effect of radiation. For this purpose, the analog Monte Carlo code (EMCS) was constructed and used to simulate electron tracks initially emitted from the cell surface with energies sampled from the designated spectrum. The track structure data were manipulated to obtain the single event density for events within a 10 micrometer cell and 5 micrometer nucleus. The shapes of $f_1(z)$, for the events within the cell and the nucleus and for two different initial electron spectra, are as expected. The broadest distribution is observed for events within the nucleus. The statistical fluctuations in the single event density can be reduced by simulating larger number of histories, however, this may not be feasible with the current available computational tools. The single event densities for the cell and nucleus will be broader if another beta emitting isotope with lower end point energy is used instead of the ^{90}Y isotope. On other words, the frequency mean specific energy per event for this isotope will be larger. The EMCS code is based on cross sections obtained for water vapor normalized to liquid water density. This limitation arises from considerable shortcomings of the availability of electron cross section data which can be used for the simulation of electron transport in the water condensed phases, protein and

DNA. The cross sections used in EMCS code may distort the accuracy of the results because of the following factors:

1. Liquid water was considered the simulation medium (although it is not necessarily the ideal model for cellular medium simulation), however, water vapor cross sections were used instead. This is because the measurements of the electron interactions, or charged particles in general, with an isolated water molecule can be made in the gaseous or vapor phase. Nevertheless, a molecule does not act individually in the liquid (or solid) phase. In these phases, the interactions are influenced by the neighboring molecules. Elastic scattering, electronic excitation, dissociative attachment, and vibrational excitation modes are present in both phases. However, there are differences such as the ionization potential for liquid phase is lower than in vapor phase. Moreover, our knowledge of the cross section for water vapor at low energy region is far from satisfactory.
2. An electron in the course of traversing a medium interacts with one scattering center at a time. This implies the neglect of quantum-mechanical interference (electron diffraction) resulting from the coherent scattering by several centers. The trajectory of the particle is thus idealized by a zig-zag path, consisting of free flights interrupted by sudden collisions in which the energy and direction of the electron are changed.
3. Due to the present energy resolution limitation, individual rotational transition at low energy region is usually not separable from pure elastic scattering. Accordingly, the reported experimental elastic scattering cross section is interpreted as the vibrationally elastic cross section. Therefore, the energy loss due to rotational excitation is not considered in the simulation. Moreover, the energy loss due to momentum transfer in

elastic scattering is not considered in the simulation as well. The energy losses due to the above two types of interactions are small and not comparable to the losses due to electronic excitation or ionization interactions. However, because of the large population of subexcitation electrons, the energy deposition due to these two interactions, which are the only known energy loss mechanisms in the low subexcitation energy region, can form an appreciable fraction of the total energy deposition.

4. The present cross sections are one of the most up-to-date and based on experimental data, particularly at low energy range. Further understanding of electron interactions in the low energy region is essential for more precise simulation and understanding of radiation effects.
5. All experimental or theoretical cross section data were evaluated at room temperature. Some of the electron interactions, such as dissociative electron attachment and molecular vibrational excitation, show strong dependency on temperature.

Therefore, it is recommended to obtain cross sections for water in liquid phase and for the major cellular molecules based on experimental measurements. Detailed investigation of electron interactions at subexcitation energies is highly recommended for better understanding of the subexcitation electron behavior in the interacting medium. Obviously, electrons with energies higher than the first electronic excitation energy slow faster than subexcitation electrons, i.e., those with energies below the first electronic excitation threshold. Nevertheless, the subexcitation electrons are important in several contexts including the formation of negative ions, which are precursors to certain chemical changes in the cell. The role of the subexcitation electrons is conspicuous when

the irradiated water contains small amounts of substances whose excitation or ionization energies lie below the first threshold of the electronic excitation of water, because their molecules can be excited or ionized by the subexcitation electrons.

When the electron kinetic energy becomes less than or equal to the cut off energy, its kinetic energy is assumed to be deposited in a single step at a single point. Large fractions of the electrons escape the target with or without depositing some of their kinetic energy, nevertheless, a considerable fraction of these electrons die within the target because their kinetic energies become less than the cut off energy. The energy of these dead electrons may substantially affect the results. For example, if it is of interest to calculate the number of DNA strand breaks obtained from the energy deposited by these electrons, the extra energy may be sufficient to raise the energy deposited above the assumed small threshold values for producing a strand break.

The disintegration of incorporated ^{90}Y radionuclides, or in general any other radioisotope, may cause distinguished effect which can not be seen in external radiation. The fast atomic shell rearrangement after a beta decay may cause the formation of ion and free radicals. Moreover, the mechanical recoil energy of the daughter nucleus may play a significant role for genetic effects. Detailed physical study of this phenomenon is recommended for better prediction of the radiation biological effect.

Time evolution is an important aspect in radiation effects, especially in a living medium where the repair process rate occur along with the effect of dose rate on the prediction of the radiation biological effect. Introducing the time frame into the electron track simulation would provide a more precise picture of the radiation effects.

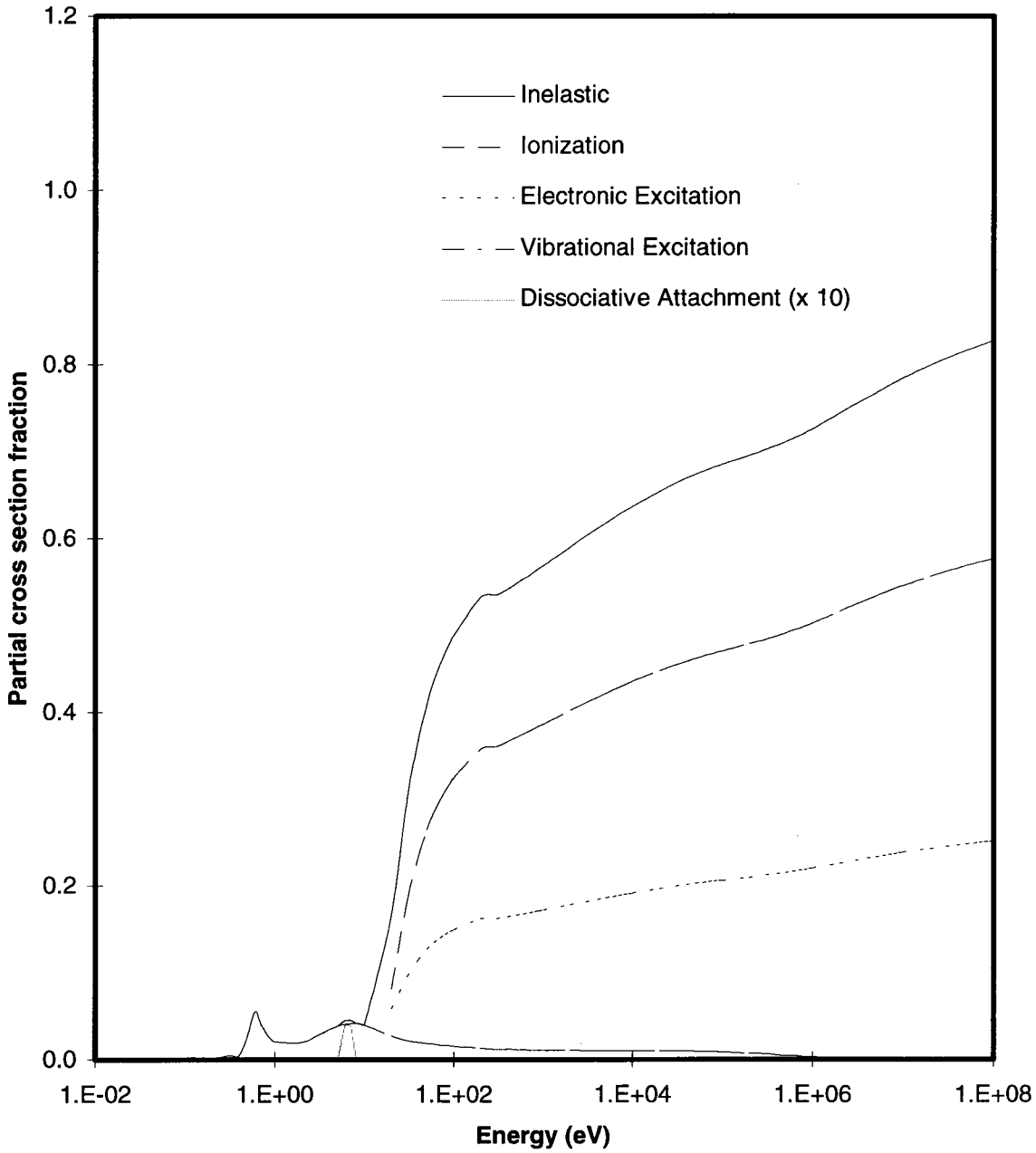

Figure 6.5 Inelastic fraction cross section.

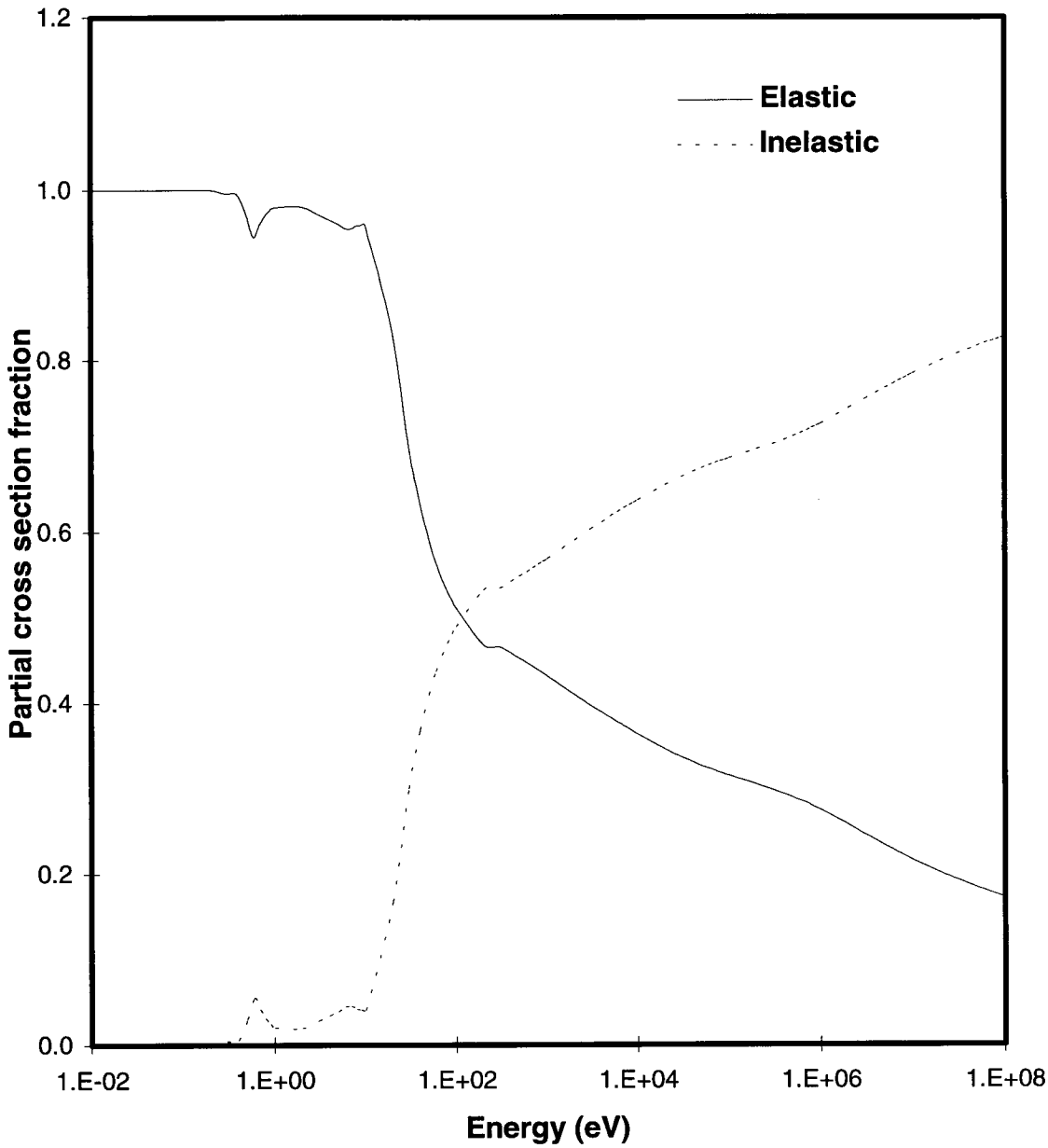

Figure 6.6 Fraction cross section as a function of electron kinetic energy in water vapor.

Speeding up the simulation computations is essential for better statistics for both the condensed walk Monte Carlo and the analog Monte Carlo simulations. Faster computational facilities are necessary even for micrometer size targets because of the large number of electron Coulomb interactions especially at low energies as it can be seen from the fractional interaction cross section in Figures 6.4 and 6.5. One way to speed up the calculations is to perform the simulation on parallel processor systems.

Finally, evaluation of beta point dose kernels for different isotopes of interest in radioimmunotherapy is recommended. Similarly, evaluation of single event density for these isotopes and for different cell/nucleus dimensions may help establishing a general correlation for the single event density for any beta emitting isotope and for any cell/nucleus configuration.

BIBILOGRAPHY

1. Berger, M. J., and Seltzer, S. M.. 1968. ETRAN Monte Carlo Code System for Electron and Photon Transport Through Extended Media, Report CCC 107, Radiation Shielding Information Center, Oak Ridge National Laboratory, Oak Ridge, TN.

2. Seltzer, S.M. 1988. An Overview of ETRAN Monte Carlo, Methods for Coupled Electron/Photon Transport Calculations, International School of Radiation Damage and Protection, 8th Course: Monte Carlo Transport of Electrons and Photons below 50 MeV, Ettore Majarana Center for Scientific Culture, Erice, Italy.

3. Halbleib, J.A. 1980. ACCEPT: a Three-dimensional Electron/Photon Monte Carlo Transport Code Using Combinatorial Geometry, *Nucl. Sci. Eng.*, 75:200-201.

4. Halbleib, J.A. 1988. Structure and Operation of the ITS Code System, In Monte Carlo Transport of Electron and Photons, Jenkins, T.M.; Nelson, W.R. and Rindi, A eds. , pp. 249-262., Plenum Press, New York.

5. Halbleib, J.A., and Mehlhorn, T.A. 1984. ITS: The Integrated TIGER Series of Coupled Electron/Photon Monte Carlo Transport Codes, Report No. SAND 84-0573, Sandia National Laboratories, Albuquerque, NM.

6. Halbleib, J.A., and Mehlhorn, T.A. 1986. ITS: The Integrated TIGER Series of Coupled Electron/Photon Monte Carlo Transport Codes, *Nucl. Sci. Eng.*, pp. 338-339.

7. Halbleib, J.A., and Kensek, R. 1991. ITS 2.1 Integrated TIGER Series of Coupled Electron/Photon Monte Carlo Transport Code System, Report No. CCC 467, Radiation Shielding Information Center, Oak Ridge National Laboratory, Oak Ridge, TN.

8. Nelson, W.R., and Rogers, D.W.O. 1988. Structure and Operation of The EGS4 System, International School of Radiation Damage and Protection, 8th Course: Monte Carlo Transport of Electrons and Photons Below 50 MeV, Ettore Majarana Center for Scientific Culture, Erice, Italy.

9. Nelson, W.R.; Hirayama, H.; and Rogers, D.W.O. 1985. The EGS4 Code System, Report No,. SLAC-265, Stanford Linear Accelerator Center, Stanford, CA.

10. Briesmeister, J. ed. 1997, MCNP-4B General Monte Carlo Code for Neutron and Photon Transport, Report No. LA-12625, Los Alamos National Laboratory, Los Alamos, CA.

11. Paretzke, H.G. 1974. An Appraisal of the Relative Importance of Radiobiology of Effect of Slow Electrons, Fifth Sym. On Microdosimetry, report No. EUR-5452, Booz, J, et al. eds. pp. 41-58, CEC, Luxembourg.

12. Paretzke, H.G. 1980. Advances in Energy Deposition Theory. Advances in Radiation Protection Dosimetry in Medicine, Thomas, R.H. eds., pp. 51-73, Plenum Press, New York.

13. Paretzke, H.G. 1987. Radiation Track Structure Theory, Kinetics of Nonhomogeneous Processes, freeman, G.R. ed, pp. 89-170, Wiley-Interscience, New York.

14. Zaider, M.; Bernner, D.J.; and Wilson, W.E. 1983. The Application of Track Calculations to Radiobiology, I. Monte Carlo Simulation of Proton Tracks. *Radiat. Res.* 95:231-247.

15. Ito, A. 1987. Calculation of Double Strand Break Probability of DNA for Low LET Radiation Based on Track Structure Analysis. In Nuclear and Atomic Data for Radiotherapy and Related Radiobiology, pp. 413-429, International Atomic Energy Agency, Vienna, Austria

16. Lappa, A.V. et al. 1993. Trion Code for Radiation Action Calculations and Its Application in Microdosimetry and Radiobiolgy, *Rad. Environ. Biophysics*, 32:1-19.

17. Uehara, S.; Nikjoo, H.; and Goodhead, D.T. 1993. Cross-sections for Water Vapour for Monte Carlo Electron Track Structure Code from 10 eV to MeV region, *Phys. Med. Biol.*, 38:1841-1858.

18. Turner, J.E. et al. 1980. Early Events in Irradiated Water, Proceeding of the 7th Symp. on Microdosimetry, Booz, J.; Ebert, H.G.; and Harfiel, H.D. eds., pp. 507-520, Harwood Academic Publishers, London.

19. Terrisol, M.; Patau, J.P.; and Eudaldo, T. 1978. Application A la Microdosimetrie e a la radiobiologie de la Simulation du Transport Des Electrond de Basse Energie Dans l'eau a l'etat liquid. Proceeding of the 6th Sym. On Microdosimetry, Booz, and Ebert H.G. eds. pp 169-178, Harwood Academic Publishers, London.

20. Kaplan, I.G.; Miterev, A.M.; and Sukhonosov, V. Ya. 1990. Simulation of Primary Stage of Liquid Water Radiolysis, *Radiat. Phys. Chem.*, 36:493-498.

21. Hill, M.A.; and Smith, F.A. 1993. Calculation of Initial and Primary Yields in The Radiolysis of Water, *Radiat. Phys. Chem.* , 43:265-280.

22. Loevinger, R.L. 1954. The Dosimetry of Beta Radiation, *Radiology*, 62:74-82.

23. Cross, W.G. 1967. The Distribution of Absorbed Energy from a Point Beta Source, *Can. J. of Phys.*, 45:2021-2040.

24. Spencer, L.V. 1955. Theory of Electron Penetration, *Phys. Rev.*, 98:1597-1615.

25. Spencer, L.V. 1959. Energy Deposition by Fast Electrons, National Bureau of Standards, Monograph 1, Washington DC.

26. Berger, M.J. 1973. Improved Point Kernels for Electron and Beta Ray Dosimetry, National Bureau of Standards, Report No. NBSIR-73-107, Gaithersburg, MD.

27. Bethe, H.A. 1930. Zur Theorie des Durchgangs Schneller Korpularstrahlen Durrch Materie, *Ann. Phys.*, 5, p. 325.

28. Cross,W.G. 1967. Tables of Beta Dose Distribution, Report No. AECL 2793, Atomic Energy of Canada Ltd., Chalk River, Ontario, Canada.

29. Berger, M.J. 1971. Distribution of Absorbed Dose Around a Point Source of Electron and Beta Particles in Water and Other Media, *J. Nucl. Med.*, 12 (Suppl. 5).

30. Cross, W.G. et al. 1982. Tables of Beta Ray Dose Distributions in Water, Air and Other Meida. Report No. AECL 7617, Chalk River, Atomic Energy of Canada Ltd., Ontario, Canada.

31. Berger, M.J. 1963. Monte Carlo Calculations of the Penetration and Diffusion of Fast Charged Particles, Methods Comput. Phys. , 1:135-215.

32. Ford, RL; and Nelson, W.R. 1978. The EGS Code System-Version 3, Report No. SLAC 210, Stanford Linear Accelerator Center, Palo Atto, CA .

33. Rogers, D.W. 1984. Low Energy Electron Transport With EGS, *Nucl. Inst. Methods*, 227:535-548.

34. Simpkin, D.J.; and Mackie, T.R. 1990. EGS4 Monte Carlo Determination of the Beta Point Kernel in Water, *Med. Phys*, 17:179-186.

35. Cross, W.G.; Freedman, N.O.; and Wong, P.Y. 1992. Beta-ray Distributions from Point Sources in an Infinite Water Medium, *Health. Phys.*, 63 (2):160-171.

36. Bardiés, M.; and Chatal, J.F. 1994. Absorbed Dose for Internal Radiotherapy from 22 Beta-emitting Radionuclides: Beta Dosimetry of Small Spheres, *Phy. Med. Biol.*, 39: 961-981.

37. Loveinger, R; Budinger, T.F.; and Watson, E.E. 1991. MIRD Primer for Beta Absorbed Dose Calculation, Society of Nuclear Medicine, New York.

38. National Council on Radiation Protection and Measurements.1985. General Concepts for the Dosimetry of Internally Deposited Radionuclides: Recommendations of the National Council on Radiation Protection, NCRP Report No. 84.

39. Prestwich, W.V.; Nunes, J; and Kwok, C.S. 1989. Beta Dose Point Kernels for Radionuclides of Potential Use in Radioimmunotherapy, *J. Nucl. Med.,* 30:1036-1046.

40. Kwok, C.S.; Prestwich, W.V.; and Wislon, B.C. 1985. Calculation of Radiation Doses for Nonuniformly Distributed β and γ Radionuclides in Soft Tissue, *Med. Phys.*, 12:405-412.

41. Eckerman, K.F. et al. 1986. Traversal of Cells by Radiation and Absorbed Fraction Estimates for Electrons and Alpha Particles, In Proceeding Fourth Int. Radiopharmaceutical Dosimetry Symp. , Schlafko-Seltsou, A.T.; and Watson, E.E. eds., Conf-85113, pp. 67-81, Oak Ridge, TN.

42. Kwok, C.S. et al. 1987. Beta Dosimetry for Radioimmunotherapy of Cancer Using Labeled Antibodies, NCI Monograph No. 3, pp. 73-82.

43. Langmuir, V.K.; and Sutherland, R.M. 1988. Dosimetry Model for Radioimmunotherapy, *Med. Phys.*, 15:567-573.

44. Humm, J.; and Cobb, L.M. 1990. Nonuniformity of Tumor Dose in Radioimmunotherapy, *J. Nul. Med.*, 31: 75-83.

45. Press, O. et al. 1989. Treatment of Refractory Non-Hodgkin's Lymphoma With Radiolabeled MB-1 (anti-CD37) Antibody. *J. Clin. Oncol.*, 7:1027-1038.

46. Eary, J.F. et al. 1990. Imaging and Treatment of B-cell Lymphoma, *J. Nucl. Med.*, 31:1257-1268.

47. Jain, R.K.; and Baxter, L.T. 1988. Mechanisms of Heterogeneous Distribution of Monoclonal Antibodies and Other Macromolecules in Tumors: Significance of Elevated Interstitial Pressure, *Cancer Res.*, 48:7022-7032.

48. Cobb, L.M. 1989. Intratumor Factors Influencing Access of Antibody to Tumor Cells, Cancer Immunol. Immunother., 28:235-240.

49. Edwards, P.A.W. 1985. Heterogeneous Expression of Cell-Surface Antigens in Normal Epithelia and their Tumors, Revealed by Monoclonal Antibodies, *Br. J. Cancer*, 51:149-160.

50. Enblad, P. Et al. 1987. Antigen Heterogeneity in Adeno Carcinomas of The Rectum and Their Secondaries, *Br. J. Cancer,* 55:503-508.

51. Ettinger, D.S. et al. 1982. Phase I-II Study of Isotopic Immunoglobulin Therapy for Primary Liver Cancer, *Cancer Treament Rep.,* 66:289-297.

52. Lechner, P.K. et al. 1983. Dosimetry of ^{131}I-Labeled Antiferritin in Hepatoma: Specific Activities in Tumor and Liver, *Cancer Treatment*, 67,7-8:647-658.

53. Wessels, B.W.; and Rogus, R.D. 1984. Radionuclides Selection and Model Absorbed Dose Calculations for Radiolabeled Tumor Associated Antibodies, *Med. Phys.*, 11:638-645.

54. O'Brien, H.A. Jr. 1983. Overview of Radionuclides Useful for Radioimmunoimaging/Radioimmunotherapy and Current Status of Preparing Radiolabeled Antibodies, In Radioimmunoimaging and Radioimmunotherapy, Burchiel, S.W.; and Rhodes, B.A. eds, New York, Elsevier, pp. 161-169.

55. Jungermann, J.A.; Kin-Hung, P. Yn; and Zanelli, C.I. 1984. Radiation Absorbed Dose Estimates at the Cellular Level for Some Electron-emitting Radionuclides for Radioimmunotherapy, *Int. J. Appl. Radiat. Isot.*, 35:883-888.

56. Leonard, F.M.; and Srivastava, S.C. 1993. Selection of Radionuclides for Radioimmunotherapy, *Med. Phys.,* 20, 2:503-509.

57. DeNardo, S.J. et al. 1983. The Choice of Radionuclides for Radioimmunotherapy, Proc. of the Symp.on Developing Role of Shorter-Lived Radionuclides in Nuclear Medical Practice, Paras, P.; and Thiesses, J.W. eds., DOE Conf 820523, Washington DC.

58. Humm, J.L. 1987. A Microdosimetric Model of Astatine-211 Labeled Antibodies for Radioimmunotherapy, *Int. J. Radiat. Oncol. Biol. Phys,* 13:1767-1733.

59. Makrigioros, G.M. 1989. Limitations of Conventional Internal Dosimetry at the Cellular Level, *J. Nucl. Med.*, 30:1856-1864.

60. Rossi, H.H. 1968. Microscopic Energy Distribution in Irradiated Matter, In: Radiation Dosimetry, Vol. I, Attix, F.H.; and Roesch, W.C. eds., Academic Press Inc., New York, NY.

61. Roesch, W.C. 1977. Microdosimetry of Internal Sources, *Radiat. Res.*, 70:494-510.

62. Fisher, D.R. 1986. The Microdosimetry of Monoclonal Antibodies Labeled With Alpha Emitters. In Proceedings of the Fourth International Radiopharmaceutical Dosimetry Symp., Schlafke-Stelson, A.T.; and Watson, E.E., eds., DOE Conf 85113, Oak Ridge, TN.

63. Kellerer, A.M.; and Rossi, H.H. 1972. The Theory of Dual Radiation Action, *Curr. Top. Radiat. Res.,* Q-8:85-158.

64. Kellerer, A.M.; and Rossi, H.H.1978. A Generalized Formulation of Dual Radiation Action, *Radiat. Res.*, 75:471-488.

65. Kellerer, A.M.; Lam, Y.M.P.; and Rossi, H.H. 1980. Biophysical Studies With Spatially Correlated Ions. 4. Analysis of Cell Survival Data for Diatomic Deuterium, *Radiat. Res.,* 83:511-528.

66. Bernner, D.J.; and Zaiser, M. 1984. Modification of the Theory of Dual Radiation Action for Attenuated Fields. II. Application to the Analysis of Soft X-rays Result, *Radiat. Res.,* 99:492-501.

67. Zider, M.; and Bernner, D.J. 1984. The Application of Track Calculations to Radiobiology. III. Analysis of the Molecular Beam Experiment Results, *Radiat. Res.,* 100:213-221.

68. Zider, M.; and Ross, H.H. 1985. Dual Radiation Action and the Initial Slope of Survival Curves, *Radiat. Res.*, 104:S68-S76.

69. Kassis, A.I. et al. 1988. Positional Effects of Auger Decays in Mammalian Cells in Culture. In DNA Damage by Auger Emitters, Baverstock, K.F.; and Charlton, D.E. eds., pp. 1-13, Taylor & Francis, London.

70. Hofer, K.G. 1980. Radiation Biology and Potential Therapeutic Applications of Radionuclides, *Bull Cancer,* 67:343-353.

71. Painter, R.B. 1980. The Role of DNA Damage and Repair in Cell Kill Induced by Ionizing Radiation. In Radiation Biology of Cancer Research, Meyn, R.E.; and Wither, H.R. eds., pp. 59-68, Raven, New York.

72. Berger, M.J.; and Wang, R. 1988. Multiple Scattering Angular Deflections and Energy-loss Straggling, International School of Radiation Damage and Protection:8th Course: Monte Carlo Transport of Electrons and Photons Below 50 MeV, Ettore Majarana Center for Scientific Culture, Erice, Italy.

73. Goudsmit, S.; and Sanderson, J.L. 1940. Multiple Scattering of Electrons, *Phys. Rev.*, 57,24.

74. Landau, L. 1944. On the Energy Loss of Fast Particles by Ionization, *J. Phys. USSR,* 8,201.

75. Blunck, O.; and Leisegang, S. 1950. Zum Energiererlust Schneller Electronen in Dünnen Schichten, *Z. Physik,* 128, 500.

76. Møller, C. 1932. Zur Theorie des Durchang Schneller Elektronen Durch Materie, *Ann. Physik.*, 14, 568.

77. International Commission on Radiation Units and Measurements. 1984. Stopping Power for Electrons and Positrons, ICRU Report No. 37, Bethesda, MD.

78. Kaplan, I.G., and Miterev, A.M. 1987. Interaction of Charged Particles with Molecular Medium and Track Effects in Radiation Chemistry, *Adv. Chem. Phys.*, 68:255-386.

79. Heller, J.M. et al. 1974. Collective Oscillation in Liquid Water, *J. Chem. Phys.*, 60:3483-3486.

80. Laverne, J.A.; and Mozumder, A. 1993. Concerning Plasmon Excitation in Liquid Water, *Radiat. Trs.*, 133, p.282.

81. Schwinger, J. 1949. On Radiation Correction to Electron Scattering, *Phys. Rev.*, 75, p.898.

82. Evan, R.D. 1955. The Atomic Nucleus, pp. 592-593, McGraw-Hill Company, Inc., New York, NY.

83. Molièr, G. 1949. Theorie der Streuung Schneller Gelandener Teilchen II: Mehrfach- und Vielfachstreuung, *Z. Naturforsch,* a3:78-97.

84. Evans, R.D. 1955. The Atomic Nucleus, p. 599, McGraw-Hill Company, Inc., New York, NY.

85. Porter, H.S.; and Jump, F.W. 1978. Analytic Total and Angular Elastic Electron Impact Cross sections for Planetary Atmospheres, Report No. CSC/TM-78/6017, Computer Science Corp.

86. Seng, G. 1975. e-H_2O Differentielle Streuexperimente bei Kleinsten Energien, Thesis, Kaiserslautern University, Germany.

87. Shyn, T.W.; and Cho, S.Y. 1987. Vibrationally Elastic Cross Section of Water Vapor by Electron Impact, *Phys. Rev.*, A36,11:5138-5142.

88. Hyashi, M. 1989. Electron Collision Cross Sections for Atoms and Molecules Determined from Beam and Swarm Data. In Atomic and Molecular Data for Radiotherapy, IAEA-TECDOC-506, p.193, International Atomic Energy Agency, Vienna, Austria.

89. Johnstone, W.M.; and Newell, W.R. 1991. Absolute Vibrationally Elastic Cross Sections for Electron Scattered from Water Molecules Between 6 eV and 50 MeV, *J. Phys. B:At. Mol. Opt. Phys,* 24:3633-3643.

90. Katase, A. et al. 1986. Elastic Scattering of Electron by Water Molecules Over the Range 100-1000 eV, *J. Phys. B:At. Mol. Opt. Phys,* 19:2715-2734.

91. Shyn, T.W.; and Grafe, A. 1992. Angular Distribution of Electrons Elastically Scattered from Water Vapor, *Phys. Rev.,* A46,7:4406-4409.

92. Hwang, W.; and Kim,Y-K. 1996. New Model for Electron-impact Ionization Cross Sections of Molecules, *J. Chem. Phys.,* 104,22:2956-2966.

93. Williams, E.J. 1935. Correlation of Certain Collision Problems with Radiation Theory, *Kgl. Danske Videnskab. Mat.-fys. Medd.,* XIII, 4.

94. Kim, Y-K. 1994. Binary-encounter-dipole Model for Electron-impact Ionization, *Phys. Rev.,* A50,5:3954-3967.

95. Vriens, L. 1969. In Case Studies in Atomic Physics, McDaniel, E.W.; and McDowell, M.R.C. eds., Vol. I, p. 335, North-Holland Publ., Amsterdam.

96. Bethe, H. 1930. Zur Theorie des Durchgangs Schneller Korpuskularstrahlen durch Materie, *Ann. Physik.,* 5:325-400.

97. Rudd, M.E. 1992. Electron Production in Proton Collision with Atoms and Molecules: Energy Distribution, *Rev. Of Mod. Phys.,* 64,2:441-490.

98. Kim,Y-K., personal communication, December 20, 1996.

99. Seltzer, S.M. 1988. Cross Sections for Bremsstrahlung Production and Electron-Impact Ionization, Methods for Coupled Electron/Photon Transport Calculations, International School of Radiation Damage and Protection, 8th Course: Monte Carlo Transport of Electrons and Photons below 50 MeV, Ettore Majarana Center for Scientific Culture, Erice, Italy.

100. Mann, J.B. 1968. Atomic Structure Calculations. II. Hatree-Fock Wave Functions and Radial Expression Values: Hydrogen to Lawrencium, Report No. LA-3691, Los Alamos National Lab., NM.

101. Seigbahn, K. et al. 1969. ESCA Applied to Free Molecules, North-Holland Publ. Company, Amsterdam.

102. Bethe, H. 1932. Bremsformel für Elektronen Relativistischer Geschwindigkeit, Z. *Phys.*, 76:293-299.

103. Schutten, J. et al. 1965. Gross- and Partial-Ionization Cross Sections for Electrons on Water Vapor in the Energy Range 0.1-20 keV, *J. Chem. Phys.*, 44,10:3924-3928.

104. Djurić, N.Lj; Čadež, I.M.; and Kurepa, M.V. 1988. H_2O and D_2O Total Ionization Cross-Sections by Electron Impact, *Int. J. Mass spec. And Ion Proc.*, 83:R7-R9.

105. Bolorizadeh, M.A.; and Rudd, M.E. 1986. Angular and Energy Dependence of Cross Sections for Ejection of Electrons from Water Vapor. I. 50-2000 eV Electron Impact, *Phys. Rev.*, A33,2:882-887.

106. Dayashankar; and Green, A.E. 1992. Analytic Electron Impact Inelastic Cross Sections for Water Vapor and A Study of Energy Deposition, *Radiat, Phys, Chem,* 40,6:523-528.

107. Green, A.E.S.; Olivero, J.J.; and Stagat, R.W. 1971. Microdosimetry of Low-Energy Electrons, Proc. Of a Symp. on Biophysical Aspects of Radiation Quality: Aspects of Radiation Quality, La CasHeight, Austria, Report No. IAEA-SM-145/8, International Atomic Energy Agency, Vienna, Austria.

108. Olivero, J.J.; Stagat, R.W.; and Green, A.E.S. 1972. Electron Deposition in Water Vapor, with Atmospheric Applications, *J. Geo. Res.*, 77,25:4797-4811.

109. Mann, M.M.; Hustrulid, A; and Tate, J.T. 1940. The Ionization and Dissociation of Water Vapor and Ammonia by Electron Impact, *Phys. Rev.*, 58,340.

110. Muschlitz, E. E.; and Bailey, T.L. 1956. Negative Ion Formation in Hydrogen Peroxide and Water Vapor, The Peroxide Ion, . *Phys. Chem.*, 60,681.

111. Buchel'nikova, N. S. 1959. Cross Sections for Capture of Slow Electron by O_2 and H_2O Molecules and Molecules of Halogen Compounds, *Sov. Phys. JETP,* 35, 783.

112. Compton, R. N.; and Christophorou, L.G. 1967. Negative-Ion Formation in H_2O and D_2O, *Phys. Rev.*, 154, 110.

113. Green, A; and Mann, A. 1987. The Big Bands of H_2O, *Radiat. Res.*, 112:11-20.

114. Seng, G; and Liner, F. 1976. Vibrational Excitation of Polar Molecules by Electron Impact II. Direct and Resonant Excitation in H_2O, *J. Phys. B:Atom. Molec. Phys.*, 9, 14:2539-2551.

115. Shyn, T.W.; Cho, S.Y.; and Cravens, T.E. 1988. Vibrational-Excitation Cross Sections of Water Molecules by Electron Impact, *Phys. Rev.*, A38, 2:678-682.

116. Paretzke, H.G.; and Berger, M.J. 1978. Stopping Power and Energy Degradation for Electrons in Water Vapor. In: Proce. Of the 6th Symp. on Microdosimetry, Booz, J; and Ebert, H.G. eds., pp. 749-758, Harwood, Brussels.

117. Lappa, A.V. et al. 1993. "TRION" Code for Radiation Action Calculations and Its Application in Microdosimetry and Radiobiology, *Radiat. Environ. Biophys.*, 32:1-19.

118. International Commission on Radiation Units and Measurements. 1970. Linear Energy Transfer, ICRU Report No. 16, Bethesda, MD.

119. Paretzke, H.G. et al. 1986. Calculated Yields and Fluctuations for Electron Degradation in Liquid Water and Water Vapor, *J. Chem. Phys.*, 84, 6:3182-3188.

120. Carter, L.L; and Cashwell, E.D. 1975. Particle-Transport Simulation with the Monte Carlo Method, TID-26607, National Technical Information Center, Springfield, VA.

121. Grosswendt, B; and Waibel, E. 1978. Transport of Low Energy Electrons in Nitrogen and Air, *Nucl. Instr. Meth.* 155:145-156.

122. Trajmar, S.; William, W.; and Kuppermann, A. 1972. Electron Impact Excitation of H_2O, *J. Chem. Phys.*, 58, 6:2521-2531.

123. Evans, R.D. 1955. The Atomic Nucleus, pp. 536-566, McGraw-Hill Company, Inc., New York, NY

124. Wu, C.S.; and Moskowski, S.A. 1966. Beta Decays, Interscience, New York, NY.

125. Dillman, L.T. 1969. Radionuclide Decay Schemes and Nuclear Parameters for Use in Radiation Dose Estimation, MIRD Pamphlet No. 4, *J. Nucl. Med.*, 10, Supl. 2.

126. Kuki, H. 1972. Complex Gamma Function with Error Control, *Numer. Math.*, 15, 4:262-267.

127. International Commission on Radiation Units and Measurements. 1983. Microdosimetry, ICRU Report No. 36, Bethesda, MD.